nagra
National Cooperative for the
Disposal of Radioactive Waste

TECHNICAL REPORT 04-05

Modelling of Tracer Profiles in Pore Water of Argillaceous Rocks in the Benken Borehole:

Stable Water Isotopes, Chloride, and Chlorine Isotopes

December 2004

T. Gimmi and H.N.Waber

Hardstrasse 73, CH-5430 Wettingen/Switzerland, Telephone +41-56-437 11 11

nagra
National Cooperative for the
Disposal of Radioactive Waste

TECHNICAL REPORT 04-05

Modelling of Tracer Profiles in Pore Water of Argillaceous Rocks in the Benken Borehole:

Stable Water Isotopes, Chloride, and Chlorine Isotopes

December 2004

T. Gimmi [1,2] and H.N.Waber [1]

[1] RWI, Institute of Geological Sciences, University of Bern, Switzerland

[2] Paul Scherrer Institut, Villigen PSI, Switzerland

Hardstrasse 73, CH-5430 Wettingen/Switzerland, Telephone +41-56-437 11 11

This report was prepared on behalf of Nagra. The viewpoints presented and conclusions reached are those of the author(s) and do not necessarily represent those of Nagra.

ISSN 1015-2636

"Copyright © 2004 by Nagra, Wettingen (Switzerland) / All rights reserved.
All parts of this work are protected by copyright. Any utilisation outwith the remit of the copyright law is unlawful and liable to prosecution. This applies in particular to translations, storage and processing in electronic systems and programs, microfilms, reproductions, etc."

Abstract

Isotope tracers offer unique possibilities for analysing flow and transport processes over large scales of time and space. This is especially relevant for low-permeability media like claystones, where transport is typically very slow and, consequently, difficult to investigate. Such lithologies are currently being investigated in several countries as potential host rocks for the disposal of radioactive or other hazardous waste. In the deep borehole at Benken (north-eastern Switzerland), a sequence of aquifers and argillaceous aquitards was investigated. Water samples were obtained from four formations (Malm, Keuper, Muschelkalk, and Buntsandstein). The Malm and the Keuper aquifer delimit a sequence of claystones and marls at depth from about 400 to 700 m with hydraulic conductivities generally below 10^{-13} m s^{-1}. Profiles of $\delta^{18}O$, $\delta^{2}H$, chloride, and $\delta^{37}Cl$ in pore fluids of these formations were obtained. The chemical, isotopic, and noble gas composition of the ground water samples indicated that no cross-formation flow occurred, but that – with the exception of the Malm – the waters evolved geochemically within the formation from which they were sampled. Infiltration conditions could also be inferred from the data. The pore water profiles in the low-permeability zone show clear trends that hint at diffusion-dominated transport processes. To evaluate possible mechanisms and time scales of evolution of the profiles, a series of advective-dispersive model calculations was performed. Varying initial conditions as well as the type and concentration values of boundary conditions revealed the following: (i), molecular diffusion to the underlying aquifer can explain the general features of the isotope profiles, (ii), no signatures of advective flow could be detected, (iii), the evolution time is in the order of 0.5 to 1 Ma (relying on laboratory diffusion coefficients) with a possible range of about 0.2 to 2 Ma, which is geologically plausible, and, (iv), parameters measured on small scales (centimeters or meters, months) are also plausible at the formation scale (tens of meters, millions of years) for the sediments investigated .

Zusammenfassung

Natürlich vorkommende Isotope im Grundwasser bieten einzigartige Möglichkeiten zur Untersuchung von Wasserfluss und Transportprozessen über grosse Zeiträume und Distanzen. Dies gilt insbesondere für geologische Medien mit geringen Durchlässigkeiten, wie z.B. Tonsteine und Mergel, wo der Transport von gelösten Stoffen typischerweise sehr langsam und deshalb schwierig zu untersuchen ist. Zur Zeit werden solch gering durchlässige Lithologien in mehreren Ländern an potenziellen Standorten für die Tiefenlagerung von radioaktiven oder anderweitig toxischen Abfällen untersucht. In der Sondierbohrung Benken (Nordostschweiz) konnte eine Abfolge von Aquiferen mit zwischengelagerten gering durchlässigen tonigen Gesteinen (Aquitarden) untersucht werden. Grundwasser konnte in verschiedenen Tiefen aus Einheiten des Malms, Keupers, Muschelkalks und Buntsandsteins entnommen werden. Die Aquifere im Malm und Keuper umgeben eine Ton-Mergel-Abfolge in einer Tiefe von ca. 400 m bis 700 m, welche auch den Opalinuston beinhaltet und welche eine durchschnittliche hydraulische Leitfähigkeit von weniger als 10^{-13} m s^{-1} aufweist. Im Porenwasser dieser Ton-Mergel-Abfolge wurden die stabilen Isotope von Wasser ($\delta^{18}O$, $\delta^{2}H$), der Chloridgehalt und die Chlorisotope ($\delta^{37}Cl$) als Funktion der Tiefe bestimmt. Die chemische und isotopische Zusammensetzung und die Edelgasgehalte der Grundwässer schliessen eine Kommunikation zwischen den verschiedenen Aquiferen aus. Die Grundwässer entwickelten sich zudem in den Gesteinen, aus welchen sie entnommen wurden. Einzig beim Malmwasser bestehen Hinweise auf einen Zufluss aus dem südlichen Molassebecken. Die Daten erlauben weiter eine Herleitung der Infiltrationsbedingungen der Grundwässer bezüglich Klima und Ort. Die Konzentrationsverläufe im Porenwasser der gering durchlässigen Gesteine zeigen deutliche Trends, welche auf diffusionsdominierte Transportprozesse hinweisen. In einer Reihe von advektiv-diffusiven Modellrechnungen wurden mögliche Prozesse und Zeitskalen, welche für den Aufbau der Konzentrationsverläufe in Frage kommen, untersucht. Dabei wurden sowohl die Anfangsbedingungen im Zentrum der gering durchlässigen Zone, als auch die Randbedingungen in den umgebenden Aquiferen variiert. Die Modellrechnungen lassen die folgenden Schlüsse zu: (i) Stofftransport via molekulare Diffusion in Richtung des unterliegenden Aquifers kann die beobachteten Konzentrationsverläufe generell erklären, (ii) es konnte kein Hinweis auf eine advektive Transportkomponente gefunden werden, (iii) die Aufbauzeit der beobachteten Konzentrationsverläufe beträgt etwa 0.5 bis 1 Ma (wenn mit Labor-Diffusionskoeffizienten berechnet) mit einem möglichen Bereich zwischen 0.2 bis 2 Ma, welcher geologisch plausibel ist, und (iv) Transportparameter, welche für die untersuchten Gesteine in kleinem Massstab (cm, m und Tage, Monate) bestimmt wurden, sind auch für den Feldmassstab (Dekameter, Millionen von Jahre) plausibel.

Résumé

Les isotopes présents naturellement dans les eaux souterraines sont particulièrement bien adaptés à l'étude des écoulements souterrains et des phénomènes de transport, lorsque ceux-ci se déroulent sur de longues périodes et des distances importantes. C'est le cas dans les roches à faible perméabilité, comme par exemple les argiles et les marnes, où le déplacement des solutés est généralement très lent et par conséquent difficile à observer. Dans différents pays, ce type d'environnement géologique peu perméable fait actuellement l'objet d'études dans la perspective d'un stockage en profondeur de déchets radioactifs ou toxiques. Le sondage profond de Benken (nord-est de la Suisse) a permis l'observation d'une série de couches aquifères séparées par des couches argileuses peu perméables (aquitards). Des échantillons d'eaux souterraines ont été prélevés à différentes profondeurs dans des couches du Malm, Keuper, Muschelkalk et Buntsandstein. Les couches aquifères du Malm et du Keuper entourent une séquence d'argiles et de marnes à une profondeur d'environ 400 à 700 m, qui renferme également la couche d'argiles à Opalinus et dont la conductivité hydraulique moyenne est inférieure à 10^{-13} m s^{-1}. Dans l'eau interstitielle de cette séquence argilo-marneuse, on a déterminé les isotopes stables de l'eau ($\delta^{18}O$, $\delta^{2}H$), les concentrations en chlorure et les isotopes de chlore ($\delta^{37}Cl$) en fonction de la profondeur. La composition chimique et isotopique des eaux souterraines, ainsi que les gaz nobles qu'elles contiennent, permettent d'exclure une communication entre les différentes couches aquifères. De plus, les eaux souterraines portent l'empreinte géochimique de l'environnement minéralogique duquel elles sont issues. Seules les eaux du Malm indiquent un apport en provenance du bassin molassique plus au sud. Les données ont en outre permis de déduire le lieu ainsi que les conditions climatiques d'infiltration des ces eaux. Les profils de concentration dans les eaux interstitielles des roches faiblement perméables présentent certaines tendances qui indiquent nettement un transport dominé par les phénomènes diffusifs. Une série de modélisations advectives/diffusives a permis d'étudier les phénomènes et échelles de temps qui ont pu produire ce type de profil. Des variations de paramètres ont été effectuées tant sur les conditions initiales dans la zone peu perméable que sur les conditions à la limite régnant dans les couches aquifères environnantes. Les modélisations ont fourni les résultats suivants: (i) Un transport de solutés par diffusion moléculaire en direction de l'aquifère inférieur permet, d'une façon générale, d'expliquer les profils de concentration observés, (ii) aucun indice ne permet de conclure à un transport par advection, (iii) la durée d'élaboration des profils de concentration observés s'élève à environ 0,5 bis 1 Ma (lorsqu'elle est calculée avec des coefficients de diffusion de laboratoire), les pôles extrêmes se situant à 0,2 et 2 Ma, ce qui est plausible du point de vue géologique, et (iv) les paramètres de transport déterminés pour les roches étudiées à petite échelle (cm, m et jours, mois) sont également plausibles à l'échelle du terrain (décamètres, millions d'années) pour les roches envisagées.

Table of Contents

List of Tables

List of Figures

1 Introduction

Claystones and marls have typically very low permeability. Consequently, they are widely considered as potential host rocks for the disposal of radioactive or other hazardous wastes. The barrier function of host rocks helps to retain wastes within the original disposal site and to minimise the risk of contamination of the biosphere.

Transport properties of potential host rock formations are usually assessed by determining diffusion coefficients and permeabilities on small samples at laboratory scale, or by hydraulic tests in boreholes. Material properties so obtained are then scaled up with the help of mathematical models, taking into account structures relevant at larger scales. Field experiments may be run at larger scales to verify partly upscaled transport properties. Performing experiments at scales of hundreds of meters and thousands to millions of years, which are relevant in case of disposal of radioactive waste is, however, impossible.

In this situation, the analysis of natural isotope tracers offers unique possibilities. Their concentration patterns in pore fluids have developed over geologic time spans. Looking back to what has happened in the past allows model concepts and material properties at relevant scales to be evaluated (e.g., Eggenkamp et al. 1994; Hendry et al. 2000; Patriarche et al. 2004a and b). A perturbation of the chemical or hydraulic situation in an aquifer delimiting an aquitard can propagate through the low-permeability rock. The characteristic time for the propagation and dissipation of the disturbance – and thus the time span over which a signature in the environmental tracers can be observed – depends on the initial situation, the type of disturbance, and the physical and chemical properties of the rock.

There is, unavoidably, a drawback to the approach of using natural tracers in that the set-ups of the "Experiments Performed by Nature" are not exactly known. The present-day chemical and isotopic composition of a ground water can be accurately determined even when sampled from great depth. In order to estimate which perturbations occurred in the past, the conditions observed today have to be extrapolated backwards. This can be done with relatively good confidence by combining information about the regional palaeo-hydrological and hydrochemical evolution.

In contrast, present-day as well as past pore-water concentrations in an aquitard are more difficult to characterise. This is due to the fact that (1) the pore-water composition cannot be measured directly, but has to be derived by indirect, complementary methods that are susceptible to various types of errors (Sacchi & Michelot 2000; Pearson et al. 2003) and (2) concentrations in the aquitard react slowly to perturbations and may thus represent superpositions of several earlier events. This implies that the initial conditions at the starting point of solute transport under presently prevailing boundary conditions can only be defined as a compositional range even when the regional palaeo-hydrogeological evolution is well understood.

In argillaceous rock sequences of low permeability additional complications arise from the fact that different solutes may access different parts of the pore space due to electrostatic or steric interactions with the clay surfaces (Horseman et al. 1996; Pearson 1999; Nagra 2002, Chapter 5.4; Pearson et al. 2003). Accurate modelling of observed data therefore requires solute-specific transport porosities and diffusion coefficients. All this highlights the necessity for a description of the aquifer ground water, i.e. boundary conditions, as precise as possible to reduce the overall uncertainty of transport calculations in an aquifer–aquitard system. Adequate predictions of the

geosphere system behaviour can only be made when based on a comprehensive understanding of these various aspects.

Ratios of stable water isotopes ($^{18}O/^{16}O$ and $^{2}H/^{1}H$), of chlorine isotopes ($^{37}Cl/^{35}Cl$), and chloride concentrations of pore water have been determined on core material from a deep borehole in north-eastern Switzerland (Rübel & Sonntag 2000; Nagra 2001 and 2002; Waber et al. 2003). The borehole was drilled across Jurassic and uppermost Triassic low-permeability formations, including the Opalinus Clay as the formation of interest. The low-permeability formations are sandwiched between two aquifers in the Malm and Keuper lithologies, respectively. Mass exchange processes with the aquifers have led to characteristic isotope signatures across the low-permeability zone. We analysed these signatures with advective-diffusive transport models, testing various boundary and initial conditions. The modelling results allowed assessment of large-scale transport behaviour and comparison of laboratory scale parameters obtained for the Opalinus Clay with large-scale parameters.

In the following, we will give an overview of the hydrogeology in the test area (Chapter 2) and describe the ground waters in the aquifers (Chapter 3), which represent the boundaries of the low-permeability zones. Chapter 3 is essentially a summary of a Nagra Internal Report (Waber et al. 2002) compiled by W. Aeschbach-Hertig (noble gases), L. Eichinger (dissolved gases, isotopes), B.E. Lehmann and H.H. Loosli (noble gas isotopes), and F.J. Pearson and H.N. Waber (hydrochemistry, geochemical modelling). Chapter 4 presents the measured pore-water data ($\delta^{18}O$, $\delta^{2}H$, $\delta^{37}Cl$ and Cl concentrations) in the low-permeability zone. In Chapter 5 we outline the assumed geological scenario and the modelling approaches, and define boundary and initial conditions for solute transport in the low-permeability rock sequence. Chapter 6 presents the results, from which project-relevant conclusions can be drawn (Chapter 7).

Unfortunately, no general convention exists with respect to the terms describing the water in the underground. In this report, we follow the terminology of earlier reports and use “ground water” to denote freely flowing water in an aquifer. Water from low-permeability zones is denoted as “pore water”. Typically, such pore water from low-permeability zones cannot be sampled by conventional ground water sampling techniques.

2 Hydrogeological setting

2.1 Geology

The deep borehole was drilled at Benken (co-ordinates: 690'988.80/277'842.90, 404.30 m above sea level) in the Zürcher Weinland, a region in north-eastern Switzerland. The study area of the Zürcher Weinland is located in a tectonically quiet region between the northern boundary of the Swiss Molasse Basin and the Tabular Jura in north-eastern Switzerland (Figure 1).

A 3D seismic survey (Birkhäuser et al. 2001) has revealed that the sedimentary rocks in the area are nearly horizontally bedded. The sedimentary sequence comprises Jurassic and Triassic sediments that are exposed in the Tabular Jura and the foothills of the Black Forest Massive to the north-east and dip beneath the Tertiary Molasse sediments at an angle of about 3 – 5° towards the southeast. With a detection limit for vertical displacements of 4 m to 10 m (qualitative) and larger than 10 m (quantitative), the seismic survey further revealed that there are no large faults present in the area. Based on these results, the sequence of stratigraphic layers encountered in the Benken borehole is representative for the whole area.

The lithostratigraphy encountered in the Benken borehole is summarised in Figure 2. The Quaternary consists of a vertical and horizontal alteration of clay, silt, sand, gravel, and lacustrine clay (Nagra 2000). The Tertiary underlying the Quaternary is composed of a 124 m thick layer of Lower Freshwater Molasse consisting of coloured marls and poorly cemented sandstones. The lowest 7 m are made of mostly ochre-coloured clays with inclusions of bean ore (Eocene Bean-Ore Formation).

Below the Tertiary, Malm, Dogger and Lias sediments of Jurassic age are encountered indicating that the whole Cretaceous sequence was eroded. At the top of these Jurassic sediments the Upper Malm comprises a 252 m thick sequence of limestone with thin marl intercalations. The period of erosion during early Tertiary times resulted in a karstification of these limestone units. The Dogger sediments below consist of about 200 m of marine claystone and marls with intercalated thin layers of limestones, calcareous sandstones and iron ooliths. These sediments also contain the Opalinus Clay Formation which is 113.2 m thick (including the Murchisonae Beds with Opalinus Clay facies), and comprises a sequence of dark grey, silty and calcareous claystones. This unit is being investigated as a potential host rock. Below, the Liassic comprises about 40 m of marine marls, silt- and claystones, and thin limestone beds.

The Triassic sediments comprise mainly continental alluvial and evaporite sequences of Keuper, Muschelkalk and Buntsandstein age. The upper third of the 199 m thick Keuper consists of sandy lithologies and dolomite-breccias of the Stubensandstein and Schilfsandstein Formations, while the lower two thirds consist of partly argillaceous anhydrite and gypsum layers and dolomites of the Gipskeuper. Below are various dolomites and micritic limestone of the Upper Muschelkalk (63 m), laminated dolomites, marls, claystones, and thick anhydrite banks with rock salt of the Middle Muschelkalk (64 m), and the 34 m thick sequence of dark grey to black claystones with thin sandstone and dolomite layers of the Lower Muschelkalk. Overlying the crystalline basement, at the bottom of the sediment pile are about 8 m of continental, coloured sandstones, the Buntsandstein.

The Mesozoic sediment pile in north-eastern Switzerland underwent a diagenetic over-print during two burial phases (Leu et al. 2001; Nagra 2002, Chapter 3.3). A first, long-term burial occurred during Cretaceous times to a depth of about 1 100 m, before about 600 m of sediment were eroded again during early Tertiary times (Palaeocene to Eocene, 65 to 33.7 Ma b.p.). In the late Tertiary, the sediment pile was buried a second time to about 1 700 m of depth. This burial

was shorter and reached its maximum about 10 Ma before present. Maximum temperatures of the two overprints were low, but higher during Cretaceous times (81 ºC to 93 ºC) due to the longer burial. These events led to maturation of the organic material present in the rocks, carbonate cementation in the silty layers, limited re-crystallisation of clay minerals, and the formation and mineralisation of veins.

In the Benken drill core only few open structures were observed in limestones, dolomites and sandstones, while veins are generally closed in the claystones, marls, and the gypsum-anhydrite layers (Mazurek 2001; Nagra 2002, Chapter 5.3). Calcite is the most abundant fracture mineral and occurs in all lithologies. In the argillaceous sequences well-preserved pyrite, quartz, barite, celestite, and newly formed clay minerals occur infrequently. In the Triassic continental and evaporite sediments fracture minerals include well-preserved pyrite, quartz, barite, gypsum and anhydrite in addition to calcite.

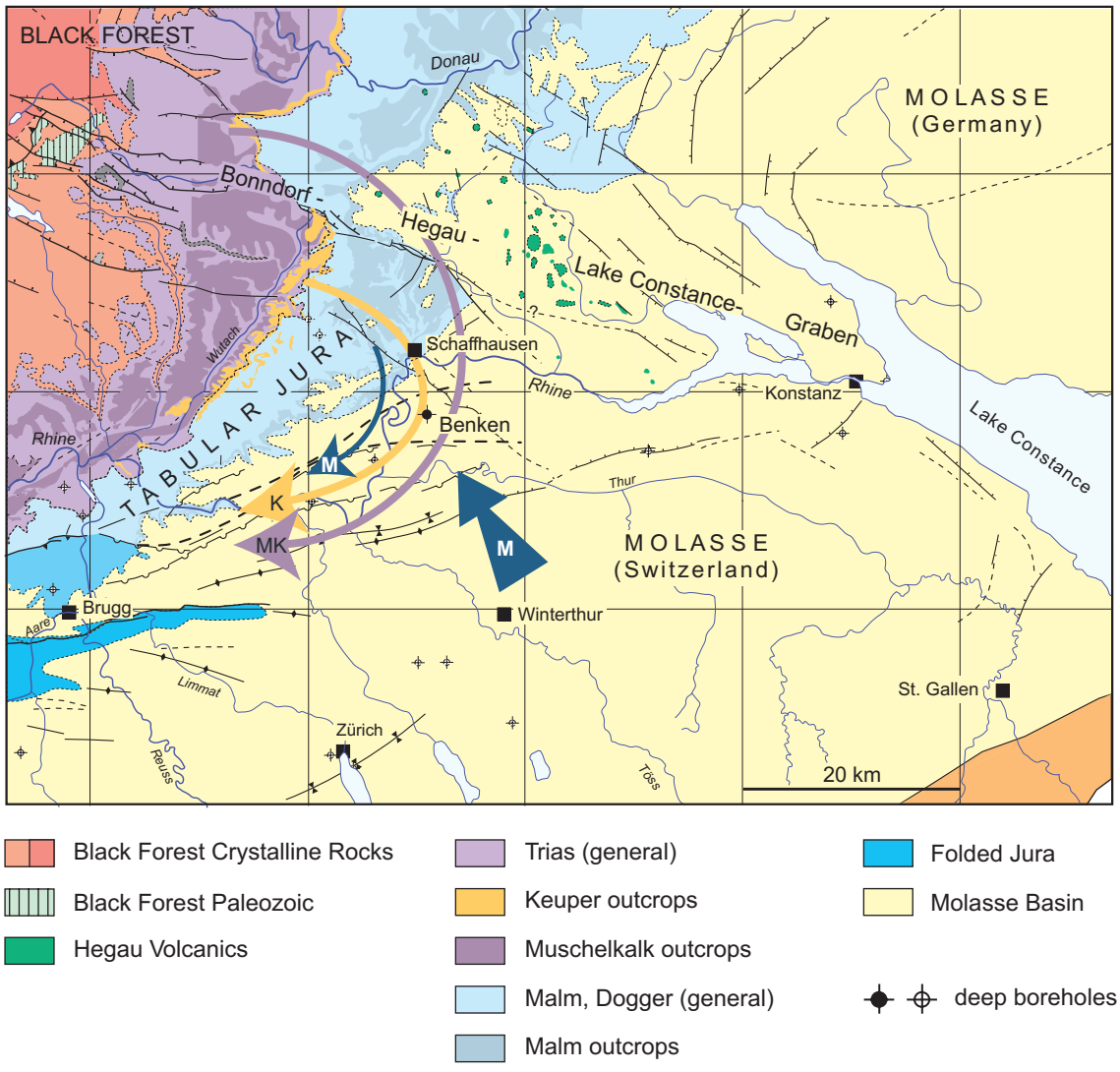

Figure 1: Simplified tectonic map of north-eastern Switzerland and south-western Germany showing the location of the Benken borehole, areas of direct infiltration into the aquifer lithologies (outcrops) and suggested ground water flow paths.

See text for explanations regarding ground water flow paths, indicated by arrows.

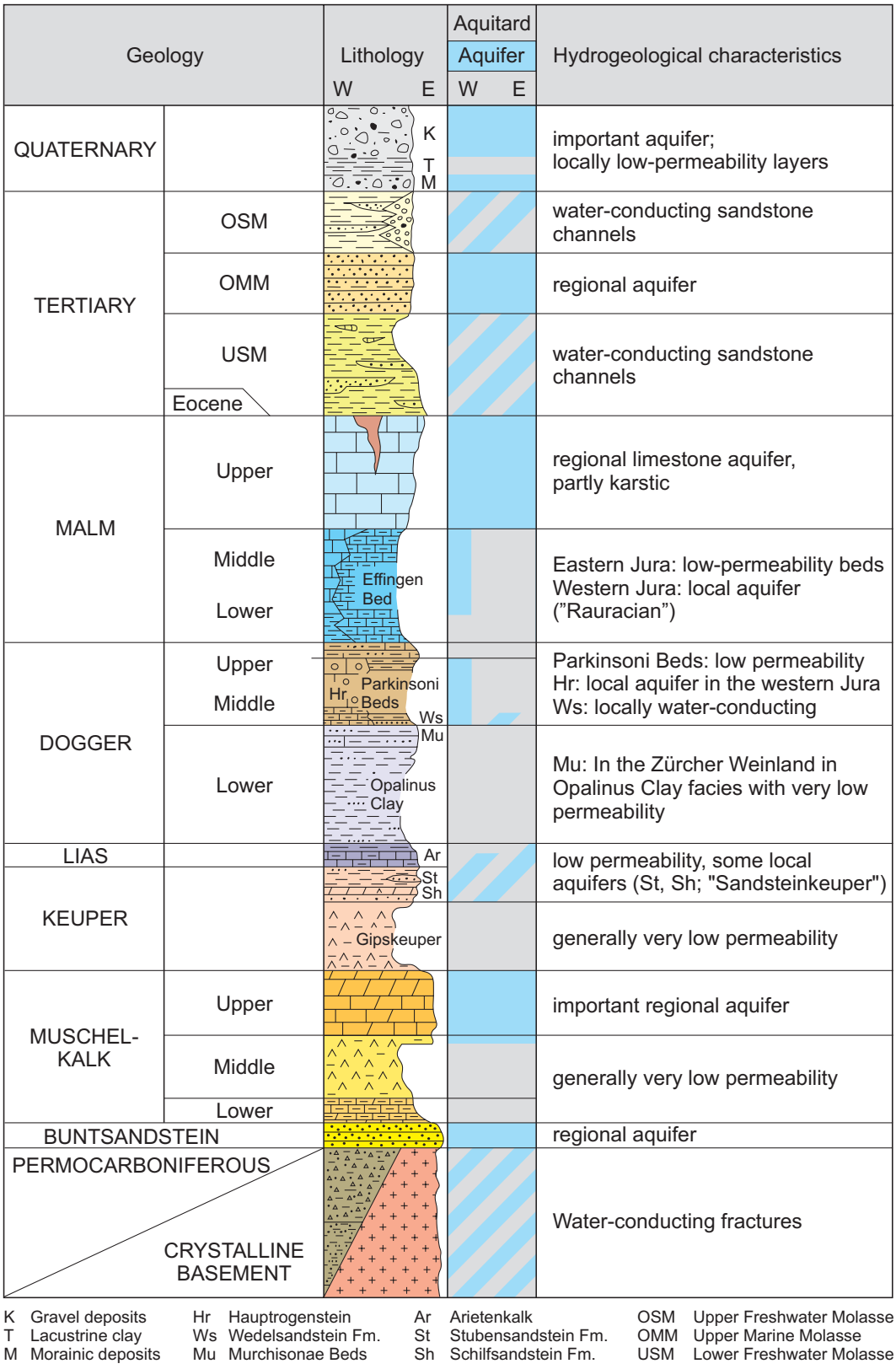

Figure 2: Stratigraphy as encountered in the Benken borehole and schematic hydrostratigraphic division in northern Switzerland and adjacent areas west of the river Aare.

Modified from Nagra 2002.

2.2 Hydrogeology

Certain lithologies of the Malm, Muschelkalk, and Buntsandstein are known to constitute regional aquifers with commonly high ground water production rates in northern Switzerland and adjacent southern Germany (Bertleff 1986; Schmassmann 1990; Schmassmann et al. 1992; Stober & Villinger 1997). The alluvial Keuper lithologies, in contrast, form aquifers of only local extent due to their high lateral variability (Biehler et al. 1993). The argillaceous rocks of the Dogger and Lias, the evaporites of the Lower Keuper, and the evaporites and argillaceous rock sequences of the Middle and Lower Muschelkalk commonly act as confining layers between these aquifers (Figure 2).

Karstification of the Malm limestones during early Tertiary times (about 65 to 33.7 Ma b.p.) resulted in a complex flow regime characteristic for such environments (Bertleff 1986; Lemcke 1987; Villinger 1988). The present hydraulic conductivity of Malm limestones is highly variable with values between 10^{-11} m s^{-1} and 10^{-4} m s^{-1} (Stober & Villinger 1997; Nagra 2002, Chapter 3.6). Values of hydraulic conductivities measured in the Benken borehole are shown in Figure 3. Major infiltration areas for the Malm aquifer are in the north along the Black Forest crystalline basement from the river Rhine to the river Donau (Danube) and in the Folded Jura mountains to the west. Indirect infiltration through the Molasse sediments takes place in the south (Figure 1). Discharge from the Malm aquifer occurs into the river Danube to the east and into the river Rhine to the north and west of the study area with the water-divide being east of the Lake of Constance (Bertleff & Watzel 2002; Nagra 2002, Chapter 3.6). It should be noted that the present flow direction of the Rhine river was established around the Pliocene – Pleistocene boundary (2.7 Ma b.p.) when the river changed its flow direction from north-east towards the river Donau to the west towards the city of Basel (cf. Figure 1; Hofmann 1996; Villinger 2003). First discharge from the Malm limestones into the Rhine river is thought to have occurred in the early Pleistocene (about 1.8 - 2 Ma b.p.) when the river eroded into these limestones.

The evolution of Malm ground water has to be interpreted within this complex palaeohydrologic history from Jurassic to present times. The Malm limestones are of marine origin and the original formation water was seawater. Erosion of the overlying Cretaceous marine sediments and subsequent karstification of the Malm limestones resulted in the first dilution of the marine-type formation water with fresh water during the early Tertiary times. The succeeding deposition of up to 6 000 m of Tertiary Molasse sediments in four alternating fresh-water and marine- to brackish-water cycles gave rise to a complex mixture of fresh- and marine-water components. Sedimentation of these mainly detrital formations occurred under warm semi-arid to semi-humid climatic conditions from middle Oligocene (Lower Marine Molasse) to the late Miocene (Upper Freshwater Molasse, Trümpy 1980), that is about 30 to 10 Ma ago. It is generally agreed that the Molasse and Malm aquifers in northern Switzerland and southern Germany represent a coupled hydrologic system (Bertleff 1986; Balderer 1990; Schmassmann 1990; Stober & Villinger 1997; Bertleff & Watzel 2002).

In the Keuper aquifer the hydraulic continuity within an individual stratigraphic unit is limited due to pronounced lateral differences in lithology. This is confirmed by the strong lateral variability of the hydraulic conductivity of an individual unit (10^{-10} to 10^{-7} m s^{-1}; Nagra 2002, Chapter 3.6) and by the fact, that the water-conducting zone is different in different boreholes in the region (Biehler et al. 1993). On a regional scale, ground water flow in the Keuper occurs due to a hydraulic connection of these individual units, which are all bound by the overlying Liassic claystones and marls and underlying evaporate layers of the Keuper. A conceptual flow model suggests the foothills of the Black Forest east of the river Wutach as the major infiltration area. Discharge of ground water from the Keuper water-conducting zones occurs westwards in the river Rhine (Nagra 2002, Chapter 3.6). In the study area, the water-conducting zone of the

Keuper is the Stubensandstein Formation, which consists of sandy layers at the bottom and dolomite breccias at the top with a hydraulic conductivity of about 10^{-7} m s^{-1} (Nagra 2002, Chapter 3.6). The porous dolomite-breccias are the result of the dissolution of evaporitic layers during diagenesis. The exfiltration zones for the Keuper aquifer that are still active today were probably created by deep erosion in the Klettgau area some 1.8 Ma ago following the diversion of the Alpenrhein towards the Aare river, which occurred about 2.7 Ma b.p. (Villinger 2003). The change in flow direction also coincides about with the exhumation of the Keuper lithologies and direct infiltration into these.

In the Muschelkalk aquifer the productive zone of regional extent is the Trigonodus-Dolomit Formation. In northern Switzerland and southern Germany its hydraulic conductivity varies between about 10^{-5} m s^{-1} and 10^{-9} m s^{-1} depending on the fracture intensity and solution porosity (Nagra 1988; Stober & Villinger 1997). Direct infiltration into the Muschelkalk occurs in the foothills of the Black Forest west of the river Wutach (Figure 1). In the study area, discharge is expected to occur towards the west into the river Rhine, while in Germany discharge also occurs towards the north into the river Neckar (Nagra 2002, Chapter 3.6; Stober & Villinger 1997).

Where the Buntsandstein directly overlies the weathered uppermost part of the crystalline basement, the two units form a regional aquifer. The hydraulic conductivity in the Buntsandstein varies between about 10^{-7} m s^{-1} and 6×10^{-6} m s^{-1} (Nagra 2002, Chapter 3.6). Infiltration occurs in the foothills and the crystalline of the Black Forest west of the river Wutach and extending beneath the sedimentary cover into northern Switzerland; the discharge areas are along the river Rhine (Thury et al. 1994).

Figure 3 shows also the hydraulic pressures measured in aquifers and aquitards of the Benken borehole. It should be noted that measuring pressures in the low permeability media is rather difficult and thus leads to relatively large uncertainties.

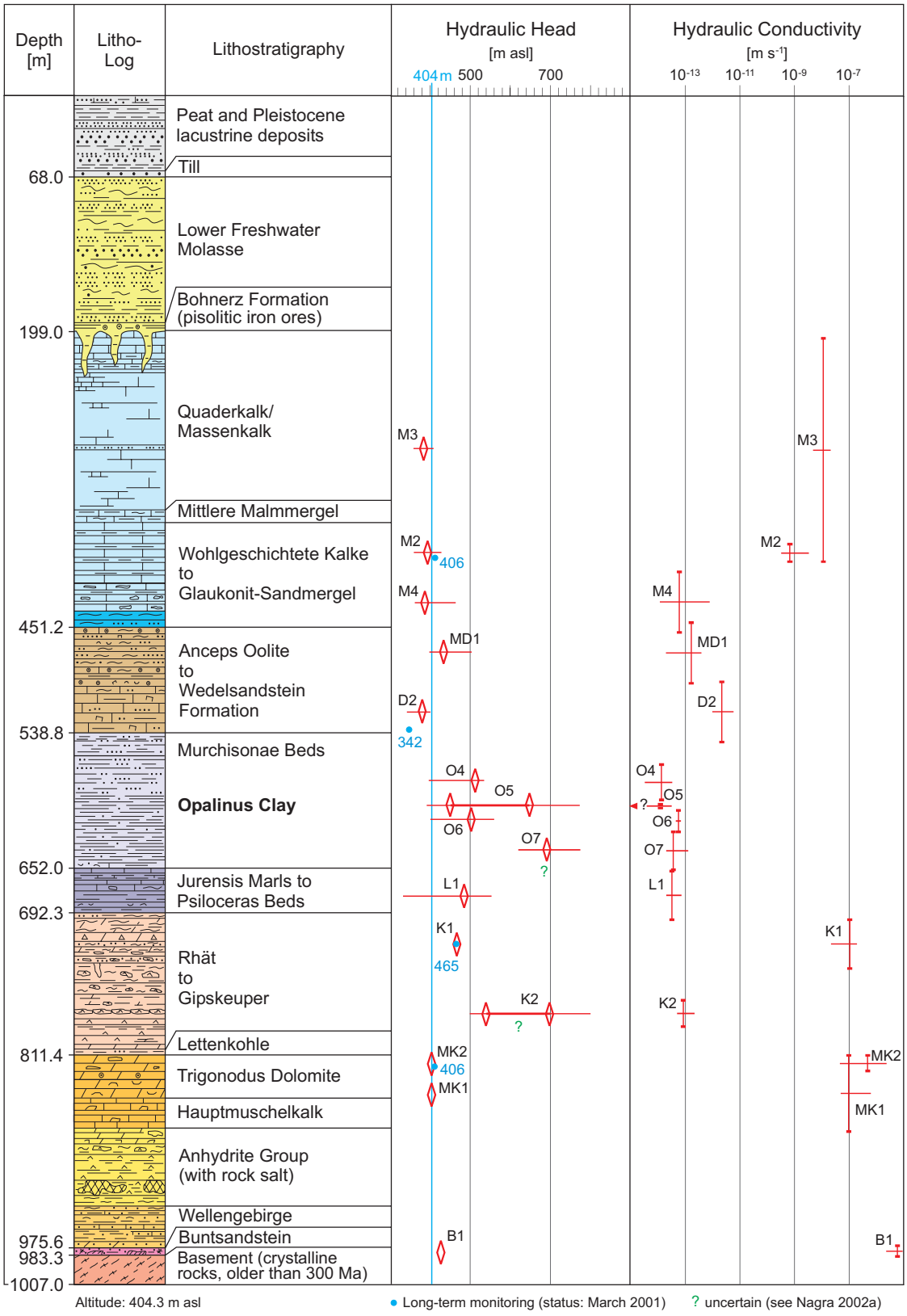

Figure 3: Stratigraphy, hydraulic pressures, and hydraulic conductivities as observed in the Benken borehole.

Modified from Nagra 2002.

3 Deep ground water at Benken

As mentioned in the introduction, in this report we use the term ground water to denote freely flowing water in an aquifer and the term pore water to denote water from low-permeability zones. In the Benken borehole, deep ground water could be collected from packed-off intervals in lithologies of the Malm, Keuper, Muschelkalk and Buntsandstein. Table 1 gives the depth of the hydraulic test intervals, the names of which were used for the designation of the ground water samples, the hydraulic conductivity of the water-producing zones, and their lithology and stratigraphic assignment. The research character of the deep borehole required the use of several different, traced drilling fluids in order to minimise induced perturbations of the *in situ* hydraulic and hydrochemical conditions (Nagra 2000). As a consequence, the gathered hydrochemical raw data have to be carefully examined for contamination by drilling fluid prior to their interpretation.

Table 1: Location of ground water samples and stratigraphy, lithology, and hydraulic conductivity of the water-producing zones in the Benken borehole (from Nagra 2000).

Epoch	Stratigraphy	Test Interval	Depth (m)	Lithology	Hydraulic Conductivity ($m\ s^{-1}$)
Malm	Wohlgeschichtete Kalke	M2	379.9 – 394.8	limestone	6.7×10^{-10}
Keuper	Stubensandstein	K1	698.0 – 739.2	dolomite-breccia, sandstone	9.7×10^{-8}
Muschelkalk	Trigonodus-Dolomite	MK2	813.0 – 826.0	dolomite, limestone	4.6×10^{-7}
Buntsandstein	Buntsandstein	B1	974.3 – 983.0	conglomeratic sandstone	5.7×10^{-6}

3.1 Evaluation of contamination by drilling fluid and sample procedures

Tracer contents were monitored continuously and control samples were taken periodically during pumping of water for hydrochemical sampling. In productive water-conducting zones drilling fluid is normally flushed by the *in situ* ground water within hours and tracer contents fall to levels of < 1 percent which are acceptable for hydrochemical sampling. This was the case for ground water from the Keuper, Muschelkalk and Buntsandstein. In contrast, the Malm limestones yielded very little water and tracer contents remained high even after several days of pumping at low rate ($< 1.5\ L\ min^{-1}$). It should be noted that for different analyses (e.g. chemistry, dissolved gases, noble gases, radioisotopes) different sampling procedures and vessels were used that could have been subjected to different types of contamination. For instance, slight air contamination of the large water samples collected for gas analyses is possible because the shape of the collection vessels may have made it difficult to entirely remove air bubbles inadvertently trapped in the vessel during sampling. This explains the apparent inconsistency e.g. of measurable dissolved oxygen and the in-line measured reducing redox potential for some ground water samples (see below and Table 3). It further explains the differences in air contamination observed between dissolved gas samples, the water samples with large volumes to be vacuum-extracted for ^{85}Kr and ^{39}Ar, and noble gas samples (see

below), the latter being collected in straight-sided copper tubes where trapping of air bubbles is much less likely. The complete drilling-fluid and ground-water data including the description of the correction procedure applied are given in Steffen et al. (2000) and Waber et al. (2002), respectively.

In the Malm limestones a clay-freshwater drilling fluid traced with uranine and the tritium activity of the water from the community's water supply (17.9 TU) was used. The correlation between tritium and uranine in drilling fluid, control samples and water samples is strong and passes through the origin, within the uncertainty of the data. This indicates that the tritium content of the formation water is zero and thus that the Malm contains no modern water. Evaluation of the tracer contents in the various water samples revealed a contamination of 23.3 %. Corrected for contamination this results in a chloride content of the *in situ* Malm ground water of about 4 550 mg L^{-1}. The overall error of this value is estimated to be about 10 %. The same correction procedure was also applied for all solutes and the isotope compositions of oxygen and hydrogen, while for the chlorine isotopic composition no correction could be applied due to the lack of data for the drilling fluid. However, the *in situ* ground water δ^{37}Cl-value is likely to be slightly more positive than measured (0.31 ‰) because modern ground water as used for the drilling fluid preparation commonly has negative δ^{37}Cl-values (range about –0.3 ‰ to –1.5 ‰; Sie & Frape 2002; Coleman et al. 2003).

The resulting corrected Malm ground water is denoted as BEN-M2c. It is recognised that a linear correction of such a high contamination is strictly only valid for non-reactive dissolved constituents and that the extent to which the concentrations of reactive constituents were perturbed by chemical reactions with the drilling fluid (e.g. with bentonite) cannot be fully resolved. In combination with regional geologic and palaeohydrologic knowledge, however, valuable information can nevertheless be obtained from such a corrected analysis in spite of the increased uncertainty.

In the Keuper lithologies core drilling was done with a sodium-silicate drilling fluid (29 % SiO_2, 14 % Na_2O). The uranine concentration dropped rapidly and the contamination by drilling fluid was below 1 % during sampling of the Keuper ground water BEN-K1. Therefore, contamination is within the analytical error of the analyses, except for the concentrations of sodium and silicon, which might be slightly outside the analytical error band.

In the Muschelkalk lithologies core drilling was performed with a highly mineralised sodium-silicate drilling fluid to a depth of 814 m, followed by clay-freshwater drilling fluid to 918 m of depth where the occurrence of rock salt required the use of a Na-Cl-brine drilling fluid for further drilling. Sampling of the Muschelkalk water occurred prior to the change in drilling fluid. Although the tracer concentrations were between 0.85 – 0.6 % during sampling, it was recognised that rock salt dissolution had already modified the drilling fluid-ground water mixture as indicated by a decrease in the Cl content between sample BEN-MK2 (75 mg L^{-1}) and a control sample (21.8 mg L^{-1}) taken some 24 hours later. Therefore, the *in situ* Muschelkalk ground water is expected to have lower Cl and Na contents than measured for sample BEN-MK2 while the other parameters remain unchanged within the analytical uncertainty.

There were similar effects on the chemistry of the Buntsandstein ground water. The requirement of a Na-Cl-brine drilling fluid with about 176 g L^{-1} Cl influenced the concentrations of Na and Cl in the ground water sample BEN-B1 in spite of the low tracer content (0.15 % and 0.10 %). Extrapolation to zero contamination yields a Cl^- content of about 225 – 252 mg L^{-1} with a corresponding Na^+ content of about 391 – 408 mg L^{-1} for the *in-situ* ground water in the Buntsandstein, while the other parameters remain unchanged within the analytical uncertainty.

Rock salt dissolution and the Na-Cl brine drilling fluid also affected the Cl-isotope composition of the Muschelkalk and Buntsandstein water samples. Halite from Triassic formations in the Benken drill core has positive δ^{37}Cl-values (Waber et al. 2001) and so has brine chloride (Kaufmann et al. 1984; Eggenkamp et al. 1995). Even a small contribution of Cl from such sources would significantly alter the *in situ* signature and it is therefore likely that the Muschelkalk and Buntsandstein ground water have δ^{37}Cl-values that are below those measured.

3.2 Ground water composition

3.2.1 Chemistry and mineral saturation

The four deep ground waters sampled from the Benken borehole have distinct chemical and dissolved gas compositions (Tables 2 and 3). Ground water from the Malm and the Keuper have a similar total mineralisation of about 10 g L^{-1}, but are of a different chemical type. The Malm ground water is of the Na-Cl-(SO_4) type with a Cl content of about 4 550 ± 455 mg L^{-1}. The Keuper ground water is of the Na-SO_4-(Cl) type with sulphate as the dominant anion and a Cl content of only about 520 mg L^{-1} (Figure 4).

Ground waters from the Muschelkalk and the Buntsandstein are distinctly less mineralised with a total mineralisation of 2.4 g L^{-1} and 1.4 g L^{-1}, respectively (Table 2). The Muschelkalk ground water is of the Ca-Mg-SO_4-(HCO_3)-type, while the Buntsandstein ground water is of the Na-HCO_3-Cl-(SO_4)-type (Figure 4). Both ground waters have a major component composition comparable to other ground water from the same aquifers in the region (Biehler et al. 1993; Schmassman et al. 1992). The Muschelkalk ground water composition is dominated by alkaline-earth elements while that of the Buntsandstein has high ratios of alkali to alkaline-earth elements and high contents of fluoride and lithium.

All four deep ground waters have an inline-measured reducing redox potential (Eh from -121 mV to –560 mV SHE, pε from –2.11 to –9.83 at formation temperature, respectively). Reducing conditions are also indicated by the redox potentials calculated from analytical concentrations of members of several redox pairs (Table 3). This is consistent with the occurrence of well-preserved pyrite in vugs and fractures within the four water-conducting formations. The occurrence of dissolved oxygen in some sub-samples (see next paragraph), however, has to be attributed to contamination during sampling (cf. 3.1).

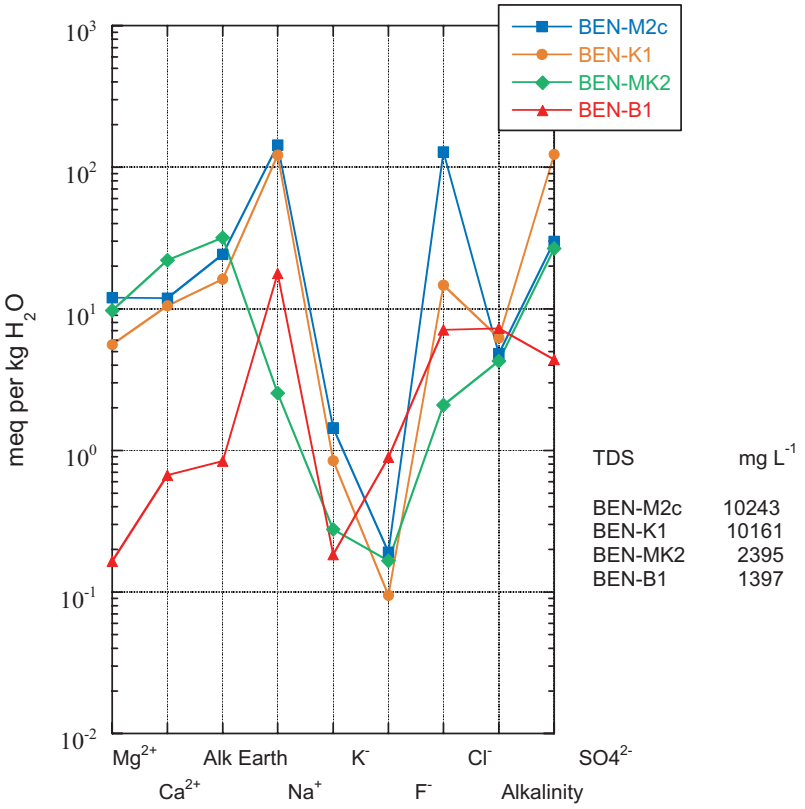

Figure 4: Schoeller diagram of deep ground waters from Benken borehole highlighting the distinct chemical compositions.

Dissolved gases are dominated by nitrogen followed by carbon dioxide in all deep ground water samples. In three aquifers the molar N_2/Ar ratios of samples taken for dissolved gas analysis are in a range between 59 to 78 (Waber et al. 2002). This range is considerably above the value for water in equilibrium with air at 10 °C and 1 bar (N_2/Ar ratio of 38), which represents approximately infiltration conditions. Only the Muschelkalk water appears to have kept its infiltration ratio of 38. This suggests an additional source of nitrogen in the surrounding rocks. The contaminated Malm sample is oxygen-free, while the samples of the other three ground waters are slightly contaminated with oxygen. Dissolved oxygen in these samples is inconsistent with the overall redox characteristics of the ground waters (measured and calculated redox potentials, occurrence of methane and higher hydrocarbon gas) and is considered as an artefact.

As Table 3 illustrates, when mineral equilibrium calculations are made at formation temperatures using the measured pH values, all waters appear to be strongly supersaturated with respect to calcite. Based on the source of these waters in carbonate-bearing sedimentary formations and the absence of measurable tritium (see below), all can be expected to be in calcite equilibrium. Thus, calculations were also made at pH values leading to calcite saturation. At calcite equilibrium, the four ground waters are also in equilibrium with the major rock-forming and vein minerals in the formations from which they were sampled (Table 3). In addition, the Buntsandstein ground water is supersaturated with respect to fluorite, which is abundant in the underlying crystalline rocks. Supersaturation with respect to barite of the ground water samples from the Malm, Keuper and Muschelkalk is attributed to contamination by drilling fluid to which barite was an additive. The Buntsandstein ground water is close to saturation with respect to barite, consistent with occurrence of barite as fracture mineral in this lithology.

3.2.2 Isotope composition

As in their chemical composition, the four ground waters also display distinct differences in their isotope composition (Table 4). The δ^2H- and $\delta^{18}O$-values of Malm ground water plot far to the right of the Global Meteoric Water Line, GMWL, while the water isotopic compositions of the other ground waters fall close to or on the GMWL and the Local Meteoric Water Line (Figure 5). Thus, the different oxygen and hydrogen isotopic compositions indicate formation-specific conditions of infiltration and, for the Malm ground water, possibly also a different geochemical evolution. Significant differences in the isotopic compositions of dissolved Cl ($\delta^{37}Cl$) and Sr ($^{87}Sr/^{86}Sr$) and differences in the isotopic compositions of dissolved inorganic carbon ($\delta^{13}C_{DIC}$) and sulphate ($\delta^{34}S_{SO4}$, $\delta^{18}O_{SO4}$) indicate a formation-specific geochemical and hydraulic evolution.

Tritium was below detection limit in the ground water from the Keuper, Muschelkalk and Buntsandstein (Table 4). The measured activities of ^3H and ^{14}C in the contaminated Malm ground water sample (3.5 ± 1.3 TU and 4.4 ± 0.5 pmc, respectively) stem from the 23 % contamination with drilling fluid and the *in situ* Malm ground water is free of ^3H and ^{14}C. Ground waters from the Keuper and the Buntsandstein are also free of ^{14}C, while the ^{14}C activity of the Muschelkalk ground water was 2.3 pmc with an associated $\delta^{13}C$ of total dissolved inorganic carbon (DIC) of about -6.5‰ PDB.

The Muschelkalk and the Buntsandstein ground water yielded measurable ^{85}Kr and ^{39}Ar (Table 4). The dissolved oxygen present in these samples indicates contamination by air of 5 – 10 %, which accounts for the measured ^{85}Kr activities and for the Muschelkalk ground water also for the measured ^{39}Ar activity. In the Bundtsandstein ground water the high ^{39}Ar activity cannot be attributed only to the observed air contamination. There, ^{39}Ar stems from underground production as indicated by a rapidly processed sub-sample that contained measurable ^{37}Ar, which is indicative of underground production. High concentrations of ^{39}Ar in Buntsandstein waters are not unusual and have been found in samples from this formation elsewhere in northern Switzerland (Loosli & Lehmann 1991). They are attributed to the interaction of Buntsandstein waters with water from the underlying crystalline basement where there is a high rate of ^{39}Ar production. For both ground water samples contamination by air and underground production, respectively, inhibit the derivation of a ^{39}Ar residence time.

3.2.3 Noble gases

For the ground waters from the Muschelkalk and Buntsandstein the entire set of noble gas data (Table 5) gives no evidence of any significant contamination of the noble gas sample by air and the analysed concentrations appear to be representative for *in situ* conditions. In contrast, the concentrations of Kr and especially Xe are surprisingly low in the Malm and Keuper ground water without any obvious experimental reason.

All ground waters have He concentrations that are four orders of magnitude higher than in air-equilibrated water (4.650×10^{-8} STP cm^3 g^{-1} at 10 °C at sea level) except for the Muschelkalk ground water, which has a He concentration only one order of magnitude higher (Table 5). The Ar concentrations are similar in all ground waters and without exception higher than that of air-equilibrated water (3.860×10^{-4} STP cm^3 g^{-1} at 10 °C at sea level). The $^3He/^4He$ ratios are high with the lowest ratio recorded for the Buntsandstein ground water. Similarly, the $^{40}Ar/^{36}Ar$ ratios are high in the ground waters and all are above that of air-equilibrated water (295.5 at 10 °C at sea level). The lowest $^{40}Ar/^{36}Ar$ ratio measured was that of the Muschelkalk ground water (Table 5).

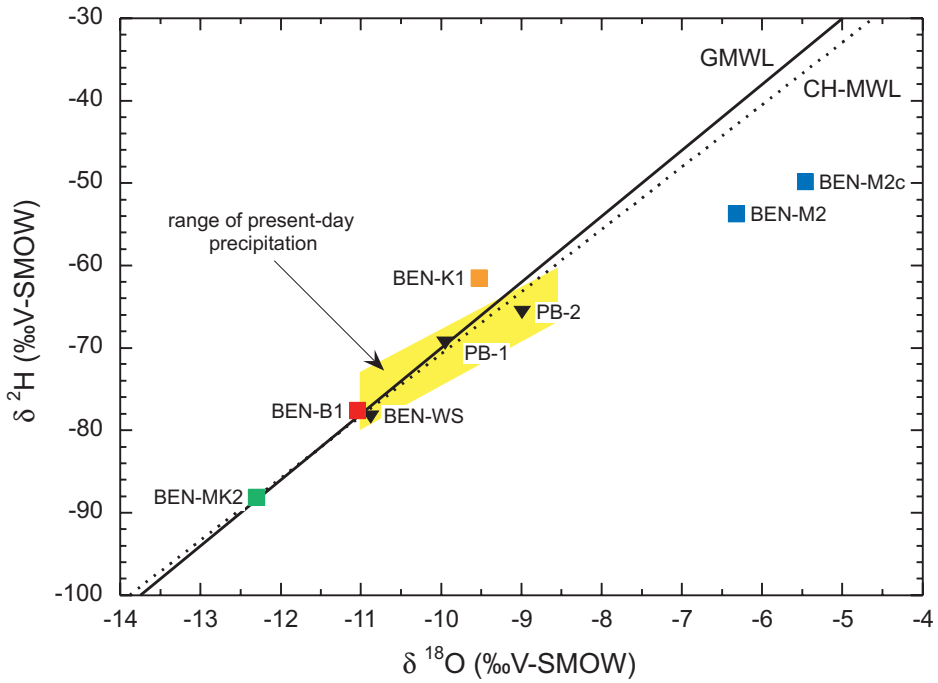

Figure 5: Diagram of $\delta^{18}O$ vs. $\delta^{2}H$ of deep ground waters sampled in the Benken borehole.

Also given are the Global Meteoric Water Line (GMWL), the range of present-day precipitation, the meteoric water line for the Swiss Midland (CH-MWL, Kullin & Schmassman 1991), and three shallow ground waters sampled near-by the deep borehole (PB-1, PB-2, and BEN-WS; WS = water supply). BEN-M2 is the isotopic composition of the Malm ground water as sampled, BEN-M2c is that corrected for contamination with drilling fluid (cf. Section 3.1).

Table 2: Hydrochemical data of deep ground water in the Benken borehole corrected for contamination by drilling fluid (*: indeterminate slight contamination by drilling fluid, see text; for complete heavy metal analyses see Nagra 2000).

[1)] pH and Eh(SHE) are uncorrected in-line measurements; Eh in Malm water possibly influenced by interaction with drilling tools and casing

Sample	Units	BEN-M2c	BEN-K1	BEN-MK2	BEN-B1
Aquifer		Malm	Keuper	Muschelkalk	Buntsandstein
Type of Sample		deep gw	deep gw	deep gw	deep gw
Date Sampled		24.09.1998	06.02.1999	12.04.1999	29.04.1999
Depth	m	379.9-394.8	698-0-739.22	813.0-826.01	974.30-983.03
Uranine	ppm	0 %	0.01-0.001	≤ 0.0074	0 %
Contamination		corrected	< 1 %	< 1 %	corrected
Water Type		Na-Cl-(SO4)	Na-SO4-(Cl)	Ca-Mg-SO4-(HCO3)	Na-HCO3-Cl-(SO4)
pH (field) [1)]			8.70	8.12	8.48
pH (lab)		8.8	8.30	8.20	8.50
El. Conductivity	µS cm^{-1}	15 418	11 590	2 628	2 970
Eh (SHE) [1)]	mV	-560	-190	-121	-247
Sample Temperature	°C	14	15.7	16.1	21.4
Formation Temp.	°C	23.6	42.2	46.0	50.6
Lithium (Li+)	mg L^{-1}		1.7	0.11	0.86
Sodium (Na+)	mg L^{-1}	3 290	2 800 *	59 *	408
Potassium (K+)	mg L^{-1}	56	33.1	11	7.2
Rubidium (Rb+)	mg L^{-1}		0.032	0.039	0.055
Ammonium (NH4+)	mg L^{-1}	1.5	4.2	0.08	0.2
Magnesium (Mg+2)	mg L^{-1}	145	67.9	120	2
Calcium (Ca+2)	mg L^{-1}	238	210	448	13.4
Strontium (Sr+2)	mg L^{-1}	15.4	7.5	5.6	0.33
Barium (Ba+2)	mg L^{-1}	0.097	0.046	0.046	0.057
Manganese (Mn+2)	mg L^{-1}	0.55	0.081	0.35	0.11
Iron (Fe+2)	mg L^{-1}	9.0	1.1	22.2	3.2
Iron (Fe+3)	mg L^{-1}	40	3.2	2.2	< 0.1
Arsenic (As+3)	mg L^{-1}	-	0.0033	< 0.0005	0.034
Arsenic (As+5)	mg L^{-1}	-	0.0006	0.0025	0.0021
Aluminium (Al)	mg L^{-1}	-	0.038	0.038	0.018
Uranium (U)	mg L^{-1}	-	< 0.0002	< 0.0002	n.a.
Fluoride (F-)	mg L^{-1}	3.6	1.8	3.2	17
Chloride (Cl-)	mg L^{-1}	4 550	520 *	75.2 *	252
Bromide (Br-)	mg L^{-1}	7.0	0.97	< 0.05	0.33
Iodide (I-)	mg L^{-1}	4.5	0.37	< 0.01	0.01
Sulfate (SO4-2)	mg L^{-1}	1 437	5 900	1 300	210
Phosphate (P)	mg L^{-1}	-	0.09	< 0.05	< 0.05
Nitrate (NO3-)	mg L^{-1}	-	< 0.1	< 1	< 1
Nitrite (NO2-)	mg L^{-1}	-	0.09	0.02	0.05
Tot. Alkalinity (field)	eq L^{-1}	-	4.80E-03	4.80E-03	7.60E-03
Tot. Alkalinity (lab)	eq L^{-1}	-	6.05E-03	4.35E-03	7.30E-03
Tot. Alk. as HCO3-	mg L^{-1}	294	369	266	445
Tot. Sulfide	mg L^{-1}	0.21	< 0.03	< 0.03	< 0.03
H2SiO3	mg L^{-1}	12.2	190 *	53	28
Borate (H3BO3)	mg L^{-1}	20.8	22	1	3.5
Organic C (DOC)	mg L^{-1}	94	2.7	2	1.6
Total Org. C (TOC)	mg L^{-1}	156	4.2	2	1.6
Total Diss. Solids	mg L^{-1}	10 243	10 161	2 395	1 397
Charge Balance	%	0.87	–0.75	1.66	–0.86
Ionic Strength	mol kg^{-1}	1.830E-01	1.796E-01	4.448E-02	2.127E-02

Table 3: Modelled carbonate and redox system, gas partial pressures, and mineral saturation states of deep ground waters at formation temperature in the Benken borehole; calculations were performed using the Nagra/PSI database 01/01 (Hummel et al. 2002).

Sample	BEN-M2c	BEN-K1	BEN-MK2	BEN-B1
Aquifer	Malm	Keuper	Muschelkalk	Buntsandstein
Water Type	Na-Cl-(SO4)	Na-SO4-(Cl)	Ca-Mg-SO4-(HCO3)	Na-HCO3-Cl-(SO4)
Carbonate system measured values				
Formation Temperature (°C)	23.6	42.2	46.0	50.6
pH	8.8	8.3	8.2	8.5
Total Alkalinity (eq L^{-1})		6.05E-03	4.35E-03	7.30E-03
Modelled using measured pH				
Total Dissolved CO_2	3.869E-03	5.367E-03	3.798E-03	6.801E-03
SI calcite	1.45	1.13	1.60	0.82
log $P(CO_2)$	-3.67	-2.82	-2.82	-2.77
Modelled using pH adjusted for calcite saturation				
pH	7.15	7.08	6.51	7.57
Total Dissolved CO_2	5.302E-03	6.604E-03	5.987E-03	7.491E-03
log pCO_2	-1.83	-1.52	-1.04	-1.79
Mineral saturation indices (log IAP/KT) at calcite saturation				
Calcite	0.00	0.00	0.00	0.00
Dolomite_ord	0.13	-0.04	-0.06	-0.24
Magnesite	-0.15	-0.79	-0.90	-1.18
Fluorite	-0.01	-1.03	0.08	0.26
Anhydrite	-0.94	-0.45	-0.35	-2.27
Gypsum	-0.71	-0.33	-0.25	-2.21
Strontianite	-0.72	-1.06	-1.53	-1.26
Witherite	-3.94	-4.42	-4.68	-3.01
Celestite	-0.17	-0.02	-0.40	-2.05
Barite	0.67	0.42	0.20	-0.11
Chalcedony				
Quartz	-0.02	0.95	0.33	0.01
Redox at formation temperature		pε	pε	pε
N^2 / NH^{4+}		-3.96	-2.75	-4.28
As^{+5} / As^{+3}		-1.21		-2.40
CO_2 / CH_4		-4.35	-3.76	-5.03
$H_{2(aq)}$ / H^+				-6.18
Gas partial pressures at formation temperature		log	log	log
CH_4		-2.89	-3.05	-2.21
CO_2		-1.52	-1.04	-1.79
N_2		-0.01	-0.10	0.15
O_2		-1.72	-1.51	-1.13

Table 4: Isotope data of deep ground waters in the Benken borehole corrected for contamination by drilling fluid where necessary (b.d.l.: below detection limit; *: no correction possible due to the component's reactivity and the lack of drilling fluid data).

Sample	Units	M2/1	BEN-M2c	BEN-K1	BEN-MK2	BEN-B1
Aquifer		Malm	Malm	Keuper	Muschelkalk	Buntsandstein
Type of Sample		deep gw	deep gw	deep gw	deep gw	deep gw
Date Sampled		24.09.1998	24.09.1998	06.02.1999	12.04.1999	29.04.1999
Depth	m	379.9-394.8	379.9-394.8	698-0-739.22	813.0-826.01	974.30-983.03
Uranine	ppm	0.114	corrected	0.01-0.001	≤ 0.0074	0.0014
Contamination with drilling fluid		ca 23 %	0 %	< 1 %	< 1 %	< 1 %
Water Type		-	Na-Cl-(SO4)	Na-SO4-(Cl)	Ca-Mg-SO4-(HCO3)	Na-HCO3-Cl-(SO4)
δ^2H H_2O	‰ V-SMOW	-53.4	-49.88	-63.2	-88.1	-77.6
$\delta^{18}O$ H_2O	‰ V-SMOW	-6.32	-5.46	-9.53	-12.3	-11.04
^3H	TU	3.5 ± 1.3	b.d.l.	< 0.6	< 0.6	< 0.6
^{14}C	pmc	4.4 ± 0.5	b.d.l.	< 0.5	2.3 ± 0.6	< 0.6
$\delta^{13}C$ TIC	‰ V-PDB	-0.79	-0.79 *	-8.3	-6.4	-5.8
$\delta^{34}S$-H_2S	‰ CD					
$\delta^{34}S$-SO_4	‰ CD	20.8	20.8 *	15.54	15.9	16.5
$\delta^{18}O$-SO_4	‰ V-SMOW	13.9	13.9 *	16.34	11.1	1.3
^{87}Sr / ^{86}Sr		0.707518 ±0.000020	0.707518 ±0.000020	0.708817 ±0.000055	0.708304 ±0.000030	0.714847 ±0.000090
Sr	ppm	13.9	13.9		6.5	0.327
$\delta^{37}Cl$	‰ SMOC	0.31 ± 0.15	0.31 ± 0.15	-0.92 ± 0.15	-0.13 ± 0.15	0.17 ± 0.15
^{85}Kr	dpm cm^{-1}				4.5 ± 1.5	0.4 ± 0.04
^{39}Ar	% modern				10 ± 6	68 ± 7
^{37}Ar	dpm L^{-1} Ar				0.050 ± 0.006	

Table 5: Noble gas data of deep ground waters in the Benken borehole corrected for contamination by drilling fluid where necessary.

Sample Aquifer	Units	BEN-M2/1 Malm	BEN-M2c Malm	BEN-K1 Keuper	BEN-MK2 Muschelkalk	BEN-B1 Buntsandstein
Type of Sample Date Sampled		deep gw 24.09.1998	deep gw 24.09.1998	deep gw 06.02.1999	deep gw 12.04.1999	deep gw 29.04.1999
Depth	m	379.9-394.8	379.9-394.8	698-0-739.22	813.0-826.01	974.30-983.03
Uranine Contamination with drilling fluid	ppm	0.114 ppm ca 23 %	0 % corrected	0.01-0.001 < 1 %	≤ 0.0074 < 1 %	0 % < 1 %
Water Type		-	Na-Cl-(SO4)	Na-SO4-(Cl)	Ca-Mg-SO4-(HCO3)	Na-HCO3-Cl-(SO4)
He	STP cm g^{-1}	2.470E-04 ± 1.445E-06	3.207E-04 ± 1.604E-05	2.071E-04 ± 7.492E-07	5.605E-07 ± 1.323E-09	1.470E-04 ± 5.340E-07
Ne	STP cm g^{-1}	2.380E-07 ± 3.138E-09	2.564E-07 ± 1.282E-08	2.152E-07 ± 2.212E-09	2.963E-07 ± 3.049E-09	2.771E-07 ± 2.913E-09
Ar	STP cm g^{-1}	3.922E-04 ± 2.149E-06	4.206E-04 ± 2.103E-05	4.078E-04 ± 3.722E-06	4.769E-04 ± 4.302E-06	4.949E-04 ± 4.416E-06
Kr	STP cm g^{-1}	7.440E-08 ± 6.113E-10	7.681E-08 ± 3.841E-09	8.809E-08 ± 1.215E-09	1.102E-07 ± 1.561E-09	1.164E-07 ± 1.569E-09
Xe	STP cm g^{-1}	7.325E-09 ± 1.173E-10	6.808E-09 ± 3.404E-10	9.858E-09 ± 1.216E-10	1.577E-08 ± 2.006E-10	1.629E-08 ± 2.069E-10
^{40}Ar / ^{36}Ar		319.7 ± 0.38	325.3 ± 3.25	306.4 ± 0.45	296.2 ± 0.36	300.2 ± 0.28
$^{3}He/^{4}He$ x 10^{-7}		3.66 ± 0.005	3.66 ± 0.005	4.25 ± 0.009	4.11 ± 0.008	0.66 ± 0.002
^{20}Ne / ^{22}Ne		9.748 ± 0.015	9.748 ± 0.015	9.734 ± 0.008	9.769 ± 0.013	9.764 ± 0.021

3.3 Solute origin and water-rock interaction

The four ground waters sampled from different depths and lithologies in the Benken borehole are geochemically evolved as can be seen from their mineralisation, mineral saturation states and isotope compositions. Comparison of the chemical and isotope data of the ground waters to those of the rocks from which they were sampled allows the evaluation of the solute origin and of the chemical and isotopic equilibrium state between ground water and rock. Such comparison further reveals whether the ground waters have mainly evolved in the lithology from which they were sampled or if they have seen different lithologies and/or mixed with other ground-water types during their evolution.

3.3.1 Malm ground water

At formation temperature (23.6 °C), the Na-Cl-(SO_4)-type Malm ground water if assumed to be in chemical equilibrium with calcite is also in equilibrium with dolomite, fluorite, and celestite, all of which are known to occur in Malm limestones. The activities of dissolved Ca^{2+}, Mg^{2+}, CO_3^{2-}, F^-, and Sr^{2+} in this ground water are thus solubility controlled by the Malm rock mineralogy. The calculated high pCO_2 and neutral pH are also typical of waters that evolved mainly in a carbonate-rich environment (e.g. Coudrain-Ribstein et al. 1988).

The vein calcite that occurs in the Wohlgeschichtete Kalke Formation from which the Malm ground water was sampled is in carbon, oxygen and strontium isotope equilibrium with the ground water (Figures 6 and 7). The isotopic composition of dissolved sulphate, in contrast, falls between the ranges of compositions of Malm and Miocene mineral sulphate (Figure 8). All this is indicative of a long residence time in the formation from which the Malm ground water was sampled.

However, the major dissolved ions in the Malm ground water are not dominant in the solids of the Malm limestones and the mineralisation of the ground water with Na^+, Cl^-, and SO_4^{2-} is not related to interaction with the Malm limestones. Possible origins for these solutes are seawater and/or dissolution of evaporite minerals. Marine to brackish water was last present in the area during Tertiary times and local occurrences of anhydrite- and gypsum-bearing, but halite-free evaporite layers are described from the overlying Tertiary Molasse sediments (Trümpy 1980). A pure seawater origin can be excluded based on the total salinity, ion-ion ratios (e.g. Br/Cl, I/Cl, Na/Cl, SO_4/Cl) and isotopic signatures ($\delta^{18}O$, δ^2H), which differ from that of seawater. Similarly, an origin from pure evaporite dissolution is excluded by the absence of halite-bearing evaporite layers in the entire Molasse sequence. Therefore, the salinity of the Malm ground water at Benken has to be derived from a remnant of marine water, which became diluted by a meteoric component at a certain time in the evolution. This is in accordance with evolutionary models proposed earlier for Malm ground waters in the Molasse Basin in Switzerland (Balderer 1990) and southern Germany (Lemcke 1976; Udluft 1981). However, a simple two-component mixing of meteoric water and Tertiary seawater cannot account for the ground-water composition observed at Benken. This is based on incompatible mixing fractions calculated for conservative tracers such as Cl and $\delta^{37}Cl$, Br, $\delta^{18}O$, δ^2H, the $^{87}Sr/^{86}Sr$-ratio, and the origin of these dissolved constituents.

Chemical and isotopic composition of dissolved Cl and Sr indicate that the marine component in the Malm ground water at Benken is older than Tertiary seawater. At a Sr concentration about twice that of seawater, the $^{87}Sr/^{86}Sr$-ratio of the Malm ground water (0.707518) is below that of the typical Tertiary seawater signature (0.70765 – 0.70905; Veizer et al. 1997) and minerals precipitated from such seawater during the marine Molasse cycles. In contrast to the $^{87}Sr/^{86}Sr$-ratio, the Cl-isotope signature of seawater is believed to have remained stable at 0‰ SMOC over geologic times (Kaufmann et al. 1984; Eastoe et al. 2001). Meteoric low-Cl waters, on the other hand, have commonly negative $\delta^{37}Cl$-values. Therefore, the observed positive $\delta^{37}Cl$-value in the Malm ground water cannot be explained by advective mixing of old seawater component with meteoric water. Salt mineral dissolution, which can result in positive $\delta^{37}Cl$ ground water signatures (Eggenkamp et al. 1995), can also not explain the observed value because of the absence of halite-bearing layers in the Molasse sediments. Therefore, the positive $\delta^{37}Cl$ ground water signature has to be explained differently. Possibilities include Cl-isotope fractionation during transport of dissolved chloride as will be discussed in Section 6.2.

3.3.2 Keuper ground water

At the formation temperature (42.2ºC) the Na-SO_4-(Cl)-type Keuper ground water if assumed to be in chemical equilibrium with calcite is also in equilibrium with dolomite, celestite, barite, and quartz, but not with gypsum. All these minerals are known to occur in the continental sediments of the Upper Keuper (Nagra 2000). The activities of dissolved Ca^{2+}, Mg^{2+}, CO_3^{2-}, Ba^{2+}, Sr^{2+}, and $SiO_{2(aq)}$ are thus solubility controlled by the rock mineralogy.

In the Keuper ground water the dominant anion, SO_4^{2-}, is derived from dissolution of highly soluble gypsum and anhydrite in the Upper Keuper lithologies. In spite of Ca-sulphate mineral dissolution, however, the major dissolved cation is sodium. Cation exchange reactions with clay

minerals, the solubility control of Ca^{2+} and Mg^{2+} by carbonate minerals and, as suggested from the chloride isotopes (see below) possibly also interaction with the pore water in the overlying claystones account for this. The clay contents of the water-conducting zones in the Keuper are variable, but may reach up to more than 50 % in certain layers (Nagra 2000). In spite of their continental origin, the clays in these layers still have a Na-dominated exchange population (Waber et al. 2003) because of their evolution in an evaporite environment.

The vein calcite that occurs in the Stubensandstein Formation from which the Keuper ground water was sampled is in carbon, oxygen and strontium isotope equilibrium with the water (Figure 6). The water is also in strontium isotopic equilibrium with the rocks from which it was sampled (Figure 7) and the sulphate isotope composition falls within the range of that given by sulphate minerals from Keuper lithologies (Figure 8). The $\delta^{37}Cl$ obtained for the Keuper ground water is significantly negative and might be indicative of meteoric water. However, meteoric water has a much lower total Cl concentration so that an additional Cl source must have contributed to the Keuper ground water. Halite from underlying Triassic formations can be excluded as such a source based on its positive $\delta^{37}Cl$-values (Waber et al. 2001).

Chemical and isotopic composition of the Keuper ground water therefore suggest a meteoric water that evolved within the Keuper lithology from which it was sampled. The chemistry and carbon and sulphate isotope compositions suggest that de-dolomitisation reactions played an important role in this ground water evolution beside cation exchange reaction. The Cl (and possibly also Na) content and Cl isotope signature can only be explained by alteration via interaction with the pore water of the overlying argillaceous rock sequence.

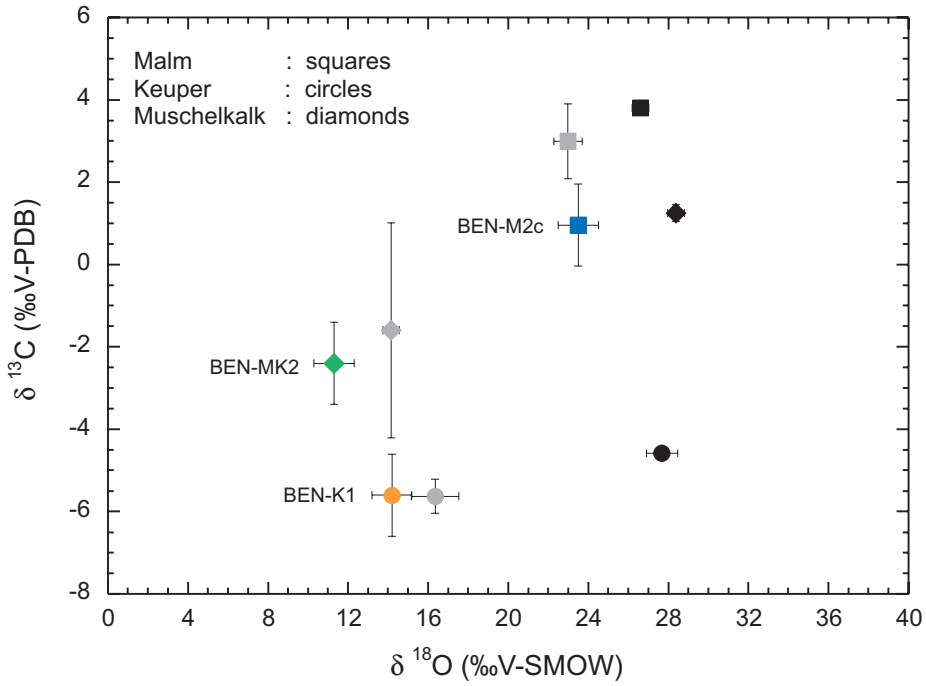

Figure 6: Isotopic composition of carbonate in whole rock, calcite from open veins, and dissolved inorganic carbon in isotope equilibrium with calcite under formation conditions.

Black: carbonate in whole rock; grey: calcite from open veins; coloured: dissolved inorganic carbon. The isotopic composition of the latter was calculated from the measured ground water values given in Table 4 and using the fractionation factors of Clark & Fritz (1997).

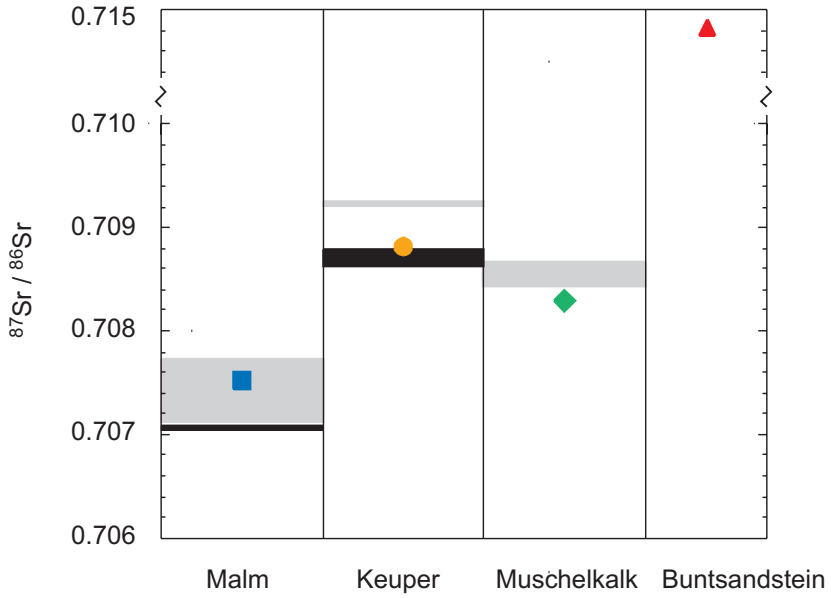

Figure 7: $^{87}Sr/^{86}Sr$ in the carbonate fraction of the whole rock, vein carbonates, and ground water.

Black areas: carbonate fraction of whole rock; grey areas; vein carbonates; coloured symbols: ground water. The data indicate Sr-isotope equilibrium between ground water and whole rock and vein minerals, respectively.

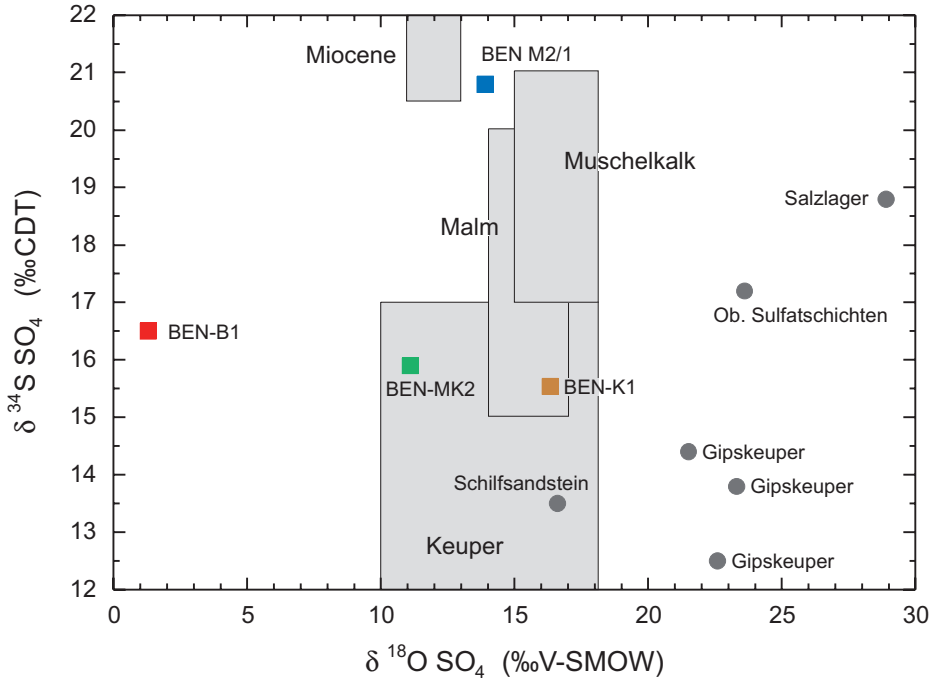

Figure 8: Isotope composition of dissolved sulphate and sulphate minerals from the Benken borehole.

Squares: dissolved sulphate; circles: sulphate minerals from Keuper and Muschelkalk Formations. Shaded areas are ranges of isotope compositions of sulphate minerals from designated areas in northern Switzerland and southern Germany (data from Balderer et al. 1991).

3.3.3 Muschelkalk ground water

The moderately mineralised Ca-Mg-SO_4-(HCO_3)-type Muschelkalk ground water indicates less interaction with the rock than the ground water in the overlying aquifers. At formation temperature (46.0 °C) if the ground water is assumed to be at chemical equilibrium with calcite it is also at equilibrium with dolomite, fluorite, and quartz, but not with gypsum. The major dissolved components are derived from the dissolution of calcite and dolomite (Ca^{2+}, Mg^{2+}, and HCO^{3-}), and gypsum and anhydrite (Ca^{2+}, SO_4^{2-}). These minerals all occur in the Trigonodus-Dolomite, which is the water-conducting zone in the Muschelkalk at Benken.

The carbonate dissolved in the ground water is in carbon isotopic equilibrium with vein carbonate minerals of the formation, but not in oxygen isotope equilibrium (Figure 6). Vein calcite of the formation and the present ground water would be at equilibrium at a formation temperature about 10 - 15 °C lower than that today.

The identical $^{87}Sr/^{86}Sr$ ratio of the Muschelkalk ground water and that of whole rock and vein carbonate indicates that the ground water derived its Sr isotope signature essentially from the formation from which it was sampled (Figure 7).

Muschelkalk water has a dissolved sulphate concentration about four times lower than Keuper ground water. The isotope composition of dissolved sulphate differs from the range given for Ca-sulphate minerals in the Muschelkalk from northern Switzerland (Figure 8). It appears that dissolved sulphate is not only derived from sulphate mineral dissolution, but also from the oxidation of pyrite. Pyrite is present in the formation, but its dissolution must have occurred at an early stage in the evolution because of the reducing redox conditions prevailing in the sampled ground water.

The low Cl content and a slightly negative $\delta^{37}Cl$-value below that of seawater are consistent with a mainly meteoric origin of Cl in this ground water. The chemical and isotopic composition of the Muschelkalk ground water are thus consistent with a meteoric water that evolved entirely within the formation from which it was sampled (i.e. the Trigonodus-Dolomite).

3.3.4 Buntsandstein ground water

The Na-HCO_3-Cl-(SO_4)-type ground water from the Buntsandstein differs from the ground waters sampled from the overlying limestone and evaporite rock formations. The high ratio of alkaline to alkaline earth elements is typical of evolution in more silico-clastic sediments such as sandstones. Calcite dissolution plays a subordinate role in the evolution of this water although it can still be assumed that calcite equilibrium is attained. More important seem to be reactions with aluminosilicates (affecting Na^+, K^+, $SiO_{2(aq)}$) and cation exchange with clays (affecting Na^+), although aluminosilicate equilibrium is not attained. Equilibrium is, however, attained with quartz and barite which are both observed in the Buntsandstein (Nagra 2000). The ground water is supersaturated with fluorite that occurs in the underlying crystalline basement as fracture infill. Note that this apparent supersaturation (SI = +0.26) is within the range of variability of equilibrium constants reported for this mineral (±0.55) (Hummel et al 2002 Section 5.3)

Interaction with crystalline rocks is also indicated by the highly radiogenic Sr-isotope ratio at low total Sr-concentration (Tables 2 and 4), both being typical for ground water of this formation in northern Switzerland (Matter et al. 1991). Dissolved sulphate differs markedly in its oxygen isotope composition in the other ground waters (Figure 8) and is similar to those of crystalline ground waters from northern Switzerland (Balderer et al. 1991). In combination with

the low concentration this suggests that the bulk of the dissolved sulphate is derived from pyrite oxidation, most probably in the underlying crystalline rocks.

3.4 Conditions of infiltration

The infiltration areas of the ground waters sampled in the Benken borehole are deduced from the outcrop areas and the regional hydraulic head distributions of the specific lithologies (see Section 2.2). These areas are mainly in the eastern and south-eastern foothills of the Black Forest mountain range at altitudes between about 500 m to 800 m above sea level (Figure 1; Traber et al. 2002). For the Malm aquifer, the combination of geological, hydrological and hydrochemical evidence indicates a more complex ground water flow pattern including a possible contribution from the Tertiary Molasse basin in the south (Balderer 1990; Traber et al. 2002).

3.4.1 Water isotopes

The ^{2}H and ^{18}O contents of rain water depend on the temperature, the dominant moisture source and the topography of the infiltration area. This allows to interpret the ^{2}H and ^{18}O contents of a sampled ground water in terms of the prevailing conditions under which it infiltrated. It has to be recognised, however, that an extrapolation to palaeo-infiltration temperatures is only valid as long as the dominant moisture sources and the topographic conditions remained stable over the time period considered.

The $\delta^{18}O$- and $\delta^{2}H$-values of the Malm ground water fall to the right of the GMWL (Figure 5). This trend can either be due to extensive rock-water interaction, evaporation (i.e. elevated temperature), mixture with sea water, or a combination of these three. In clay-poor rocks such as Malm limestones and Molasse sandstones extensive rock-water interaction would result mainly in enrichment in ^{18}O and produce a shift parallel to the x-axis in the $\delta^{18}O$ vs. $\delta^{2}H$ diagram. In contrast, evaporation effects shift the $\delta^{18}O$- and $\delta^{2}H$-values from the GMWL towards the right on trajectories with a slope of about 4 to 7, depending on the humidity of the air. The isotope composition of the Malm ground water cannot be explained by one single process alone. Most probably, the $\delta^{18}O$ and $\delta^{2}H$ value indicate a mixture of an old sea-water component with fresh water. In this area sea water was present for the last time during the Upper Marine Molasse (late Tertiary), when sub-tropical climatic conditions prevailed. Thus, it appears that at least this sea-water component infiltrated under warmer conditions than those present.

For the Keuper ground water the composition of stable water isotopes falls within the range of present-day precipitation and thus indicates that this ground water infiltrated under climatic conditions similar to the present ones.

The Muschelkalk ground water has significantly lower $\delta^{18}O$- and $\delta^{2}H$-values than present-day precipitation (Figure 5) that are indicative of infiltration of this ground water during cold climatic conditions and suggesting even a glacial melt water component in this water. During the Holocene and Pleistocene, the topography of the catchment area of the Muschelkalk water could not account for the measured values by the altitude effect.

The Buntsandstein ground water has a water isotope composition that falls just below the range of present-day precipitation (Figure 5). Because seasonal effects in the isotope composition are smoothed out in ground water, the $\delta^{18}O$- and $\delta^{2}H$-values of the Buntsandstein ground water indicate an infiltration under slightly cooler climatic conditions than the present ones.

3.4.2 Noble gases

Noble gases yield information about the temperature of infiltration during ground water recharge. In ground water noble gases originate from three major sources: 1) dissolution of atmospheric air according to solubility equilibrium, 2) addition of certain isotopes from radio-decay in the water or the aquifer rock (underground production), and 3) injection of "excess air". The first component depends on temperature, salinity, and atmospheric pressure during equilibration of the water and can thus be used to calculate the noble gas temperature (NGT) during infiltration (e.g. Kipfer et al. 2002). To enable the calculation of the NGT, this first component has to be corrected for the two other components. Underground production is of major importance for the contents of ^{3}He, ^{4}He, and ^{40}Ar. The underground production rate of these isotopes can be calculated from the concentrations of U, Th, Li, and K in the aquifer rock. For the third component, the "excess air", several correction models have been proposed (see discussion in Kipfer et al. 2002). The "excess air" correction model applied for the Benken deep ground waters is the CE Model proposed by Aeschbach-Hertig et al. (2000), which uses inverse methods to derive the NGT by fitting the STP-volume of dry "excess-air" and the degree of diffusive re-equilibration to the measured data for all noble gases.

The evaluation of an excess-air component indicates that the terrigenic He component (*in situ* produced He and a possible external earth crust/mantle source) makes more than 99 % of the total He for all samples, except for the Muschelkalk ground water (cf. discussion in Waber et al. 2002). The very high total He concentrations make an exact correction for excess air insignificant for all samples.

In all ground water samples the noble gas composition appears to be of predominantly terrigenic origin. This is indicated by the similarity of the $^{40}Ar_{rad}$ / $^{4}He_{rad}$ ratio in the ground water (0.11 ± 0.01, Waber et al. 2002) with that calculated for the in-situ production of the rock from the base of the Malm to the top of the Muschelkalk in the Benken borehole (0.11 ± 0.11, Lehmann et al. 2001).

The noble gas data of the Malm (contaminated and corrected) and Keuper ground water cannot be satisfactorily modelled with either model due to the very low concentrations of Kr and especially Xe. Strictly speaking, these data cannot be interpreted. Nevertheless, the data allow some indications if one accepts certain assumptions.

Based on the high salinity, the chemical Na-Cl-(SO_4) type and the isotopic compositions, the Malm ground water can be assumed to originate from seawater that became diluted with meteoric water during its evolution. Inconsistent NGTs calculated for Ar, Kr, and Xe argue against such an origin with the seawater and meteoric water having infiltrated under similar climatic conditions. More likely but with limited confidence, the noble gas data indicate a mixture of warm seawater (about 30 %) and cold fresh water (about 70 %) for the Malm ground water.

For the Keuper ground water the low concentrations of Xe result in large discrepancies between temperatures calculated for Xe (about 17 °C) and those calculated for Ar and Kr (about 7 °C to 9 °C). Rejecting the Xe data allows inverse fitting of the Ne, Ar, and Kr concentrations with pure excess air. The fits are reasonable and reveal consistent temperatures for these three noble gases (9.1 °C and 7.9 °C for an infiltration at 400 m a.s.l. and 700 m a.s.l., respectively), which are similar to those of the present-day climate. However, there is no obvious experimental reason to reject the Xe data.

For the ground waters from the Muschelkalk and Buntsandstein the CE Model can explain all atmospheric noble gas concentrations (Ne, Ar_{rad}, Kr, and Xe) within the analytical error (i.e.

< 1 %). The noble gas data are best fitted with an infiltration at about 700 m a.s.l. and a fractionated excess air component of 13.36 cm g^{-1} and 23.34 cm g^{-1}, respectively . This results in infiltration temperatures of 3.9 ± 0.5 °C for the Muschelkalk ground water and of 3.0 ± 1.2 °C for the Buntsandstein ground water. These temperatures are robust against uncertainties in infiltration altitude, salinity, and choice of noble gas model. Therefore, the NGTs indicate infiltration of these ground waters under significantly colder climatic conditions than those of the present.

3.4.3 Comparison of temperatures derived from water isotopes and noble gases

The relationship between the water-isotope composition of precipitation and temperature has been developed for the Swiss Midland ("CH-Mittelland") and Black Forest regions based on numerous precipitation monitoring stations in northern Switzerland and southern Germany (Kullin & Schmassmann 1991; Graf & Trimborn 1997). Table 6 compares the temperatures calculated using these equations and the measured δ^2H and $\delta^{18}O$ values of the Benken samples to the noble gas recharge temperatures. The isotopic composition of Malm ground water falls so far off the GMWL that neither equation is applicable.

For the Keuper ground water the range of calculated NGTs overlaps with the water-isotope infiltration temperature derived with the equation for the Black Forest region. The derived infiltration temperatures are thus consistent and fully support the current regional hydrogeological understanding (Nagra 2002, Chapter 3.6; Traber et al. 2002). When calculated with the "CH-Mittelland" equation, the isotopic composition of the Muschelkalk sample yields temperatures overlapping with the NGTs, while very low temperatures are obtained when using the equation for the Black Forest region. The latter suggest a glacial melt water component in this water. The Buntsandstein isotopic composition leads to temperatures overlapping NGTs when interpreted with the equation appropriate for the Black Forest region. Again, this is consistent with the regional hydrogeology.

Summarising, the evaluation of the climatic and topographic recharge conditions based on water isotopes and noble gases yields a consistent picture for the Keuper, Muschelkalk, and Buntsandstein ground water, which are in line with the current regional hydrogeological understanding (Nagra 2002, Chapter 3.6; Traber et al. 2002). Similar accounts for the Malm ground water, which is best interpreted as a mixture of water recharged under tropical and moderate climatic conditions. However, the data for this ground water cannot be interpreted in a more quantitative way.

3.5 Ground water residence times

The residence times of the deep ground waters at Benken can be evaluated from three types of data: 1) the activities of radioisotopes in the ground water, 2) the contents of isotopes that are produced in the subsurface by nuclear reactions (*in situ* production), and 3) information about the climatic conditions during ground-water infiltration as given in Section 3.4.

Ground waters from the four deep aquifers have no measurable ^3H and, except for the Muschelkalk ground water, no measurable ^{14}C (Table 3) indicating very long average residence times in the underground. The ^{14}C data of the three ^{14}C-free ground waters can thus be used at best only for evaluating minimum residence times. For the Malm ground water the uncertainty attached to the correction of the carbonate system for drilling fluid contamination precludes such an estimate. For the remaining ground waters the measured ^{14}C activities were corrected for dilution by ^{14}C-free carbonate from mineral dissolution based on the carbonate chemistry,

$\delta^{13}C_{TIC}$, and the available carbon isotope data from the rock, using the equations implemented in the geochemical code NETPATH (Plummer et al. 1994; for details see Waber et al. 2002). For the Keuper and Buntsandstein ground waters the calculated estimate of their minimum residence time is > 25 ka and > 26 ka, respectively. The measured ^{14}C content of the Muschelkalk sample is 2.3 ± 0.6 pmc. The possible range of residence times of this water considering the uncertainties in both the measured ^{14}C and the adjustment for the effects of water-rock reactions is from 12 to 22 ka. Best agreement with the measured ^{13}C contents of water and fracture calcite is obtained for a residence time of this water between 12 and 14 ka (for details see Waber et al. 2002).

Table 6: Comparison of temperatures calculated from noble gas concentrations (NGT) with those calculated from water isotope composition using equations of Kullin and Schmassmann (1991) for the Black Forest area, south Germany, and the Swiss Midland (CH-Mittelland).

Sample	Isotope temperature [°C]			Noble Gas Temperature (NGT) [°C]	
	Regional Equation	δ^2H	$\delta^{18}O$	Range	Comments
Shallow ground waters					
BEN-PB1	CH-Mittelland	9.0	8.3		
BEN-PB2	CH-Mittelland	9.9	10.0		
BEN-WS	CH-Mittelland	6.6	6.6		
Deep ground waters					
BEN-M2c		-	-	partly tropical partly moderate	data inconclusive
BEN-K1	CH-Mittelland	10.6	9.1		
	Black Forest	10.6	8.1	7.9 – 9.1	Xe excluded
BEN-MK2	CH-Mittelland	3.9	4.1	3.9 ± 0.5	all consistent
	Black Forest	-1.1	0.8		
BEN-B1	CH-Mittelland	6.7	6.4		
BEN-B1	Black Forest	3.8	4.1	3.0 ± 1.2	all consistent

The high concentrations of He and Ar and the high $^3He/^4He$ and $^{40}Ar/^{36}Ar$ ratios in the ground waters from the Malm, Keuper and Buntsandstein indicate that large amounts of He and Ar produced *in situ* in the surrounding rocks have accumulated in these ground waters. Thus, the ground waters must have been shielded from the atmosphere for a very long time and no mixing with a young ground water component can have occurred in recent past times. This is consistent with the ^3H and ^{14}C data of the three ground waters. The significantly lower He concentration in the Muschelkalk ground water and its $^{40}Ar/^{36}Ar$ ratio just above that of air-saturated water indicates a considerably lower underground residence time which is consistent with the presence of measurable ^{14}C in this ground water.

Table 7: Summary of the chemical and isotopic characteristics, conditions of infiltration and underground residence time of the deep ground waters sampled in the Benken borehole. The layers of low permeability (aquitards) between the aquifers are shown in grey.

Groundwater sample	Stratigraphy of the water-conducting zone	Chemical type	TDS [mg L^{-1}]	Cl [mg L^{-1}]	Br/Cl × 1 000 [molar]	^{4}He [STP cm^3 g^{-1}]	$^3He/^4He$ × 10^{-7}	$^{40}Ar/^{36}Ar$	Infiltration temperature [°C] [1]	Mean residence time [a]
air-saturated H_2O at 10 °C						4.65×10^{-8}		295.5		
seawater			35 164	19 353	1.5					
BEN-M2c	Malm (Wohlgeschichtete Kalke)	Na-Cl-(SO_4)	10 243	4 550	0.7	3.207×10^{-4}	3.66	325.3	partly ≈ 20 partly ≈ 10	very old ($\times 10^5 - \times 10^6$)
Aquitard (argillaceous rocks of the Dogger and Lias)										
BEN-K1	Keuper (Stuben- & Schilfsst.)	Na-SO_4-(Cl)	10 161	520	0.042	2.071×10^{-4}	4.25	306.4	ca. 7 to 9 (= present-day climate)	interglacial; > 25 000, < 2.6×10^6
Aquitard (evaporites of the Keuper)										
BEN-MK2	Muschelkalk (Trigonodus-Dolomit)	Ca-Mg-SO_4-(HCO_3)	2 395	21.8	< 0.1	5.605×10^{-7}	4.11	296.2	3.9 ± 0.5	glacial 12 000–14 000
Aquitard (evaporites and argillaceous rocks of the Middle and Lower Muschelkalk)										
BEN-B1	Buntsandstein	Na-HCO_3-Cl-(SO_4)	1 397	383	< 0.38	1.47×10^{-4}	0.66	300.2	3.0 ± 1.2	glacial > 26 000

[1] based on stable water isotopes and noble gas temperatures.

Summarising, the isotope and noble gas data and derived NGT of the deep ground waters are consistent with long residence times (Tables 7 and 8). No absolute values can be derived for the Malm ground water, but there are multiple lines of evidence that it contains no Holocene component and at least part of this water infiltrated during warmer climatic conditions than those of today, i.e. during Tertiary time. For the Keuper ground water, infiltration during an interglacial period in the Pleistocene is consistent with all data, which limits its residence time to more than 25 ka and less than about 2.7 Ma, the time when first direct infiltration into the Keuper could have occurred (cf. Section 2.2; Traber et al. 2002). The Muschelkalk ground water infiltrated during the last glaciation period (about 10 to 26 ka) with a ^{14}C residence time of 13 ± 1 ka. For the Buntsandstein the data consistently indicate an infiltration during a glacial period in the Pleistocene and thus a residence time in the order of several tens to hundreds of thousand of years.

The chemical and isotopic compositions observed in the Malm an Keuper aquifers are again summarised in Table 8, together with typical pore water values in the low-permeability zone between the two aquifers. These data provide the framework for the analysis of the pore and ground water data between about 400 and 710 m with a transport model (see Chapter 5).

Table 8: Summary of measured chemical and isotopic compositions in Malm and Keuper aquifers and typical values for pore water in the centre of the argillaceous, low permeability zones.
[1)] Distance between ground water sampling location and upper and lower border of the Opalinus Clay,
[2)] TDS: total dissolved solids,
[3)] relative to V-SMOW,
[4)] relative to SMOC.

Geology	**Formation**	Δ OPA **[m] [1)]**	**Water type**	TDS [2)] **[mg L^{-1}]**	Cl **[mg L^{-1}]**	$\delta^{18}O$ **[‰] [3)]**	$\delta^{2}H$ **[‰] [3)]**	$\delta^{37}Cl$ **[‰] [4)]**	**Direct infiltration earliest since**
Malm	Wohlgesch. Kalke	171	Na-Cl-SO_4	ca. 10 240	4 550	-5.46	-49.9	0.31	stagnant
Dogger	Opalinus Clay		Na-Cl-SO_4	ca. 13 900	5 670	-4.6	-40	0.37	stagnant
Keuper	Stubensandstein-Fm.	63	Na-SO4-Cl	10 161	520	-9.53	-63.2	-0.92	ca. 2.5Ma

3.6 Evaluation of cross-formation flow

The chemical, isotope and noble gas composition of the deep ground waters sampled in the Benken borehole differ significantly. Similarly, the conditions of infiltration and underground residence time are aquifer specific (Table 7). Inspection of element concentrations, ion ratios and isotope compositions along with mixing calculations reveal that none of the ground waters contain components from aquifers above and/or below. The same picture arises when looking at the chemical evolution of the ground waters. Sampled from lithologies that differ in their mineralogical composition, the ground waters are essentially in chemical and isotopic equilibrium with the rock and vein mineral assemblages from which they were sampled (cf. Section 3.3).

The distinct chemistry, isotopic composition and geochemical evolution of the four ground waters is consistent with direct infiltration into and geochemical evolution within the formation from which they were sampled, except for the Malm ground water. The latter appears to be a mixture of seawater and a meteoric component that evolved in the overlying Tertiary Molasse sediments. None of the ground waters shows any indication that there was mixing across the low-permeability rock sequences from the point of infiltration to the sampling location. Thus these low-permeability rocks, which are the argillaceous rocks between the Malm and Keuper and the Triassic evaporite sequences between the Keuper and Muschelkalk and the Muschelkalk and Buntsandstein (cf. Figure 2), effectively shield the aquifers from mixing. The absence of mixing between the ground waters, however, does of course not exclude interaction with the pore water of the low-permeability rocks.

4 Data on pore water from low-permeability units at Benken

As mentioned in the introduction, we use the term pore water to denote water from low-permeability zones and ground water to denote freely flowing water in an aquifer.

4.1 Stable water isotopes

4.1.1 Sampling and pore water analysis

No water could be sampled *in situ* from the low-permeability layers. Therefore, from depths between about 450 m and 700 m core samples with lengths of about 30 cm and diameters of about 10 cm were brought to the surface and immediately sealed in vapour-tight polyethylene-coated aluminium bags. Processing in the laboratory occurred immediately after sample reception.

The isotopic composition of pore water was determined using two different methods: the commonly used vacuum-distillation method and the newly developed diffusive-exchange method (Rübel & Sonntag 2000). For both methods the rim of the core (ca. 1 to 2 cm), which might have been contaminated by drilling fluid, was removed. For the vacuum-distillation method the central part of the core was placed into vacuum containers. The pore water was removed from the rock samples over a period of 48 h under vacuum at 105 °C and directly analysed in the mass-spectrometer. For the diffusive-exchange method, rock pieces of about 1 cm^3 were placed into a vapour-tight container together with a small amount of test water with known initial isotope composition. Diffusive exchange between the two fluid reservoirs (pore water and test water) via the vapour phase led finally to equal isotopic compositions in both reservoirs. Fractionation effects between pore water and test water are negligible for the given water contents and differences in salinity. Making two such experiments with different initial concentrations of the test water allows one to calculate both the original isotopic composition of the pore water and the water content of the rock sample from the final concentrations of the test water. For both methods, the ^{18}O and ^{2}H concentrations of the test or extracted water were determined using standard mass spectrometric procedures. All data are presented in the usual δ notation relative to the Vienna Standard Mean Ocean Water (V-SMOW). Details of both methods are given in Rübel & Sonntag (2000) and Rübel et al. (2002).

A comparison between the diffusive-exchange and the distillation method clearly revealed that the latter consistently underestimated the ^{18}O and ^{2}H concentrations in the pore fluid (Rübel & Sonntag 2000). This is explained by the incomplete removal of the pore water during distillation leading to an enrichment of heavy isotopes in the pore water remaining in the rock sample. In the following we will therefore focus on the data from diffusive exchange. Unfortunately, diffusive-exchange data between about 570 m and 650 m could not be used due to a technical problem. In this range, distillation data, shifted according to the mean deviation between the two data sets (2.9±0.33‰ in $\delta^{18}O$ and 10.7±1.9‰ in $\delta^{2}H$), are shown in order to fill the gap.

The accuracy of the mass-spectrometer measurements is ±0.1‰ for $\delta^{18}O$ and ±1.0‰ for $\delta^{2}H$. Errors of the pore-water concentrations obtained with the diffusive-exchange method were estimated to be ±0.4‰ for $\delta^{18}O$ and ±1.5‰ for $\delta^{2}H$ (Rübel & Sonntag 2000). Similar errors were attributed to the ground water samples. Somewhat larger errors of ±0.5‰ for $\delta^{18}O$ and ±2.4‰ for $\delta^{2}H$ were calculated for the shifted distillation data based on first order error propagation and assuming identical errors for the distillation as for the diffusive-exchange method.

4.1.2 Profiles of ^{18}O and ^{2}H

Figure 9 shows profiles of $\delta^{18}O$ and $\delta^{2}H$ in the pore water across the low-permeability zones at Benken, together with the values of the ground water in the bounding aquifers. The error bars indicate the uncertainties. Figure 10 displays the relations between the $\delta^{18}O$ and $\delta^{2}H$ data. The following observations can be made:

- The profiles of $\delta^{18}O$ and $\delta^{2}H$ have similar shapes. The highest values are found near the centre and upper half of the Dogger units and decrease towards the Keuper aquifer.
- The data obtained from ground water samples match well with the values of the adjacent low-permeability zones.
- The shifted distillation data fit nicely into the profiles of the data obtained from diffusive exchange.
- The isotopic composition of pore water in the Dogger units is generally heavier than that of modern meteoric waters, and presumably lighter than initial pore water, which was seawater.
- On a plot of $\delta^{2}H$ versus $\delta^{18}O$ (Figure 10), the data for the greater depths follow the Global Meteoric Water Line, whereas those above about 650 m lie to the right of it.
- The $\delta^{18}O$ value at about 545 m deviates considerably from values for neighboring samples while the $\delta^{2}H$ value differs only slightly from neighboring values.

These findings may be interpreted as follows. The heavy isotopic composition of Dogger pore waters compared with meteoric water presumably represents a remnant from old formation water. Isotopic exchange between the originally marine and younger meteoric waters most likely has occurred during the more than 144 Ma since deposition of the Jurassic sediments. Notably, erosion of the overlying Cretaceous marine sediments and karstification of the Malm limestones during early Tertiary times (about 65 to 33.7 Ma b.p.) resulted in a first dilution of the marine pore waters with fresh water (see Section 2.2 and, for burial history, Leu et al. 2001). This is also evident from the Cl contents in the pore water, which are in the order of one third of seawater (cf. Section 4.2 below). The exchange led to pore waters isotopically lighter than those originally deposited (with values probably in the range between –2 and 0 ‰ [e.g. Gregory, 1991]), but heavier than modern meteoric water. The concentration drop towards the Keuper aquifer may indicate a change of isotopic boundary conditions followed by isotopic exchange. A more detailed interpretation based on modelling results will be presented in the next sections.

The reason for the relatively low values at about 545 m is unclear. Neither hydraulic conductivities in this zone, nor structure or mineral composition of that sample, have revealed any differences to the surrounding zones. Thus, it seems unlikely that the relatively low values originate from locally altered (hydro)geologic properties, and the data are treated as outliers, originating possibly from an analytical artefact.

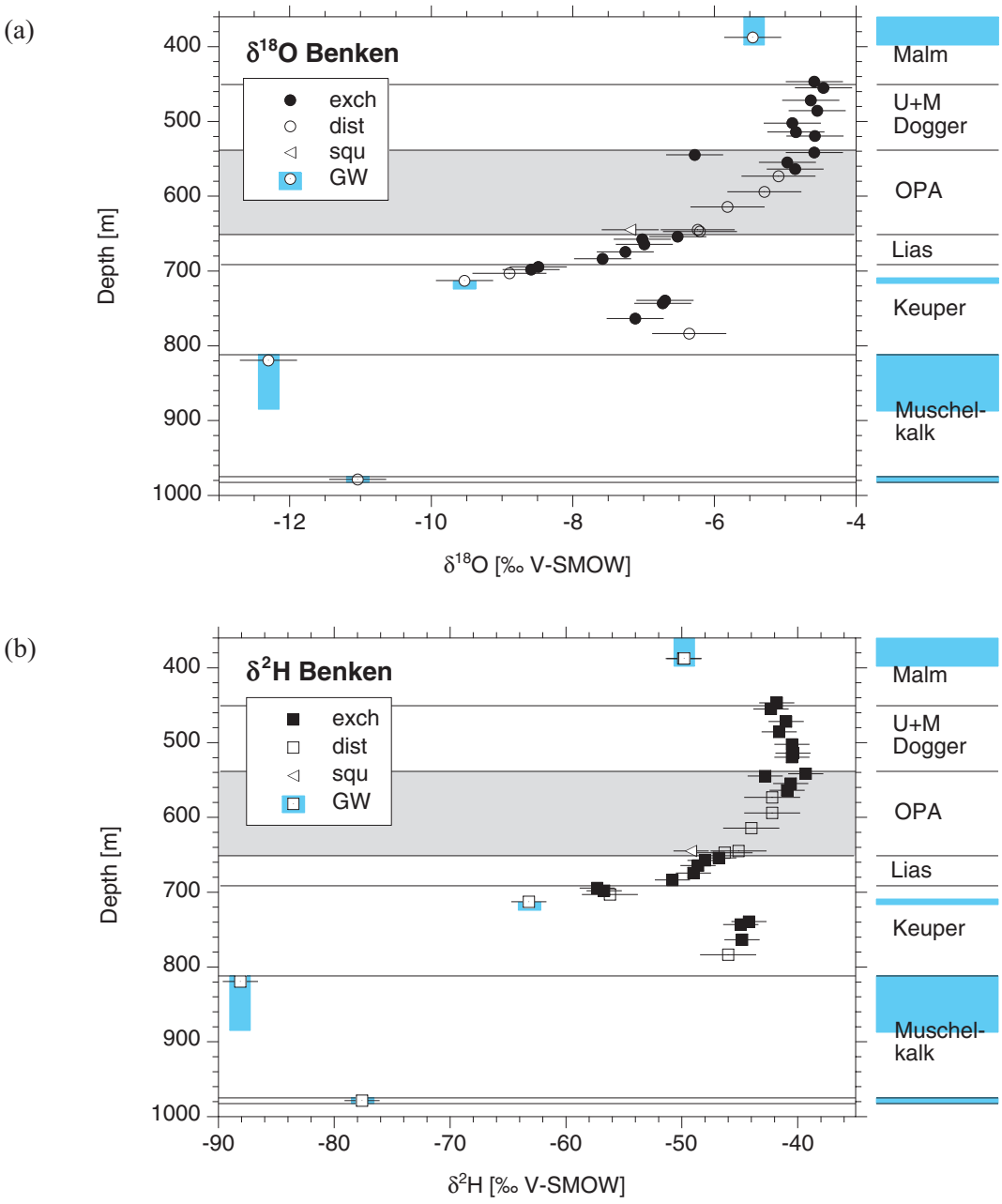

Figure 9: Profiles of $\delta^{18}O$ (a) and $\delta^{2}H$ (b) in the pore water across the Benken borehole.

Data from Rübel & Sonntag (2000) and Waber et al. (2002). Filled symbols: data obtained by diffusive exchange; open symbols: corrected distillation data; squ: squeezing data; GW: ground water samples. The error bars indicate the analytical precision. On the right side, geologic units and aquifers (turquoise) are shown. OPA denotes the Opalinus Clay including the Murchisonae Beds.

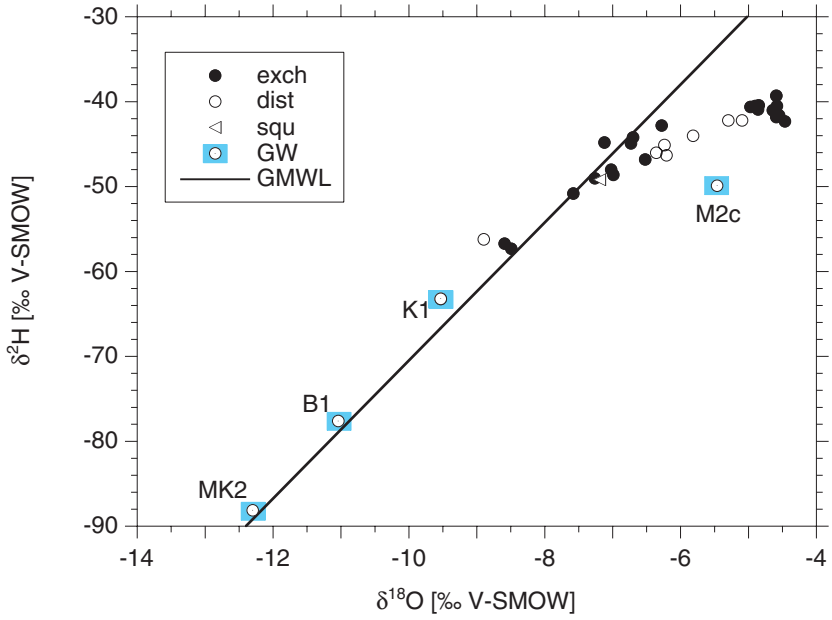

Figure 10: Relationship between the $\delta^{18}O$ and $\delta^{2}H$ contents of pore water and ground water from the Benken borehole.

Data from Rübel & Sonntag (2000) and Waber et al. (2002). Filled circles: data obtained by diffusive exchange; open circles: corrected distillation data; triangle: squeezing data; circles with dots: ground water samples; M2c: Malm; K1: Keuper; B1: Buntsandstein; MK2: Muschelkalk; GMWL: Global Meteoric Water Line, $\delta^{2}H = 10.8 + 8.13\delta^{18}O$ (e.g. Clark & Fritz 1997).

4.2 Chloride and $\delta^{37}Cl$

4.2.1 Sampling and pore water analysis

Indirect methods had to be applied to derive the chloride concentration and chlorine isotopic composition of pore water from low-permeability rocks. They were based on aqueous extraction of core samples as summarised below, and squeezing of pore water from cores under high pressures. Details of sampling and analytical procedures are given in Waber et al. (2003). The chlorine isotope composition is expressed in the common δ notation as $\delta^{37}Cl$ relative to Standard Mean Ocean Chloride (SMOC).

Aqueous extraction of rock samples yields Cl concentrations per mass of wet rock. The concentration of Cl in pore water, expressed as mass of Cl per volume of pore water, can then be calculated using an adequate porosity measure. The volume of the pore water was determined approximately by measuring the solid density of a sample and its weight loss (WL) upon drying at 105 °C.[1] If it is assumed that the leached Cl was present in all the water corresponding to the WL porosity, the minimum Cl contents of the pore water can be calculated. However, in fine-grained, clay-rich rocks, such as the Opalinus Clay, Cl cannot dissolve in all pore water because a considerable part of the water is located in the interlayer space of clays or on (negatively charged) outer surfaces of minerals. Chloride is excluded from such water mostly because of

[1] Not all pore water can be driven off upon drying at 105 °C in case of clay rocks. For the low-permeability sediments at Benken, the difference between a WL water content and the total water content (or physical porosity) is in the order of 10 to 20 % (Gimmi 2003).

electrostatic interactions, and the chloride-accessible (or chloride geochemical) porosity is smaller than the physical or also smaller than the WL porosity of the rock. The transport relevant pore-water Cl content can be calculated, if the proportion of Cl-accessible porosity to WL porosity can be estimated. An evaluation of the different porosity measures for Opalinus Clay is given in Gimmi (2003).

For the present case, the proportion of Cl-accessible porosity to total WL porosity was estimated to be 0.5 based on diffusion experiments with anions (Van Loon & Soler 2004; Gimmi 2003), squeezing experiments (Waber et al. 2003) and experience from the Mont Terri Underground Laboratory (Pearson et al. 2003). This factor and the local WL porosities were used to convert Cl concentrations per mass of rock as obtained from aqueous extraction to concentrations per volume of Cl-accessible pore water *in situ*, which are relevant for transport. The errors of the resulting Cl concentrations were estimated to be ±10 %. No such calculations are necessary for the Cl isotope ratio because no process is known that would fractionate, that is change the ratio, of Cl isotopes during aqueous extraction or lead to clearly different accessible pore fractions for two isotopes. The analytical error for δ^{37}Cl is given by the laboratory as ±0.15‰ (cf. Waber et al. 2003).

4.2.2 Profiles of Cl and ^{37}Cl

Figures 11 and 12 show the Cl and δ^{37}Cl data obtained for the pore waters of the low permeability zones and the surrounding aquifers. The following observations were made:

- The Cl concentrations are clearly diluted as compared to seawater.
- The Cl data show a general trend that is similar to that of the stable water isotopes: values are highest near the centre and upper half of the Dogger units and decrease towards the Keuper aquifer.
- The Cl data do not follow the general trend in a smooth, monotonic way. In the lower part (Lias, lower Opalinus Clay) as well as in the upper part (at the Dogger-Malm boundary) some deviations occur.
- The maxima of the δ^{37}Cl data are not found in the centre of the Dogger units, but between the upper Dogger and the Malm, and in the lower part of the Opalinus Clay. That is, ^{37}Cl is enriched towards the aquifers.

The relatively complicated patterns make the interpretation of the data difficult. Nevertheless, it seems that, in general, diffusion towards the Keuper and the Malm aquifer occurs, as in case of the stable water isotopes. This is also supported by the increased δ^{37}Cl values in regions close to the boundaries, with steep Cl gradients (cf. generic calculations in Section 6.2.1). The reason for the increased Cl values in the upper Lias is largely unknown. At least part of the scatter in the Cl data can be attributed to the uncertainty related to the Cl-accessible porosity. Similarly, analytical difficulties were encountered by the Cl isotope measurements of aqueous extract samples with high dissolved sulphate contents such as the Lias samples. Thus, the error bars may underestimate the total uncertainty of the data (Waber et al. 2003). An interpretation of the data based on the modelling results will be presented in Section 6.2.

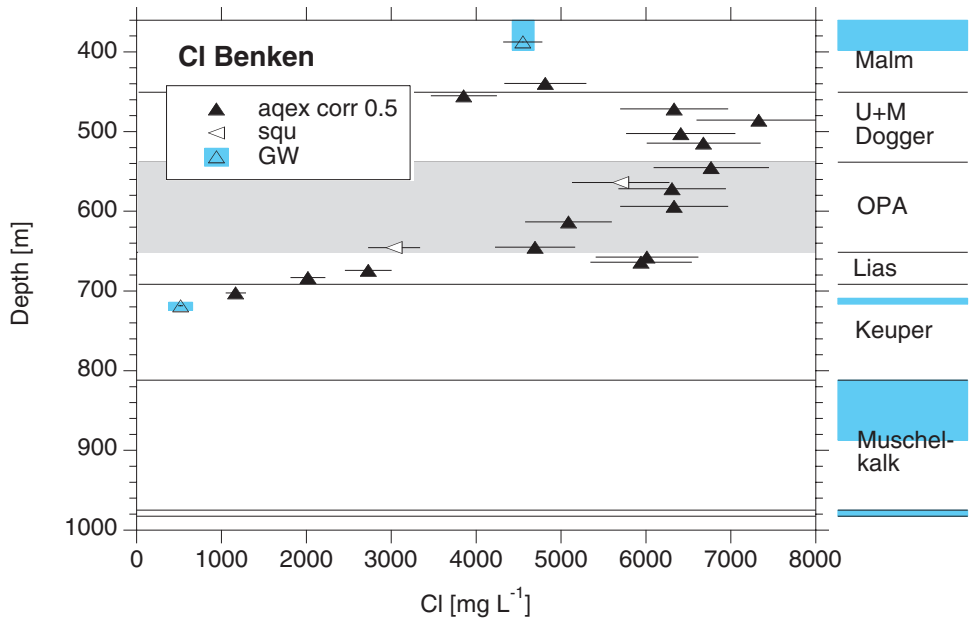

Figure 11 Profile of chloride concentrations of the pore water (mass of chloride per volume of Cl-accessible water) across the Benken borehole.

Data from Waber et al. (2002 and 2003). Filled symbols denote values obtained from aqueous extracts and scaled with a Cl-accessible porosity of 0.5; open symbols denote either values obtained from core squeezing (squ) or from ground water samples (GW). On the right side, geologic units and aquifers (turquoise) are shown. OPA denotes the Opalinus Clay including the Murchisonae Beds.

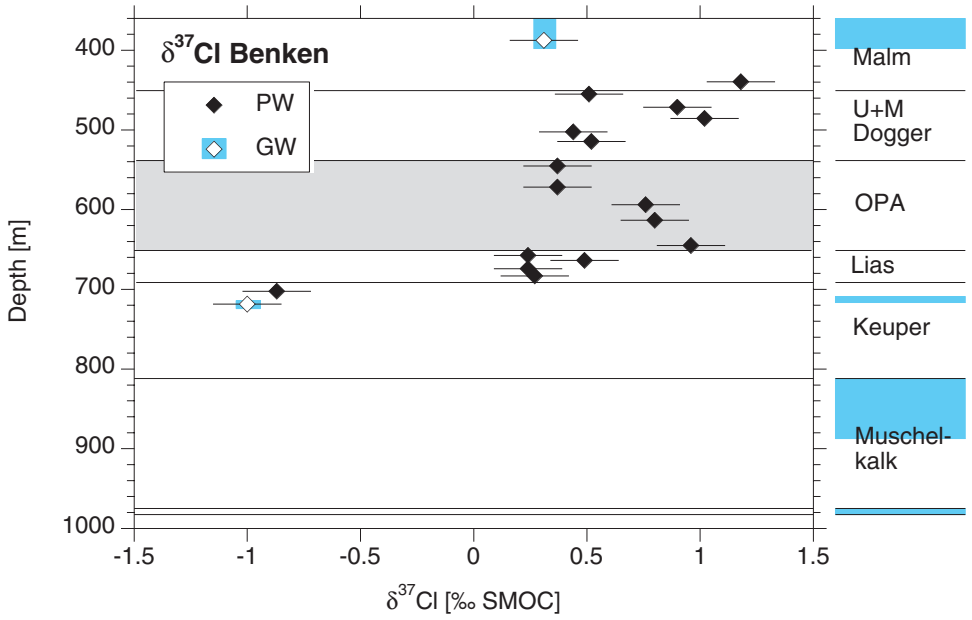

Figure 12 Profile of $\delta^{37}Cl$ in the pore water and ground water of the Benken borehole.

Data from Waber et al. (2002 and 2003). PW, filled symbols: pore water; GW, open symbols: ground water. On the right side, geologic units and aquifers (turquoise) are shown. OPA denotes the Opalinus Clay including the Murchisonae Beds.

5 Modelling approaches

5.1 General considerations

The analysis of natural tracer profiles is generally difficult, because neither the processes, nor the parameters that have led to the observations, are well known. Having several sets of data for different environmental tracers can greatly improve the analysis, provided one can link them through corresponding geologic scenarios and process models. Our modelling approach is the following. First, we will discuss geologic scenarios referring to Chapter 2, and transform them to initial and boundary conditions for the modelling. Second, we will start modelling with the stable water isotope data, which have, in our opinion, the highest information content. We will test the effect of different initial and boundary conditions on the calculated profiles, and present the corresponding conclusions. Finally, we will try to use the Cl and δ^{37}Cl data to check the conclusions obtained for the stable water isotopes, and to come up with some general conclusions.

5.2 Geologic scenarios

The qualitative interpretation of the observed profiles of δ^{18}O, δ^{2}H, Cl, and δ^{37}Cl mentioned in Chapter 4 and the palaeo-hydrogeology (Chapter 2) set the guidelines for our modelling approach. Today, the low-permeability formations are sandwiched between two aquifers, namely the Malm and the Stubensandstein Formation in the Keuper (Figure 3, Section 2.2). These aquifers define the upper and the lower boundaries of the modelled domain (Figure 13). In view of the almost undisturbed geologic stratification in the Benken area, a one-dimensional approach will suffice. Trying to model the detailed history of isotopic concentrations in pore waters since deposition is hopeless because of the very long time scales involved and the uncertainties in geologic history. Instead, we will concentrate on the most dominant feature of the data, which is the decrease of δ values or concentrations towards the Keuper.

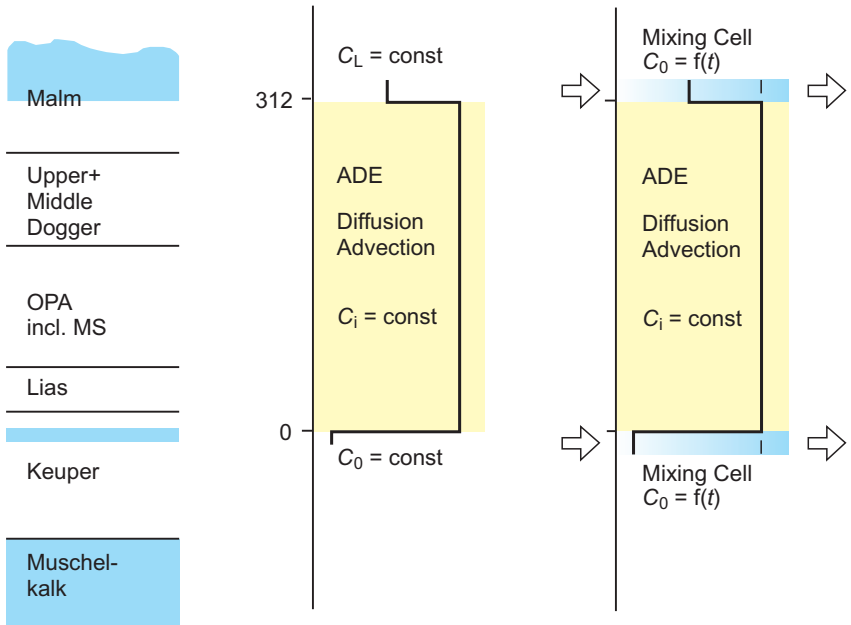

Figure 13: Schematic representation of the model setup chosen and the corresponding boundary and initial conditions.

The basic hypothesis is that the shape of the profile originates from a relatively late change in the Keuper boundary condition. Diffusive and possibly also advective transport has then propagated the perturbation of isotopic concentrations at the lower boundary into the Dogger units. Geologic reasoning for this scenario and for implied boundary and initial conditions can be found in Chapter 2 and will be summarised again in the following paragraphs.

5.2.1 Initial conditions

The isotopic and chemical composition of the pore waters in the Jurassic sediments is interpreted as a remnant of old formation water that evolved from the original seawater by interaction with the rock and the surrounding aquifer waters in the course of the geologic evolution. Jurassic and Cretaceous sediments were deposited about 206 to 65 Ma ago mainly under marine conditions. After erosion of Cretaceous as well as upper Malm layers, the lower Malm was exposed to fresh water for at least 30 million years (about 65 to 33.7 Ma b.p., see Chapter 2). About 30 to 10 Ma ago, the Jurassic sediments were covered again by the Molasse sediments, which comprise a sequence of alternating fresh and marine water sediments.

The changing upper boundary conditions, and the long time spans involved, most likely have resulted in rather smooth, low-gradient concentration profiles across the Jurassic sediments. This means that the isotopic concentrations across most of the Dogger units were approximately constant, but at an unknown value, before the relatively late event generated the shapes observed today (cf. also Figure 13). As a starting point, the maximum values observed today in the upper Dogger units were used (cf. Table 9). Alternatively, larger initial concentrations were considered, representing pore waters less diluted by fresh water.

5.2.2 Keuper boundary condition

In the Benken borehole the water-conducting zone of the Keuper is the Stubensandstein Formation. This formation, which is about 11 m thick, includes dolomite-breccias at the top with a hydraulic conductivity of about 10^{-7} m s^{-1} (Nagra 2001). The porous dolomite-breccias are the result of the dissolution of evaporitic layers during diagenesis. Thus, the permeability of this layer was much lower than it is at present for a very long period of time.

High permeability alone does not necessarily imply water flow. The aquifer must also be connected to infiltration and exfiltration zones. As stated in Section 2.2, direct infiltration into the Keuper lithologies occurs at present in the Wutach region in the foothills of the Black Forest to the north of Benken (Traber et al. 2002). New exfiltration zones for the Keuper aquifer, that are still active today, were created by deep erosion in the Klettgau area some 1.8 to 2.0 Ma ago following the diversion of the Alpenrhein towards the Aare river about 2.7 Ma ago (Section 2.2; Villinger 2003).

It thus appears that the Keuper units contained old formation water and had similar hydraulic properties as the overlying Dogger units for most of the time since deposition. Significant flushing with meteoric water may have started less than about 2 Ma ago with the creation of new exfiltration areas. This flushing with meteoric water led then to the observed drop in the concentration of stable water isotopes.

This scenario is also supported by the Keuper water sampled (Chapter 3; Waber et al. 2002). Chemical and isotopic composition of this water consistently indicate an evolution in the formation from which it was sampled (i.e. Stubensandstein) and an infiltration under climatic conditions like those of the present. The absence of measurable tritium excludes the presence of

a young ground water component, and the undetectable ^{14}C, the high He content, and the high $^{40}Ar/^{36}Ar$ ratio of this water indicate that recharge occurred well before the present climatic period, most probably during early Pleistocene times. Although no absolute age can be derived for the Keuper water, the regional geologic history and the formation water chemistry limit its residence time in the subsurface to an interval between 2.6 Ma (climate) and substantially more than 25 000 years (high He concentrations, absence of ^{14}C).

A rough estimate of the residence time may also be obtained from estimates of distance to the infiltration area, hydraulic gradient and conductivity, and porosity of the aquifer. Using a distance of 20 to 30 km, the present-day gradient of about –0.003 to –0.007 m m^{-1}, a conductivity of 10^{-8} to 10^{-7} m s^{-1}, a porosity of 0.015 to 0.15 and assuming correlation between conductivity and porosity, residence times in the order of 0.15 to 0.5 Ma were estimated. These times are within the range indicated by the chemical composition.

Combined with geologic evidence it can be concluded that the evolution time of the profiles in the low-permeability zones, that is the time since the concentration dropped in the Keuper aquifer in Benken, must be lower than about 1.8–2.7 Ma when direct infiltration and regional discharge to the present Rhine were established. The stable isotope signature of the Keuper aquifer in Benken may have varied somewhat with time since then, with slightly lower values resulting from infiltration during the glacial periods. Also, Cl concentrations can be expected to have been higher in the very initial stages of ground water circulation because of the known presence of halite in the Keuper lithologies at other locations, but might have rapidly dropped to values like those observed today or even below these.

As base case boundary conditions for the Keuper, the measured concentrations in the ground water were chosen to have prevailed since the flushing of the aquifer (Table 9). Several alternatives were tested, including a lower flushing rate because the hydraulic conductivity observed today first had to be developed by mineral dissolution reactions, and somewhat lower stable isotope ratios accounting for a glacial input.

5.2.3 Malm boundary condition

The facts that the whole sequence of Cretaceous sediments is eroded in the area and that the Malm limestones are strongly karstified suggest that the original marine formation water was flushed before Tertiary times. During the Tertiary, the area was subjected to alternating fresh water and brackish to seawater environments under subtropical to tropical conditions and the Malm could possibly have been saturated alternately with seawater and fresh water. As outlined in Chapter 3, an explanation of the Malm ground water that is consistent with the measured data is that it is a mixture of a Tertiary seawater component with meteoric water. The age of this meteoric component is difficult to define. Radiogenic and stable isotopes and noble gases suggest, however, that infiltration of this meteoric component must have occurred at least during an interglacial period in the Pleistocene if not during late Tertiary times. At present, the entire sequence of Malm limestones at Benken is characterised by a low hydraulic conductivity (8.8×10^{-9} m s^{-1}, Nagra 2002, Chapter 3.6) and almost stagnant ground water flow conditions can be assumed over this entire time range.

Unfortunately, no pore-water data are available from the lowest Malm units that could characterise the link between the pore-water profiles and the value obtained for the Malm ground water. Because of this and the complex palaeo-hydrogeologic evolution of the Malm ground water it is difficult to define unique boundary conditions for the Malm. Therefore, we will test the effect of different boundary conditions on the evolution of water isotopes in the underlying formations. Conditions that may have prevailed for at least several hundreds of

thousand to a few millions of years are assumed for the base case simulations, as listed in Table 9. To take into account an initially more dilute mixture of meteoric water and seawater, a lower Cl concentration in the Malm was also assumed.

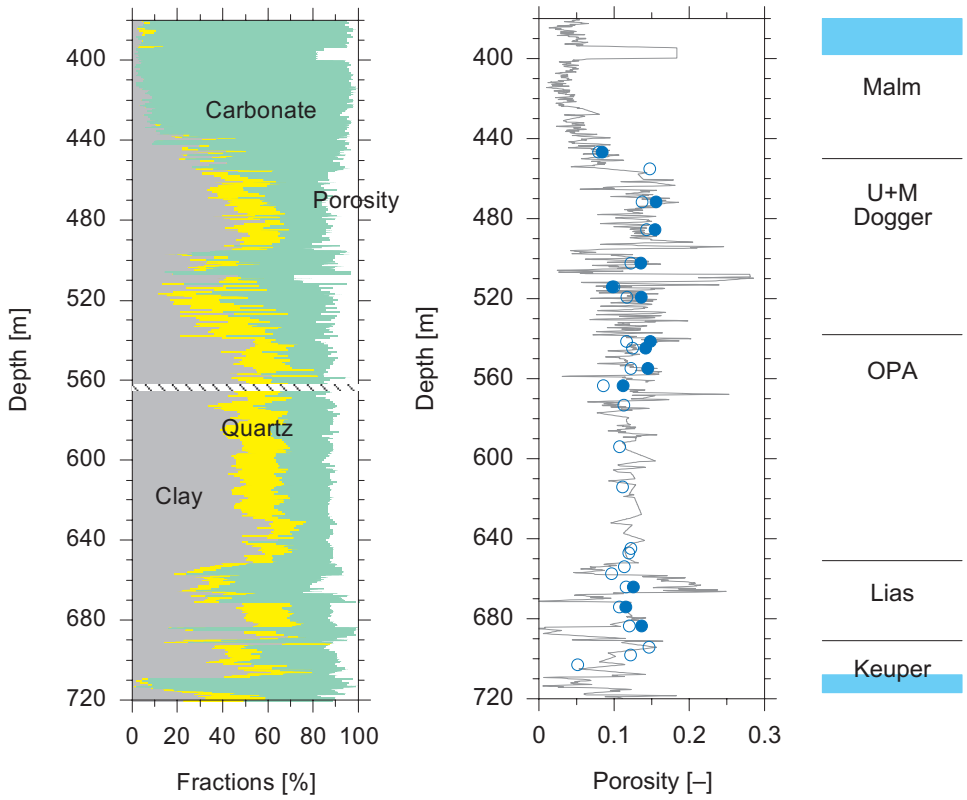

Figure 14: Mineralogy and porosity of the Benken borehole calculated from geophysical borehole logs, and porosities for the samples from which the stable isotope values were obtained.

The data based on geophysical borehole logs (left side and the solid line on the right side) are from Nagra (2001). The porosities estimated by drying at 105 °C (open circles) or by diffusive exchange (filled circles) are from Rübel & Sonntag (2000).

5.2.4 Spatial and temporal variability of parameters

Structural and mineralogical investigations of rock samples across the Dogger units have revealed a relatively small spatial variability (Nagra 2001; Mazurek 2001; Gimmi 2003). Only in a few locations with a small vertical extent (lenses) were there clear differences in porosity or mineralogy (with the exception of the lower Malm), as can be seen for instance from the mineralogy or porosity calculated based on several calibrated geophysical borehole logs (Nagra 2001) or from the porosity values of the samples used to derive the stable water isotope values (Figure 14). In view of the relatively small variability it seems justified to assume – in a first attempt – spatially constant transport parameters throughout the entire domain. To test the influence of variable porosity and diffusion coefficients, some calculations were also run with a numerical (finite difference) code developed by us.

Properties of the domain will certainly have changed with time since deposition. Strong compaction of the clayey sediments occurred during two subsequent burial events during the Cretaceous and Tertiary (Leu et al. 2001). This compaction can be considered as nearly

irreversible, in that probably no dramatic changes of the rock fabric took place during the last 10 Ma or so, where the whole area was generally lifted up. There is no evidence either that the relatively late contact with fresh Keuper water altered the structure of the sediments significantly, because porosity, for instance, shows only a slight trend with depth. Thus, we will also assume temporally constant parameters.

5.3 Mathematical representation

5.3.1 Transport equation

Following the arguments presented in Section 5.2, transport calculations were based on the one-dimensional advective-dispersive equation with constant coefficients

$$\frac{\partial C}{\partial t} = D_p \frac{\partial^2 C}{\partial z^2} - v \frac{\partial C}{\partial z} \qquad [1]$$

where C is the concentration of an isotope or chemical in the water phase, D_p is the (pore) dispersion coefficient, v the average linear pore velocity, t the time, and z the depth coordinate (positive upward with $z = 0$ at 709.1 m below ground, $z = L$ at 397.0 m below ground, and $L = 312.1$ m; cf. Figure 13). Note that the porosity or water content ε was assumed to be constant throughout the formations and therefore could be eliminated. For very low advective velocities, as expected in such clay layers, dispersion is dominated by diffusion, and D_p is just the pore diffusion coefficient. In argillaceous media, different solutes may access different parts of the pore space. Thus, D_p and v may, in principle, be solute specific.

The δ values used in case of isotopes are scaled and shifted ratios of two isotope concentrations and thus depend on both of them:

$$\delta = \frac{R}{R_{std}} - 1 = \frac{{}^bC}{{}^aC}\left(\frac{{}^aC}{{}^bC}\right)_{std} - 1, \qquad [2]$$

with $R = {}^bC/{}^aC$, and ${}^aC$ and ${}^bC$ are the concentrations of the main or reference (a) and of the less abundant (b) isotope. If the main isotope concentration ${}^aC$ remains essentially constant in time and space, the δ values just represent linearly scaled and shifted concentrations of the isotope b and can be treated as any ordinary chemical concentration. This is typically the case for water isotopes, because the total water concentration can be considered as constant for normal pressures and temperatures. Then, the gradients and changes of ^{16}O and ^{1}H concentrations are negligible compared to the relevant gradients and changes of the δ values, and Eq. [1] can be used to model the $\delta^{18}O$ and $\delta^{2}H$ values. For Cl, the situation is different. Cl concentrations can significantly vary with depth and time. Accordingly, Eq. [1] cannot be applied to $\delta^{37}Cl$ values, but individual calculations with different D_p values have to be performed for ^{35}Cl and ^{37}Cl.

Based on the low osmotic efficiency reported for Opalinus Clay (Nagra 2002, Chapter 5.11), we did not consider any osmotic phenomena in the transport equations for Cl. By using Eq. [1] to describe $\delta^{37}Cl$ profiles, we also neglected fractionation processes for ^{37}Cl other than diffusion. This seems justified for the processes occurring relatively late in the geologic history, but it

might be incorrect for the earlier times, where compaction was important, e.g. during burial of the formations, or generally for media with higher osmotic efficiency (cf. de Marsily et al. 2002; Gonçalves et al. 2004).

5.3.2 Initial and boundary conditions for water isotopes

Initially, uniform isotope concentrations throughout the modelled domain ($0 \le z \le L$) were assumed. As first estimates, we used initial values of $\delta^{18}O = -4.6‰$ and $\delta^{2}H = -40‰$ according to maximum values observed today in the upper Dogger units (cf. Table 9). Alternatively, larger initial concentrations of $\delta^{18}O = -3.2‰$ and $\delta^{2}H = -30$ or $-37‰$ were tested, representing pore waters less diluted by fresh water. Note that the larger initial value for $\delta^{18}O$ was chosen more or less arbitrarily. The values for $\delta^{2}H$ were then chosen either so that a similar fit as for $\delta^{18}O$ was obtained at similar times, or according to the trend of the relation between $\delta^{18}O$ and $\delta^{2}H$ in the upper part of the profile.

The concentration drop at the lower boundary at $t = 0$ was modelled in two different ways. The first was simply to assume constant concentrations C_0 at $z = 0$ for $t > 0$, equal to the values measured today in the Keuper aquifer ($\delta^{18}O = -9.53‰$ and $\delta^{2}H = -63.2‰$, cf. Table 9). The second takes into account a gradual decrease from initial values in the Keuper aquifer, equal to the initial values in the pore water, to those observed today, as may have happened during the onset of flow. The gradual decrease was achieved by representing the aquifer as a mixing cell of equivalent height ζ, which was flushed for $t > 0$ at a given rate ρ with water of a given concentration C_{in}. The concentration drop in this mixing cell, in which concentrations are always uniform, results from the interplay of advective and diffusive mass transfer across the boundary to the low-permeability zone, and advective input and output of flushing water. The equation for the lower boundary is in this case

$$\varepsilon_m V \frac{\partial C_m}{\partial t} = \varepsilon_m A v_{in} C_{in} - \varepsilon_m A v_{out} C_m - \varepsilon B \left(v C\big|_{z=0} - D_p \left.\frac{\partial C}{\partial z}\right|_{z=0} \right) \qquad [3]$$

where C_m is the concentration within the mixing cell (aquifer), V the volume, A the vertical, and B the horizontal cross sectional area of the mixing cell over which solute exchange happens, ε_m the porosity of the aquifer, C_{in} the concentration of the flushing water, v_{in} the flushing velocity, and v_{out} the velocity of the water leaving the mixing cell. Taking into account the mass balance for water and neglecting density changes, v_{out} is related to v and v_{in} as $v_{out} = v_{in} - v\,(\varepsilon B) / (\varepsilon_m A)$ (for z positive upward). Using this relation and introducing the flushing rate

$$\rho := v_{in} A / V \qquad [4]$$

and the equivalent height of the aquifer or mixing cell

$$\zeta := \varepsilon_m V / (\varepsilon B) \qquad [5]$$

the equation for the mixing cell can be simplified to

$$\frac{\partial C_m}{\partial t} = \rho\left(C_{in} - C_m\right) + \frac{D_p}{\zeta}\frac{\partial C}{\partial z}\bigg|_{z=0} \qquad [6]$$

To obtain this last equation, we assumed also continuity of concentrations across the lower boundary, i.e. $C_m = C(z = 0,t)$. This assumption together with the use of a dispersive and an advective term for mass transfer between aquifer and low-permeability layers in Eq. [3] corresponds to a resident injection, as defined in Gimmi & Flühler (1998). This type of solute exchange is typical for a reservoir in close contact with an advective-dispersive transport domain and for low advective velocities. We assumed meteoric concentrations of the flushing water C_{in} of $\delta^{18}O = -9.53‰$ and $\delta^{2}H = -63.2‰$ or slightly lower values (cf. Section 6.1.4) and investigated various flushing rates ρ.

For the Malm interface at $z = L$, the following boundary conditions were compared: Constant concentrations C_L according to measured values of the Malm aquifer (–5.46‰ and –49.8‰, cf. Table 9), zero concentration gradients, or a mixing cell boundary condition analogous to that at the lower interface.

Table 9: Initial (IC) and boundary conditions (BC) for the base case simulations with constant concentrations at the Keuper and Malm interfaces. The values for the various alternative initial and boundary conditions are given in the text.

	IC	**Keuper BC**	**Malm BC**
$\delta^{18}O$	–4.6 ‰	–9.53 ‰	–5.46 ‰
$\delta^{2}H$	–40 ‰	–63.2 ‰	–49.8 ‰
Cl	6 600 mg L^{-1}	520 mg L^{-1}	4 550 mg L^{-1}
$\delta^{37}Cl$	0.31 ‰	–1.0 ‰	0.31 ‰

5.3.3 Initial and boundary conditions for chloride and $\delta^{37}Cl$

The types of initial and boundary conditions used for Cl and the Cl isotopes are the same as those presented in 5.3.2. For Cl, an initial concentration $C_i = 6\,600$ mg L^{-1} was used for the base case simulations (Table 9) according to the observed values in the upper and middle Dogger, and a value of 9 000 mg L^{-1} for the test of a larger initial concentration. The values for the constant concentration C_0 at the Keuper interface or the concentration of the flushing water entering the mixing cell, C_{in}, were 520 mg L^{-1}, the value C_L at the Malm interface 4 550 mg L^{-1}, all according to the measured ground water values. For $\delta^{37}Cl$, for the base case an initial value of 0.31 was used (approximately equal to measured values in the middle part), and boundary values of -1‰ (Keuper) and 0.31‰ (Malm) as observed today in the aquifers (Table 9).

5.3.4 Solutions

Analytical solutions of Eq. [1] exist for instance for constant concentrations on both sides of the domain, or constant concentration on one side and zero gradient on the other (e.g., Carslaw & Jaeger 1959; van Genuchten & Alves 1982). To be more flexible with respect to boundary conditions, we obtained solutions generally in Laplace space and inverted them back numerically with the Talbot algorithm (Jury & Roth 1990). The Laplace space solution for constant concentrations $C(0,t) = C_0$ and $C(L,t) = C_L$ is

$$\hat{C}(z;s) = \frac{(C_L - C_i)e^{a(z-L)}\sinh(abz) - (C_0 - C_i)e^{az}\sinh[ab(z-L)]}{s\sinh(abL)} + \frac{C_i}{s} \qquad [7]$$

where C_i is the initial concentration, $a := v/2/D_p$, $b := (1+4sD_p/v^2)^{1/2}$, ^ denotes a Laplace transformed variable, and s is conjugate to time t.

The solution for a constant concentration $C(0,t) = C_0$ and a zero gradient at $z = L$ is

$$\hat{C}(z;s) = \frac{(C_0 - C_i)}{s} e^{az} \frac{b\cosh[ab(z-L)] - \sinh[ab(z-L)]}{b\cosh(abL) + \sinh(abL)} + \frac{C_i}{s} \qquad [8]$$

For a mixing cell at $z = 0$ with $C(0,t) = C_m(t)$, and a constant concentration $C(L,t) = C_L$, a zero gradient, or another mixing cell with $C(L,t) = C_{mL}(t)$ at $z = L$, the general Laplace space solution is

$$\hat{C}(z;s) = A_1 e^{az(1+b)} + A_2 e^{az(1-b)} + \frac{C_i}{s} \ . \qquad [9]$$

For a constant concentration $C(L,t) = C_L$ at $z = L$ and the mixing cell at $z = 0$, the above coefficients are

$$A_1 = \frac{T_2(C_L - C_i)e^{-aL(1-b)} - T_3}{s(T_2 e^{2abL} - T_1)}, \qquad A_2 = \frac{T_3 - T_1(C_L - C_i)e^{-aL(1+b)}}{s(T_2 - T_1 e^{-2abL})} \qquad [10]$$

with

$$T_1 = \rho + s - \frac{v(1+b)}{2\zeta}, \qquad T_2 = \rho + s - \frac{v(1-b)}{2\zeta}, \qquad T_3 = \rho C_0 + s C_{mi} - (\rho + s)C_i,$$

where ρ is the flushing rate defined in Eq. [4], and ζ the equivalent height or thickness of the mixing cell as defined in Eq. [5].

For a zero gradient at $z = L$ and the mixing cell at $z = 0$, the coefficients are

$$A_1 = \frac{T_3(1-b)}{s(T_1[1-b] - T_2[1+b]e^{2abL})}, \qquad A_2 = \frac{T_3(1+b)}{s(T_2[1+b] - T_1[1-b]e^{-2abL})} \qquad [11]$$

with T_1, T_2, and T_3 as above.

And finally, for mixing cells at both ends, the following coefficients can be found:

$$A_1 = \frac{T_3 T_{2L} e^{aL(1-b)} - T_2 T_{3L}}{s\left(T_1 T_{2L} e^{aL(1-b)} - T_2 T_{1L} e^{aL(1+b)}\right)}, \qquad A_2 = \frac{T_1 T_{3L} - T_3 T_{1L} e^{aL(1+b)}}{s\left(T_1 T_{2L} e^{aL(1-b)} - T_2 T_{1L} e^{aL(1+b)}\right)} \qquad [12]$$

with T_1, T_2, and T_3 as above, and

$$T_{1L} = \rho_L + s + \frac{v(1+b)}{2\zeta_L}, \quad T_{2L} = \rho_L + s + \frac{v(1-b)}{2\zeta_L}, \quad T_{3L} = \rho_L C_0 + s C_{miL} - \left(\rho_L + s\right) C_i,$$

where ρ_L, ζ_L, and C_{miL} are the flushing rate, the equivalent height or thickness, and the initial concentration of the mixing cell at $z = L$, respectively. Switching boundary conditions between $z = 0$ and $z = L$ is possible, if required, by switching the direction of the z-axis. For velocities $v \to 0$ or, correspondingly, $Pe = vL / D_p << 1$ (see next paragraph), the above solutions tend to the solutions for pure diffusion.

We mention just in passing that solutions were also developed for a non-constant linear initial concentration distribution $C(x,0) = ax + b$, and for stepwise ($t_i < t < t_{i+1}$) constant concentrations at the boundaries.

5.4 Parameter estimation

The dispersion coefficient D_p and the advective flow velocity v were initially treated as unknown, although we have some information about small-scale diffusion coefficients of Opalinus Clay samples and present-day hydraulic properties in the Benken area. We do not know precisely, when the concentration drop in the Keuper aquifer occurred. Thus, the evolution time t was also considered as an unknown. It is then convenient to replace the time t in the transport equation with a dimensionless diffusion time $T_D = D_p t/L^2$, where L is the size of the domain, or, since L is known, with a diffusion distance $\xi = (D_p t)^{1/2}$. Consequently, for $v = 0$ the transport equation has no free parameter, and the concentrations C are a function of the dimensionless variables T_D and z/L, or of the lengths ξ and z only. If v is different from zero, the transport equation depends on a single parameter, namely the Peclet number $Pe = v\,L/D_p$ in case of T_D, or the dispersivity D_p/v in case of ξ. If a mixing-cell boundary condition is used, Eq. [6] should also be transformed such that instead of the flushing rate ρ a scaled parameter $\rho L^2/D_p$ or ρ/D_p, respectively, appears.

In the following, we will express concentrations as a function of the diffusion distance ξ. We will try to estimate ξ and D_p/v from the ^{18}O and ^{2}H data sets. For that purpose, the weighted sum of squares of the deviations between measured and calculated data, the χ^2 function, is minimised (ignoring the values at 545 m). As a criterion to assess the relative quality of the fit of a simulation, we used the calculated χ^2 divided by the number of data points n

$$\Delta := \frac{\chi^2}{n} = \frac{1}{n} \sum_{i=1}^{n} \frac{\left(y_i - y_{mi}\right)^2}{\sigma^2} \qquad [13]$$

where y_i are measured and y_{mi} calculated values, and σ_i is the standard deviation of the pore water measurements. The quantity Δ gives the average squared deviation between the measurements and the simulations, scaled by the variance.

Since oxygen and hydrogen in water generally move together as a water molecule, it makes sense to combine the two data sets for parameter estimation. In this case, equal weights were attributed to each set. We also estimated parameters for each data set individually. Once a value of ξ was obtained, we could use laboratory-scale diffusion coefficients of Opalinus Clay to estimate the time that has passed since the concentration in the Keuper aquifer dropped, or, the other way round, obtain diffusion coefficients, provided evolution times were known a priori.

6 Modelling results and discussion

6.1 Stable water isotopes

6.1.1 Base case

As a base case, we considered purely diffusive transport with constant concentrations for $t > 0$ according to present-day values at the Keuper and Malm boundaries (cf. Table 9). The initial values were derived from maximum concentrations in the upper part of the domain. Figure 15 shows best-fit curves for the combined ^{18}O and ^{2}H data sets for the base case as well as for zero gradient upper boundary conditions. Minimum deviations between data and simulations were found in both cases for ξ = 39.7 m. Note that the data at about 545 m were ignored for the estimation of ξ (cf. Section 4.1.2).

In general, the simulations for the base case with purely diffusive exchange match the data quite well. This confirms the importance of diffusion. It indicates also that the chosen setup with constant parameters, homogeneous initial conditions, and constant boundary concentrations is a possible scenario. Of course, some of the deviations between the data and the simulations may be linked to simplifications of the set-up. For instance, the $\delta^{2}H$ values in the Lias, and to a lesser degree also the $\delta^{18}O$ values, have a gradient smaller than simulated around 660 m, and larger than simulated at depths between about 680 and 710 m. This may point to larger than average porosity or D_p in the upper part of the Lias, and smaller than average in the lower part. Indeed, a somewhat larger porosity was estimated from the bulk densities obtained in the borehole log in the upper Lias (but not confirmed by the porosity values of the corresponding samples), as can be seen in Figure 14. The porosities obtained in the borehole log may suffer from local borehole collapse. Nevertheless, we ran simulations with a numerical code, taking into account the spatial heterogeneity of the porosity according to Figure 14, while assuming constant D_p. The simulations (not shown) revealed that this variability has only a minor influence on the simulations and the estimated ξ values, but locally may improve the correspondence between measurements and simulations.

Van Loon & Soler (2004) have obtained an effective diffusion coefficient of $D_e = 6.1 \times 10^{-12} \pm 0.6 \times 10^{-12}$ m^2 s^{-1} from laboratory experiments at room temperature (about 22± 2 °C) on small Opalinus Clay samples from Benken, where tritium diffused perpendicular to the bedding. Based on a water-filled porosity ε of 0.12 ± 0.02 m^3 m^{-3}, a pore diffusion coefficient of about $5.0 \times 10^{-11} \pm 1.0 \times 10^{-11}$ m^2 s^{-1} at 22 °C can be deduced. At Benken, the in-situ temperature in the Opalinus Clay is and has probably been for the last several millions of years about 35 to 40 °C (Nagra 2001), with somewhat lower temperatures in the upper part of the low-permeability zones. The laboratory diffusion coefficient D_p at this temperature is about $1.0 \times 10^{-10} \pm 0.2 \times 10^{-10}$ m^2 s^{-1} (Van Loon & Soler 2004), i.e. about twice that at room temperature. With that value, an evolution time of about 0.5 ± 0.1 Ma was estimated for ξ = 39.7 m, where the error covers only the uncertainty of the laboratory diffusion coefficient D_p. Temperatures and thus also diffusion coefficients are somewhat lower in the upper part of the low-permeability zones. This has only a small effect on the simulations, as was tested with the numerical code, and thus the time of 0.5 Ma can be considered as a minimum time. The evolution time seems plausible when compared with the maximum time frame of about 1.5 - 2 Ma that was set by geologic and geochemical evidence. Conversely, the agreement between estimated evolution time and geologic evidence indicates that – to the order of magnitude – laboratory diffusion coefficients can be considered as relevant on these much larger temporal and spatial scales.

In the following, we will commonly indicate evolution times instead of values for ξ. All evolution times for stable water isotopes were calculated from ξ estimates with the above-mentioned diffusion coefficient $D_p = 1.0 \times 10^{-10}$ m^2 s^{-1}. Of course, a different D_p value would, for the same ξ, lead to different evolution times, according to the relation $t = \xi^2/D_p$. A different D_p value requires, in addition, a scaling of the flushing rate – for calculations involving a mixing cell – according to the relation $\rho_1/D_{p1} = \rho_2/D_{p2}$, and a scaling of the velocity – in case of advective flow – according to $v_1/D_{p1} = v_2/D_{p2}$. Thus, if a lower diffusion coefficient of $D_p = 5.0 \times 10^{-11}$ m^2 s^{-1} is used, evolution times have to be doubled to get the same calculated values, if at the same time the flushing rate and the advective velocity are reduced by a factor of two.

A closer look at Figure 15 reveals that a single calculation may not fit both data sets equally well. Indeed, from individual data sets we estimated a diffusion distance $\xi = 47.0$ m for $\delta^{18}O$ and $\xi = 35.5$ m for δ^2H (Figure 16). The differences in the calculated curves are relatively small compared to the scatter of the data, but they would translate to a ratio of about 1.75 for the evolution times t (smaller time for ^2H) or for the pore diffusion coefficients D_p (smaller diffusion coefficient for ^2H), respectively. Different evolution times t due to non-simultaneous change of boundary conditions for ^{18}O and ^2H are unreasonable. Different diffusion coefficients D_p of ^2H and ^{18}O are, in principle, possible and could have various origins. A retarded diffusion of ^2H as compared to ^{18}O may result from slightly stronger enrichment of ^2H in interlayer or other strongly bound water, but such differences are expected to affect the ratio of diffusion coefficients only at the second or third decimal. Relative mass differences for ^{18}O in water as compared to ^2H in water may also lead to different diffusion coefficients. According to Graham's law applied for average species, this ratio is about 0.975, which means that ^{18}O would be retarded as compared to ^2H. Thus the relative mass differences cannot explain the findings. Interaction of ^{18}O of the pore water with oxygen of solids could be regarded as another possibility. Such interaction would include dissolution/precipitation reactions, as for instance calcite dissolution, and isotopic exchange between pore water and minerals. The pore water is in chemical equilibrium with and buffered by the surrounding rock (Pearson 2002, Waber et al. 2003). Only minimal mass transfer induced by dissolution/precipitation reactions is required to preserve equilibrium along the chemical gradients towards the aquifers. Such small mass transfer could not account for observable changes in the pore water ^{18}O or ^2H concentrations. Isotopic exchange can also be excluded because such reactions are extremely slow (in the order of tens of Ma) at the *in situ* temperatures present in the formation since the last burial. More important, both processes, reactions and isotopic exchange, would slow down the diffusion of ^{18}O as compared to ^2H, in contrast to what is observed.

Based on these considerations, we believe that the different ξ values for ^{18}O and ^2H mainly reflect uncertainties of the data and of the modelling approach. The factor 1.75 may just give an estimate of uncertainty for calculated evolution times. Figure 17 displays calculations for evolution times of 0.25, 0.5, and 1 Ma indicating the sensitivity of the calculations to doubling the evolution time or dividing it by a factor two.

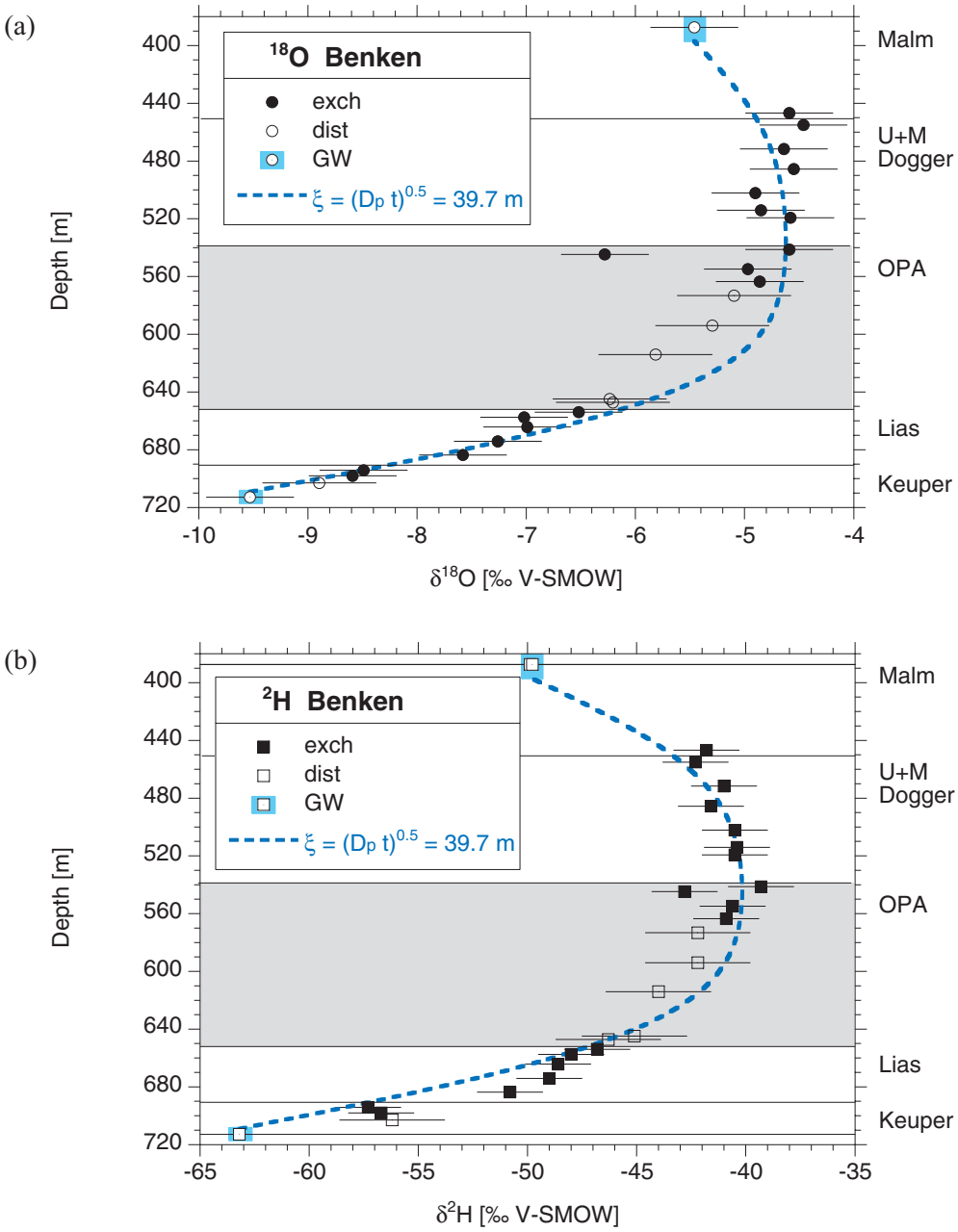

Figure 15: Best-fit simulations for the combined data sets of $\delta^{18}O$ (a) and $\delta^{2}H$ (b) for the base case (pure diffusion, constant concentrations at Keuper and Malm boundary, initial concentrations derived from maximum concentrations found in pore water).

Symbols as in Figure 9. Cf. Table 9 for initial and boundary conditions.

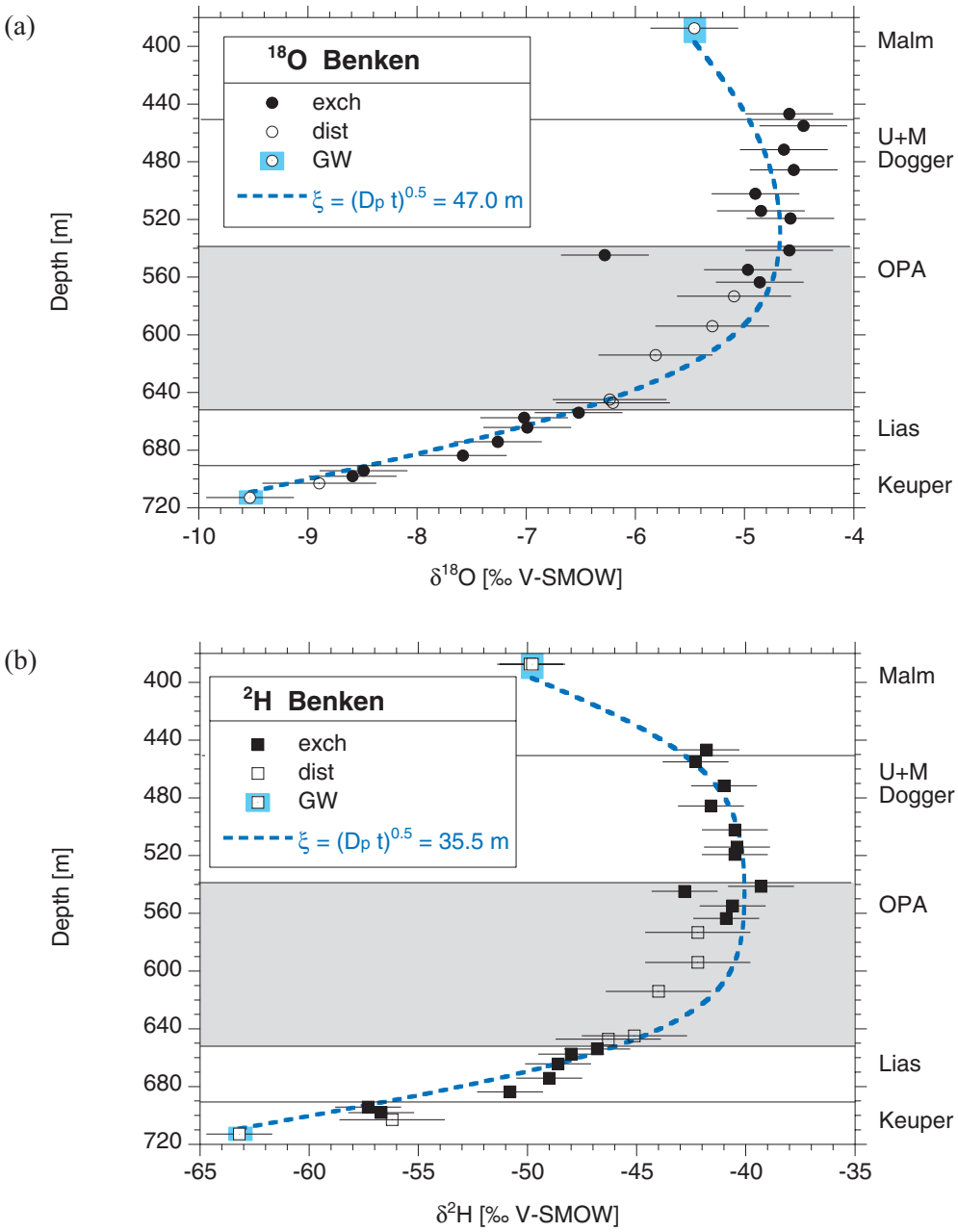

Figure 16: Individual best-fit simulations for the data sets of $\delta^{18}O$ (a) and $\delta^{2}H$ (b) for the base case.

Base case: pure diffusion, constant concentrations at Keuper and Malm boundary, initial concentrations derived from to maximum concentrations found today; cf. Table 9. Symbols as in Figure 9.

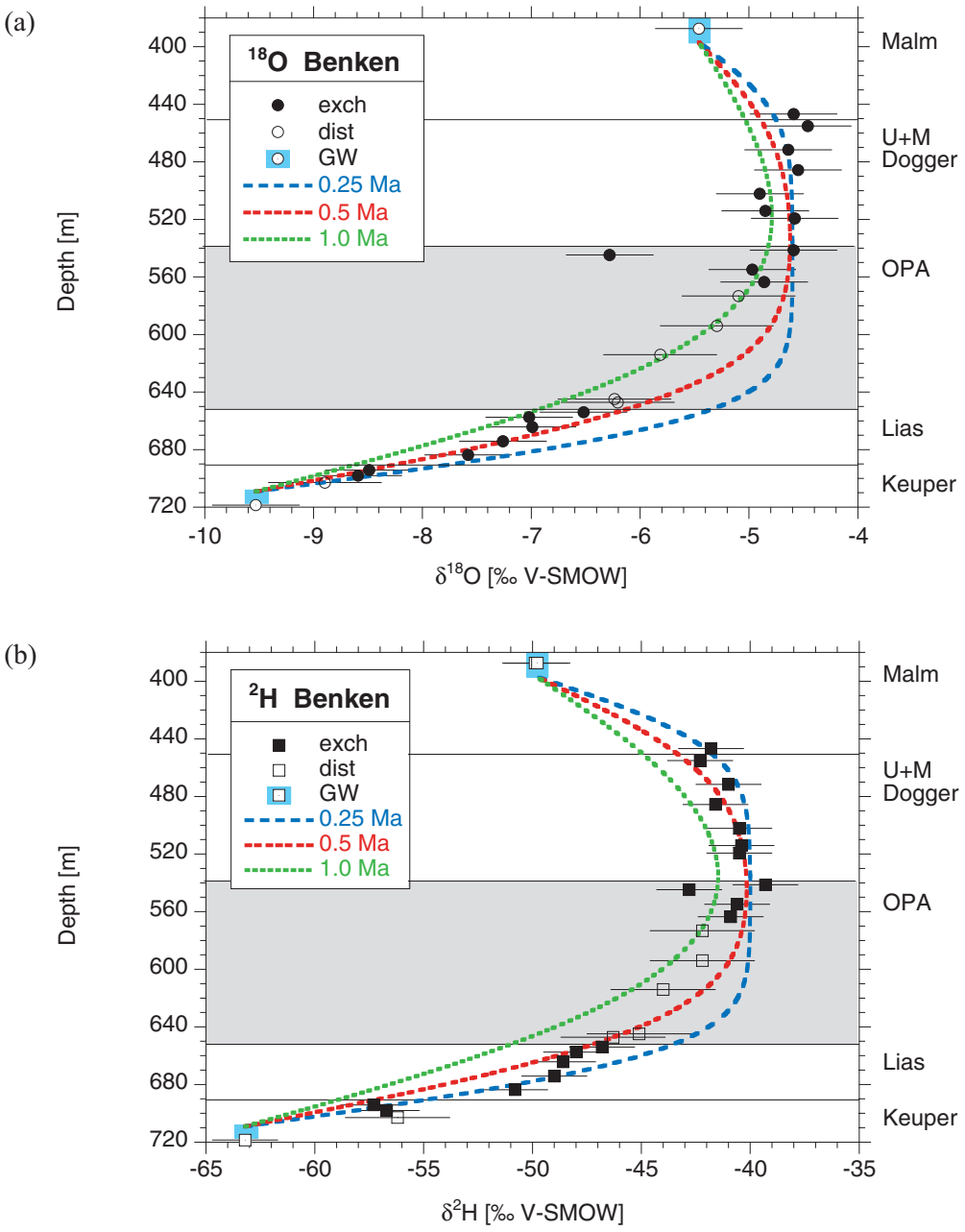

Figure 17: Effect of variation of evolution time t on the calculated profiles for $\delta^{18}O$ (a) and $\delta^{2}H$ (b) for the base case.

The curves for 0.5 Ma correspond to the best fits for the combined data sets, shown in Figure 15. The evolution times t were estimated from $\xi = (D_p\ t)^{0.5}$ with the laboratory diffusion coefficient D_p for HTO at 40°C, which represents approximately the relevant in-situ temperature. Symbols as in Figure 9.

6.1.2 Variation of Malm boundary condition

The upper boundary influences calculated values in the upper part of the profiles but has no effect on the estimated ξ. This is illustrated in Figure 18. Calculations for a zero-gradient upper boundary condition seem to describe the ^{18}O (but not the ^{2}H data) even better than the base case, but the same ξ as for a constant concentration at the Malm boundary was estimated. Using a mixing-cell boundary condition at the Malm interface led, depending on parameters, to profiles intermediate between those for a constant concentration and a zero gradient, but, again, always to the same value of ξ. Figure 18 also shows calculations for a constant concentration at the Malm boundary, but assuming a shorter evolution time or, correspondingly, a lower diffusion coefficient D_p for the upper part of the profile. The latter could originate from a somewhat lower porosity or lower temperature in the upper part of the profile.

Since there are no data in the uppermost part of the Dogger units, it cannot be decided, which boundary condition is most appropriate for the Malm interface. But, for all tested conditions at the Malm interface, the major part of the profile, and thus the value of the estimated ξ, was determined by the lower boundary. This supports also our independent hypothesis about the geological scenario.

6.1.3 Variation of initial condition

The effects of choosing higher initial concentrations are shown in Figure 19. The initial concentration for $\delta^{18}O$ was arbitrarily increased from –4.6 ‰ (Table 9) to –3.2 ‰ (Figure 19a). Approximate fits were obtained in this case for $\xi \approx 70$ to 90 m or $t \approx 1.5$ to 2.5 Ma. The corresponding initial concentration for $\delta^{2}H$ was chosen in two ways. Firstly, it was chosen so that a similar agreement between data and calculations was obtained for the same values of ξ or t (Figure 19b, initial value of –30 ‰). As is obvious, the agreement between measurements and simulations is not satisfactory for any ξ or t. The calculated curves have generally a different shape. For small ξ or short times, the deviations are especially large in the central regions, whereas for larger ξ or longer times, the data in the lower part are clearly underestimated. In addition, the ratio between the initial concentrations of $\delta^{2}H$ and $\delta^{18}O$ (see Figure 20) is far from any local trend of the data and thus not very likely.

Choosing an initial value for $\delta^{2}H$ according to the local trend (Figure 20) of pore-water composition, that is the ratio of the $\delta^{2}H$ and $\delta^{18}O$ values in the upper part of the profile, which might be more reasonable, gives an even worse picture (Figure 19c, initial value of –37 ‰). For a diffusion distance ξ of 70 to 90 m or an evolution time t of 1.5 to 2.5 Ma, as obtained for ^{18}O, the calculated curves all underestimate the measured data significantly. No value of ξ or t could be found in this case that led to a satisfying match with the data.

These observations led to the conclusion that today's maximum concentrations in the upper part of the profile represent approximately initial values prior to the activation of the Keuper aquifer. Even if we did not explicitly test non-uniform initial concentrations, the relatively good comparisons shown in Figure 15 support our assumption that initial values, before the relatively late drop in concentrations in the Keuper aquifer, were more or less constant throughout the formations.

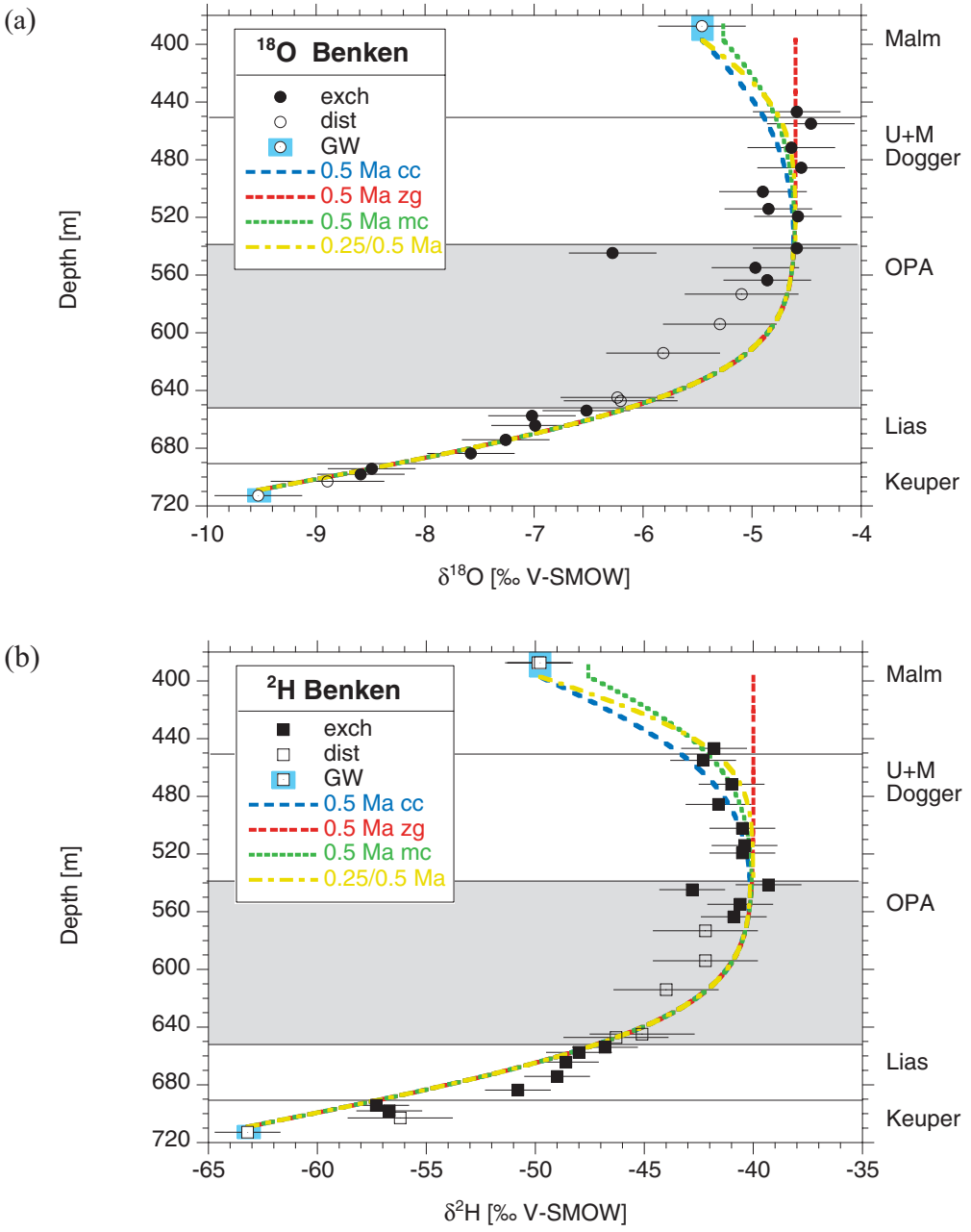

Figure 18: Effect of variation of the Malm boundary condition on the calculated profiles for $\delta^{18}O$ (a) and $\delta^{2}H$ (b).

Except for the Malm boundary condition, all model settings correspond to the base case. Malm boundary conditions: cc: constant concentration (base case); zg: zero gradient; mc: mixing cell; 0.25/0.5 Ma: cc, but lower evolution time (or lower diffusion coefficient D_p) in upper part of profile. In all cases, values for ξ identical to the base case were estimated. Symbols as in Figure 9.

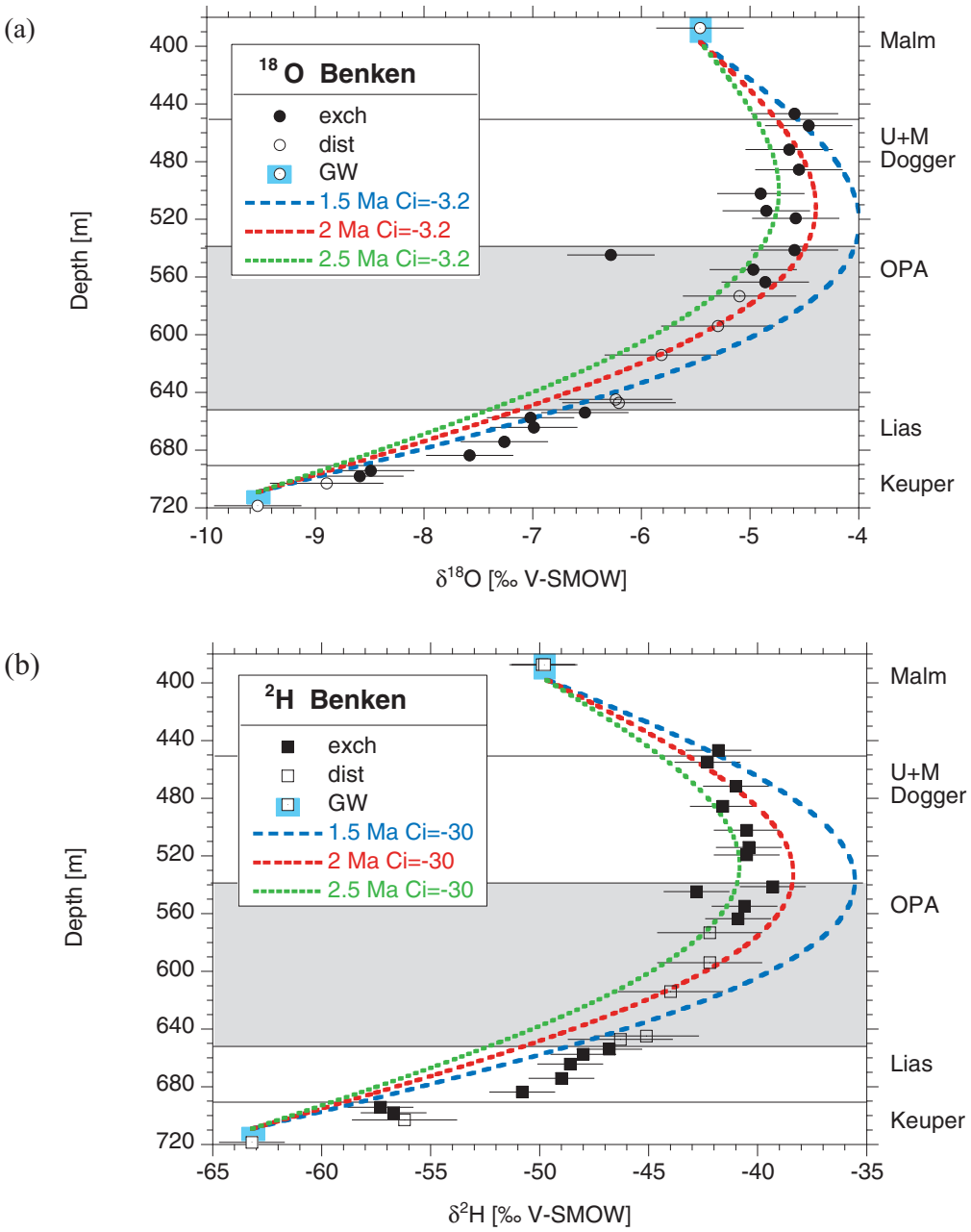

Figure 19: Influence of larger initial concentrations (as compared to the base case) on simulated concentration profiles of $\delta^{18}O$ (a) and $\delta^{2}H$ (b and c).

For (b), the initial concentration for $\delta^{2}H$ (C_i = –30 ‰) was adapted to get an approximate agreement between data and simulation at the same times as for $\delta^{18}O$. For (c), an initial concentration C_i = –37 ‰ was chosen for $\delta^{2}H$ according to the local trend of the pore water composition (see text and Figure 20). Symbols as in Figure 9. (Figure continued on next page.)

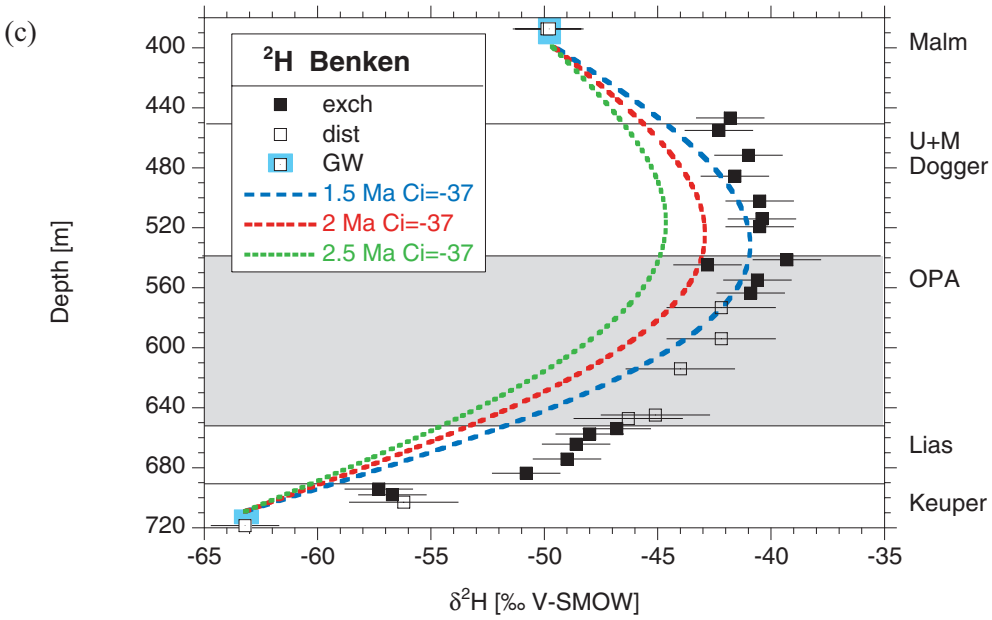

Figure 19: continued

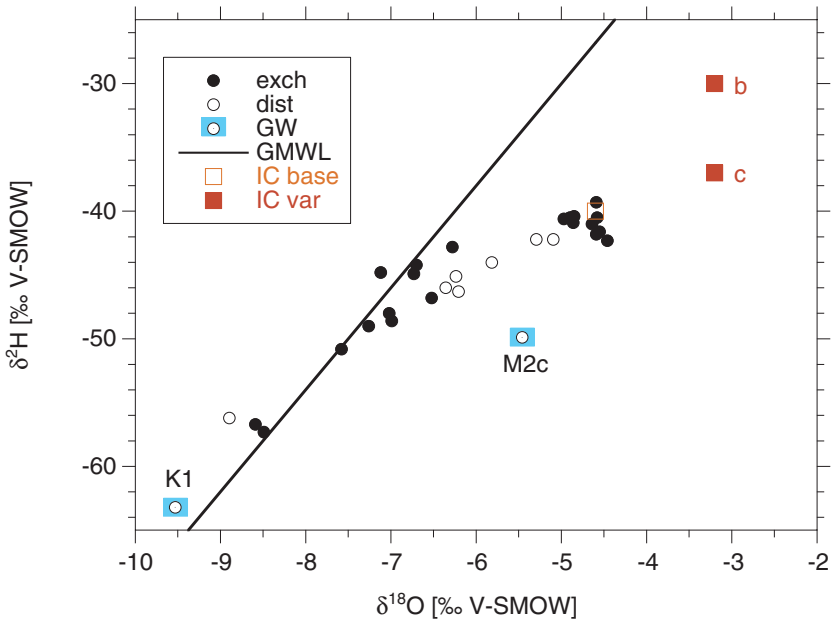

Figure 20: Comparison of assumed initial condition of base case and alternative initial conditions with pore water and ground water data.

IC base, open square: initial condition of base case; IC var, filled squares; initial conditions b and c according to Figure 19(b) and (c). Solid and open circles: pore water data; open circles with dot: ground water data; K1: Keuper; M2c: Malm.

6.1.4 Variation of Keuper boundary condition

Assuming a constant concentration at the Keuper boundary as in the base case (Figure 15) implies that the δ values dropped instantaneously. A more gradual decrease can be obtained with the mixing-cell boundary condition, depending on the values of the flushing rate ρ and the equivalent height ζ. In the following simulations, ζ was set equal to 10 m, which roughly represents equivalent aquifer thickness.

Figure 21 shows calculated $\delta^{18}O$ profiles for a flushing rate ρ of 2×10^{-5} a^{-1}. For this case, the time in which the aquifer element is flushed once with external water equals 5×10^4 a. This time is relatively short compared to diffusion times in the order of 5×10^5 a as estimated from the base case. Consequently, the simulated concentration drop in the Keuper occurs relatively rapidly. An approximate fit was obtained for an evolution time of about 1 Ma with this boundary condition. If the δ values of the inflowing water are like those observed today, that is –9.53 ‰, the concentration in the Keuper is overestimated even at larger evolution times (Figure 21, thick lines). If the inflow concentrations are decreased to about –10 or –10.5 ‰ for $\delta^{18}O$ (Figure 21, thin lines), the comparison becomes generally rather good, even slightly better than for the base case. Such a stable isotope composition would still be consistent with the climatic conditions during infiltration as derived from the measured values of the Keuper ground water.

Increasing the flushing rate to very large values leads finally to an instantaneous concentration drop like in the base case. Reducing the flushing rate, on the other hand, generally produced worse agreement between measurements and calculations, as is illustrated for $\delta^{18}O$ and $\rho = 2 \times 10^{-6}$ a^{-1} in Figure 22. If inflow concentrations like those observed today are used, concentrations drop too slowly at the lower boundary, and propagate too far up into the overlying Dogger units. Deriving a (rather poor) match of the data at low flushing rates of 2×10^{-6} a^{-1} or 2×10^{-7} a^{-1} requires unreasonably low isotope compositions of the inflowing water of –20 or –120 ‰, respectively, for $\delta^{18}O$ (not shown). Thus, such low flushing rates were rejected.

The flushing rate is related to the velocity v_{in} of the inflowing water and the lateral extent of the mixing cell V/A according to Eq. [4]. Assuming a lateral extent in the order of 10^4 m, which roughly corresponds to distances to infiltration zones, inflow velocities in the order of 0.2 m a^{-1} can be estimated from $\rho = 2 \times 10^{-5}$ a^{-1}. These velocities are more or less plausible compared to the hydraulic conductivity of about 10^{-7} m s^{-1} or 3 m a^{-1} of the Stubensandstein. This comparison should not be over interpreted, however, since the mixing-cell approach with constant inflow concentration does not exactly represent a two-dimensional situation.

To summarise, the following can be stated. The simulations with a mixing-cell boundary at the Keuper interface indicate clearly that the concentrations in this aquifer dropped relatively rapidly. In the base case, where an instantaneous drop was assumed, the evolution time was estimated to be about 0.5 Ma. For cases with more gradual concentration decreases, the estimated evolution times increase to about 1 Ma at most.

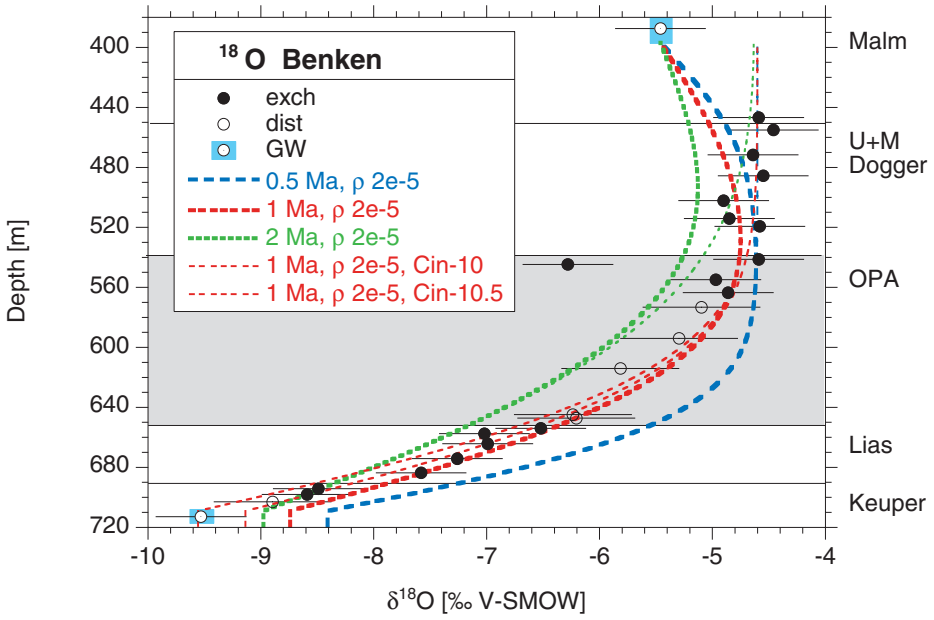

Figure 21: Simulated concentration profiles of $\delta^{18}O$ for a mixing-cell boundary condition at the Keuper aquifer, with a flushing rate ρ of 2×10^{-5} a^{-1}.

Thick lines: Keuper inflow concentration C_{in} of –9.53 ‰ and constant concentration at upper boundary, at three different evolution times; thin lines, lower part of Figure: Keuper inflow concentration C_{in} of –10.0 and –10.5 ‰ at an evolution time of 1 Ma; thin lines, upper part of Figure: as thick lines, but for zero gradient at upper boundary. Symbols as in Figure 9.

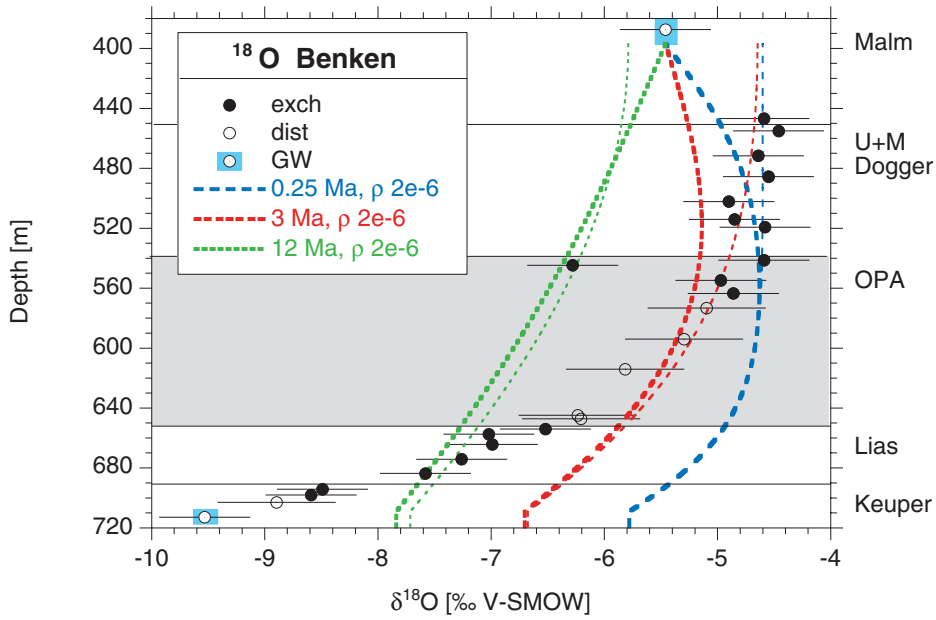

Figure 22: Simulated concentration profiles of $\delta^{18}O$ for a mixing-cell boundary condition at the Keuper aquifer, with a flushing rate ρ of 2×10^{-6} a^{-1}.

Simulations are shown for three evolution times. Keuper inflow concentration C_{in} of -9.53 ‰. Thick lines: constant concentration at the upper boundary; thin lines: zero gradient at the upper boundary. Symbols as in Figure 9.

6.1.5 Combined effects of boundary and initial conditions

In most cases so far only one boundary or initial condition at a time was varied from the base case. To test combined effects, we compared simulations for zero gradient at the upper boundary, an increased initial value of –3.2 ‰ or –3 ‰, and constant or time dependent concentrations at the lower boundary with the ^{18}O data. The results (Figures 21, 22, 23, and 24) corroborate the conclusions drawn above based on individual variations of boundary or initial conditions. In Figures 21 and 22, calculations for a mixing-cell condition at the Keuper aquifer and a zero-gradient condition at the Malm interface are shown in addition to those with constant concentration at the Malm interface. Again it became obvious that the upper boundary condition has only a minor impact, especially if the lower part of the profile is described adequately. Figures 23 and 24 demonstrate that, for an increased initial concentration of –3.2 ‰ or –3 ‰, respectively, no reasonable fit can be obtained for any diffusion distance ξ, irrespective of the combination of upper and lower boundary conditions.

6.1.6 Influence of advection

Upward or downward advective flow across the Dogger units may have occurred during certain times, and at certain locations. However, we have no detailed information that would allow us to model such time- and space-dependent flow reliably. To obtain at least an idea about the possible influence of advection, we investigated the most simple case: constant upward or downward flow. Figure 25 illustrates the typical influence of advective flow on the simulations, for an advective velocity $v = 2 \times 10^{-12}$ m s^{-1} (upward) or $v = -2 \times 10^{-12}$ m s^{-1} (downward), at a given evolution time $t = 0.5$ Ma.

Since, as stated, the evolution time is not known exactly *a priori*, we estimated it from the data for each velocity. The procedure was the following. For pre-set values of the velocity v (or v/D_p, respectively), we minimised the mean squared deviations $\Delta = \chi^2/n$ between calculations and measurements, where n is the number of data points, by adjusting the evolution time t (or ξ, respectively) for the combined data sets.

Figure 26 shows the best-fit curves for relatively small, constant velocities $v = 2 \times 10^{-12}$ m s^{-1} (upward) and $v = -2 \times 10^{-12}$ m s^{-1} (downward), together with the best-fit curve of the base case ($v = 0$ m s^{-1}). It can be seen that for such low velocities, the deviations from the base case are relatively small, especially for upward flow. However, in both cases the mean squared deviation per data point, Δ, is somewhat larger than for the base case with $v = 0$ m s^{-1} (see following paragraph). Figure 27 shows best-fit curves for velocities $|v| = 2 \times 10^{-11}$ m s^{-1}. At such velocities, the differences to the base case are already very large, and no reasonable fits could be obtained at all, which is also reflected in the large Δ values.

A summary over minimum average deviations Δ between measurements and simulations for various advective velocities $|v|$ is presented in Figure 28. A positive v means upward flow, and a negative v means downward flow. The numbers in the plot denote the evolution times estimated from ξ with the laboratory diffusion coefficient at 40 °C of 1×10^{-10} m^2 s^{-1}. Using this value for all velocities means that we neglected hydrodynamic dispersion, which will not contribute much at these low velocities anyway. In general, upward velocity led to smaller, and downward velocity to larger, evolution times. For velocities smaller than about 2×10^{-12} m^2 s^{-1} the estimated evolution times varied only over a small range (about 0.25 - 0.7 Ma). For larger velocities, clearly smaller or larger evolution times were estimated, but the fits were so poor that these values should not be considered.

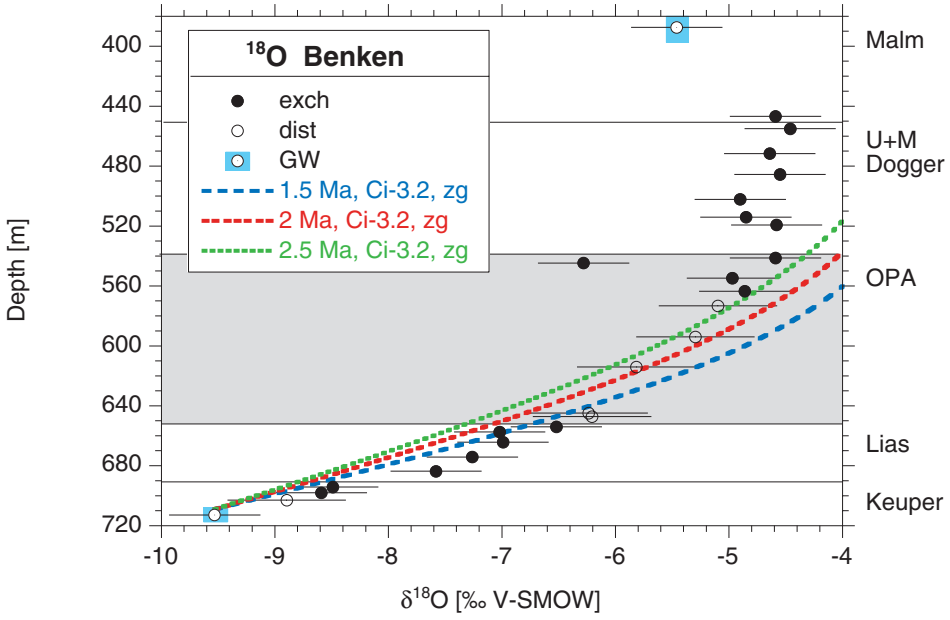

Figure 23: Calculations for $\delta^{18}O$ for combined effects of increased initial concentration (C_i = -3.2 ‰), zero gradient upper, and constant concentration lower boundary condition.

Simulations for three evolution times are shown. Symbols as in Figure 9.

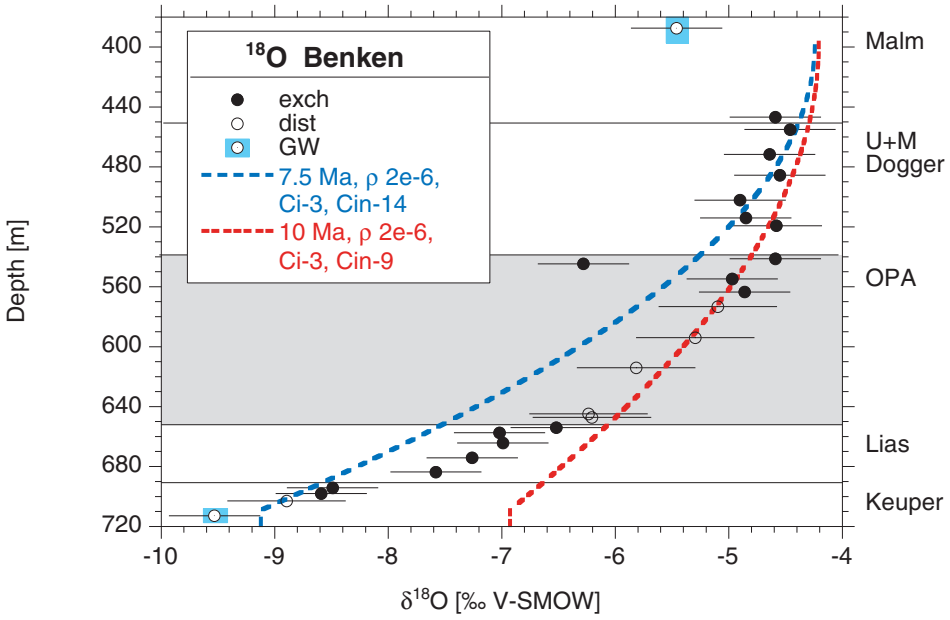

Figure 24 Calculations for $\delta^{18}O$ for combined effects of increased initial concentration (C_i = -3 ‰), zero gradient upper, and mixing-cell lower boundary condition.

Keuper: flushing rate ρ of 2×10^{-6} a^{-1}, inflow concentrations C_{in} of –9. ‰ and –14 ‰, respectively. Symbols as in Figure 9.

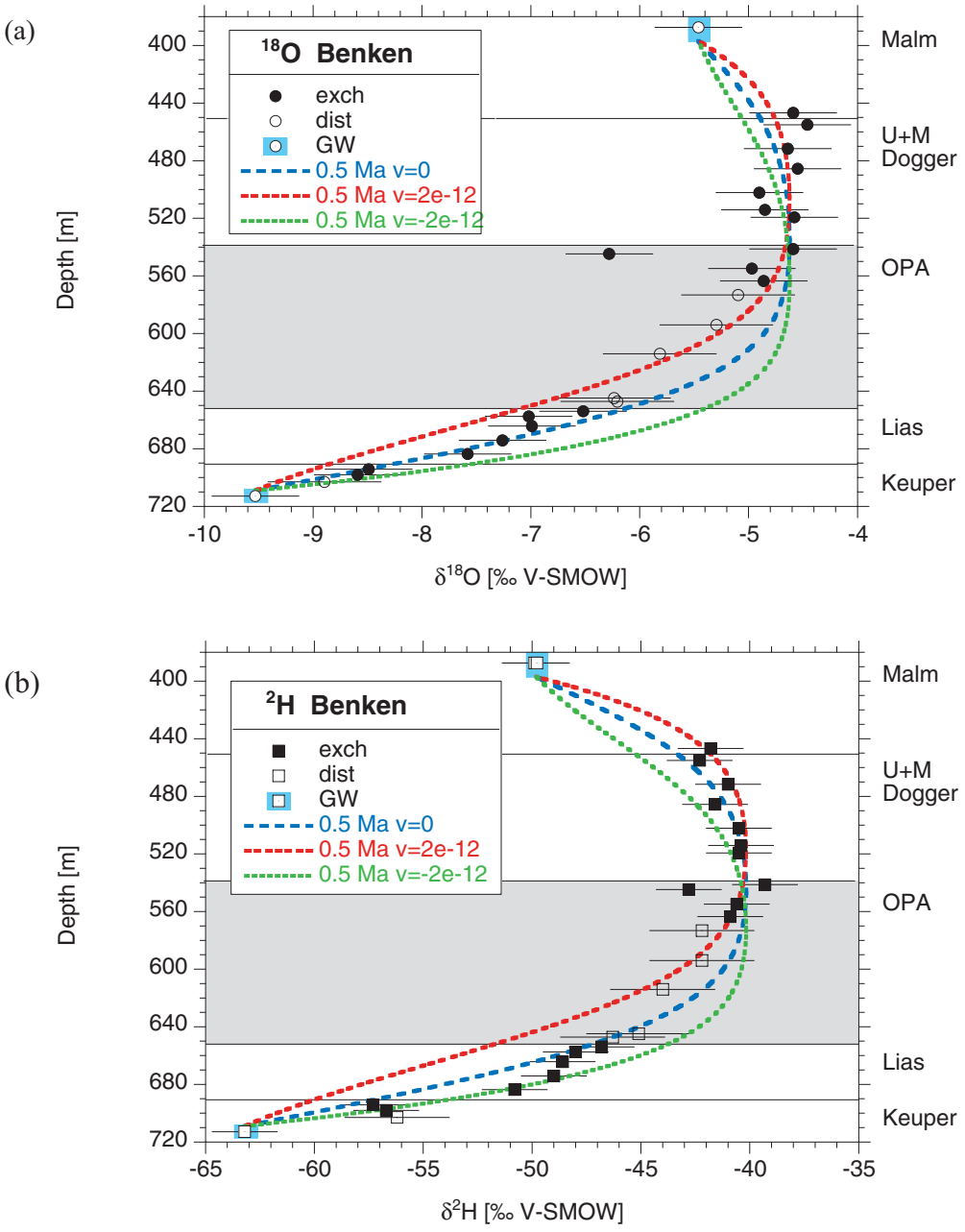

Figure 25: Influence of relatively small upward or downward advective velocity, as compared to pure diffusion, on simulated concentration profiles of $\delta^{18}O$ (a) and $\delta^{2}H$ (b), at an evolution time of 0.5 Ma.

$v > 0$: upward velocity; $v < 0$: downward velocity; $v = 0$: pure diffusion. Symbols as in Figure 9.

The relative importance of advective versus diffusive or dispersive mass transfer can be estimated from the Peclet number $Pe = |v|\ L/D_p$. If this dimensionless number is smaller than about unity, advection is negligible and diffusion dominates over the length scale L. The corresponding limit for $|v|$ equals in our system with $L \approx 300$ m and $D_p \approx 1 \times 10^{-10}$ m^2 s^{-1} about 3.3×10^{-13} m s^{-1}, and is indicated by the vertical line in Figure 28. Overall, the smallest minimum deviations Δ were found to the left of this line, where diffusion dominates. When advective flow also contributed to transport, the mean squared deviations Δ increased, especially for downward flow.

It is interesting to compare velocities used in the simulations with those estimated from the present-day hydraulic situation in this region (Nagra 2001). The hydraulic gradient between the Keuper and Malm aquifer of about –0.5 m m^{-1} points today to upward flow, neglecting the slight overpressures within the low-permeability zones (cf. Figure 3). With a hydraulic conductivity perpendicular to the layering of about 2×10^{-14} m s^{-1} and a generic water-filled porosity of about 0.1 m^3 m^{-3}, one calculates an advective velocity of 1×10^{-13} m s^{-1} for water tracers that can spread over the whole water-filled pore space. This value leads to $Pe = 0.3$, which also indicates that today advection is hardly an important transport mechanism.

As stated, assuming spatially and temporally constant flow over the last million years is a very simplified scenario. Loading and unloading of the surface with ice following glaciation may have caused variable horizontal or vertical water flow. But, since the Dogger units were once covered with about 1 000 m of sediments more than today (Leu et al. 2001) and thus are considered to be overconsolidated, it is unlikely that glaciation has caused large changes of porosity and corresponding advective flow. Horizontal strain may also lead to upward and downward flow of water. Calculations of velocities based on present-day fluid pressures within the Dogger units (cf. Figure 3) led to values $|v|$ between zero and about 9×10^{-13} m s^{-1}, with maximum values occurring only right at the Malm and Keuper interfaces. Again, such velocities have only a very small effect on simulated isotope profiles, as was also verified with the numerical calculations displayed in Figure 29 (Kosakowski & Gimmi 2001).

Figure 28 clearly shows that the assumption of diffusion dominated isotope exchange leads to minimal deviations between measured data and simulations. Diffusion dominated means, that advection is either absent or so small, that it hardly influences the calculations. The latter is true in our system for velocities smaller than about 3×10^{-13} m s^{-1}. Conversely, we conclude from Figure 28 that advection did not leave any detectable signature in the isotope profiles observed today at Benken. This conclusion is also supported by the low velocities estimated from measured hydraulic conductivities and present-day hydraulic gradients across, or overpressures within, the Dogger units.

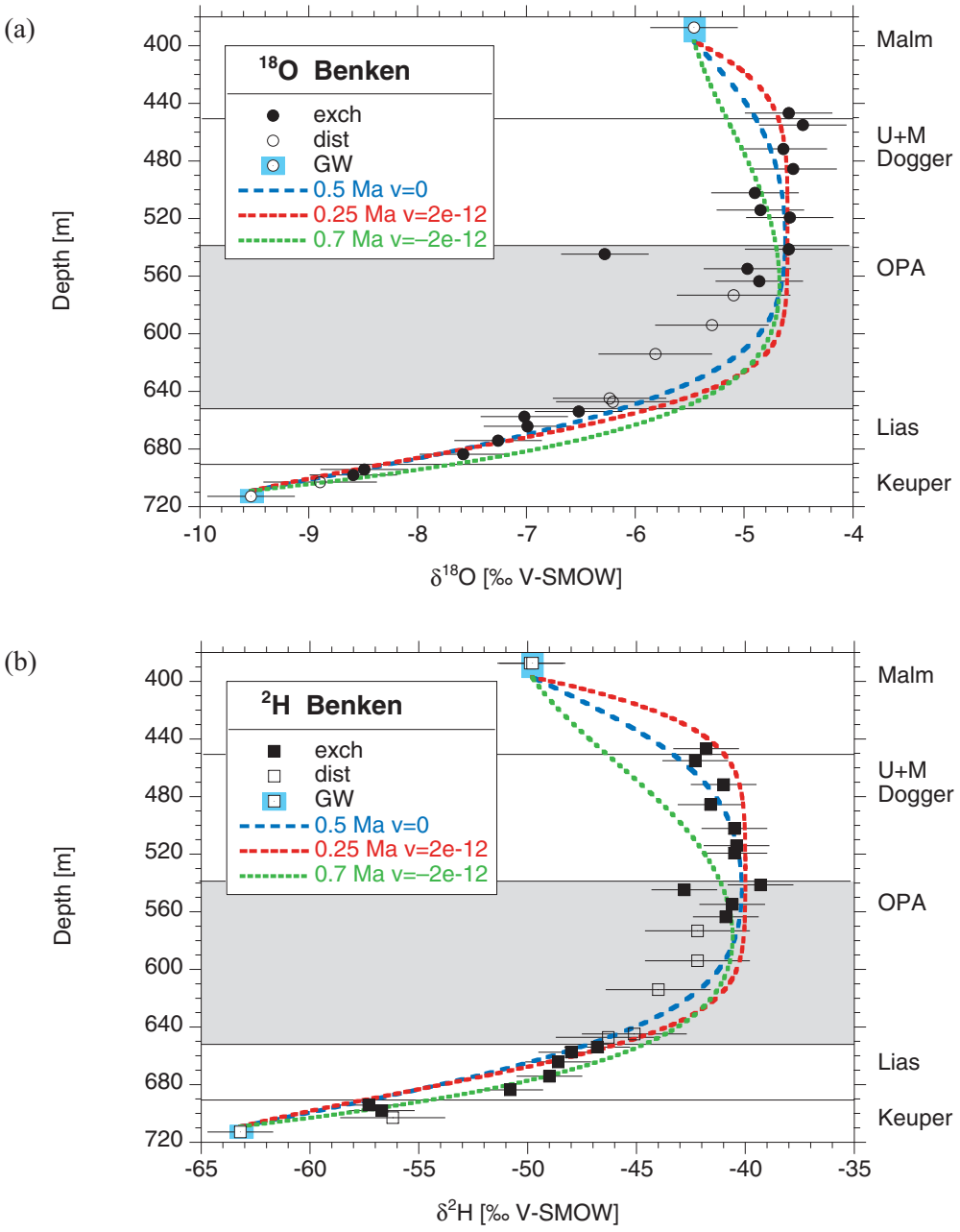

Figure 26: Influence of relatively small upward or downward advective velocity, as compared to pure diffusion, on fitted concentration profiles of $\delta^{18}O$ (a) and $\delta^{2}H$ (b).

$v > 0$: upward velocity; $v < 0$: downward velocity; $v = 0$: pure diffusion. Symbols as in Figure 9.

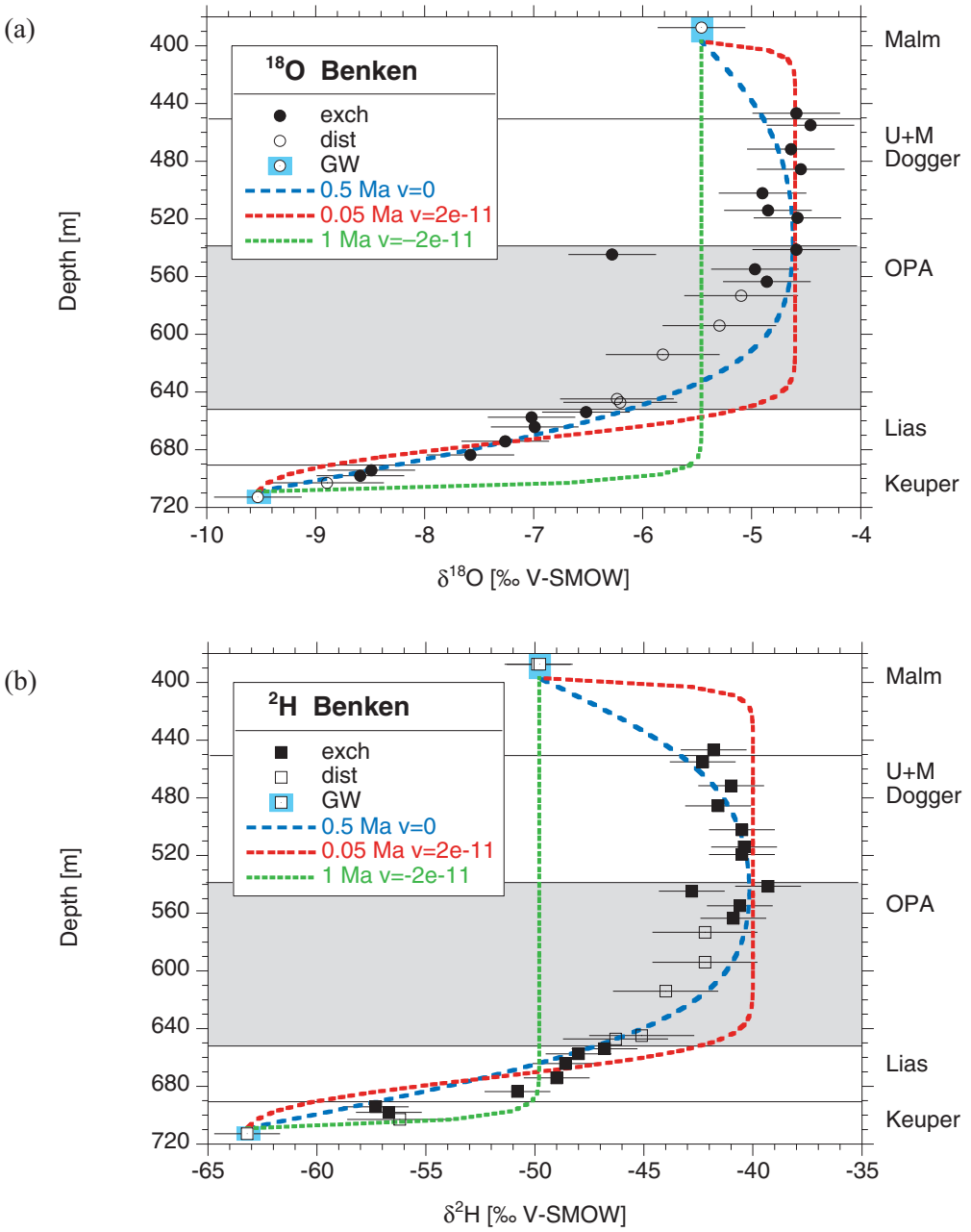

Figure 27: Influence of slightly increased upward or downward advective velocity, as compared to pure diffusion, on fitted concentration profiles of $\delta^{18}O$ (a) and $\delta^{2}H$ (b).

$v > 0$: upward velocity; $v < 0$: downward velocity; $v = 0$: pure diffusion. Symbols as in Figure 9.

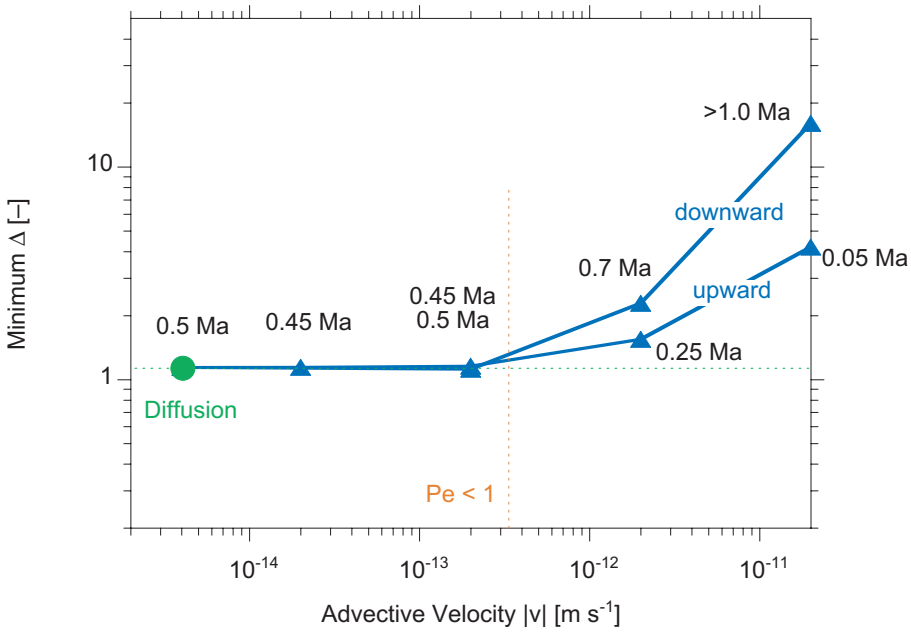

Figure 28: Calculated minimum average deviations Δ vs. absolute values of advective velocity v for boundary and initial conditions of the base case.

See Eq. [13] for definition of Δ. Labels next to points or triangles indicate evolution times for upward of downward flow, as estimated from diffusion distance ξ with the laboratory diffusion coefficient D_p. The point on the left, and the horizontal line, indicate minimum Δ for pure diffusion.

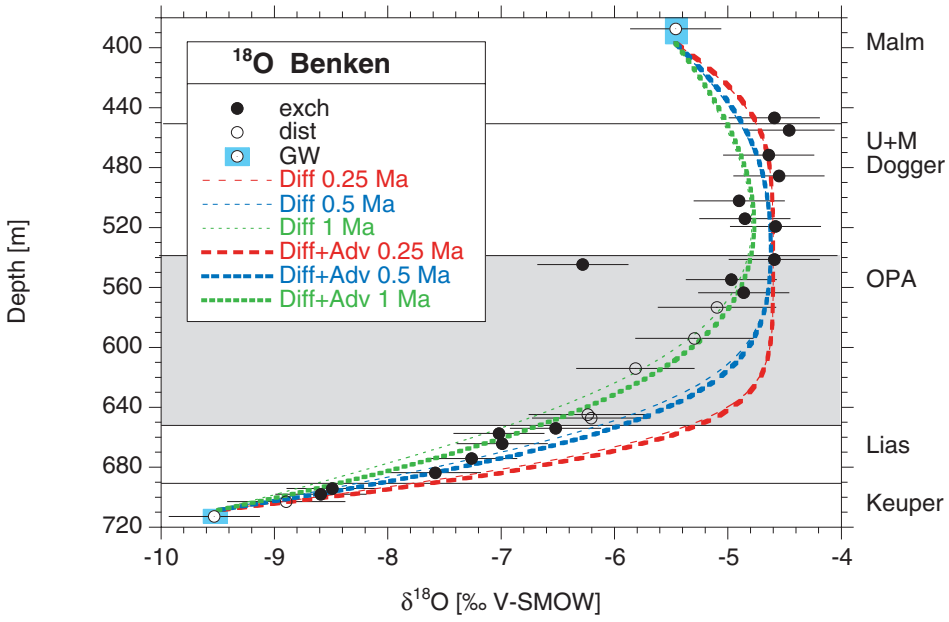

Figure 29: Influence of depth dependent advective velocities, estimated based on a hydraulic conductivity of 2×10^{-14} m s^{-1} and present-day hydraulic gradients within the low-permeability zones, on simulated profiles of $\delta^{18}O$.

Data from Kosakowski & Gimmi (2001). Thick lines: simulations with advection; thin lines: simulations for the base case. Symbols as in Figure 9.

6.1.7 Summary of results for stable water isotopes

Values of $\delta^{18}O$ and $\delta^{2}H$ were determined in the pore fluid of low-permeability formations at Benken in north-eastern Switzerland. The formations are of Jurassic and uppermost Triassic age, and they were sampled at depths between about 400 and 700 m. A new technique based on diffusive exchange of isotopes (Rübel & Sonntag, 2000; Nagra, 2001) had to be used to obtain the pore-water isotopic composition from the rock samples, because the conventionally used vacuum-distillation method was proven to be inaccurate. The latter suffered from incomplete distillation, which results in fractionation effects that cause the measured isotope ratios to deviate from those present *in situ*. The data sets provide a unique opportunity to evaluate the transport behaviour of Jurassic sedimentary rocks on very large spatial and temporal scales. The measured profiles seemed to be influenced mainly by mass exchange with the underlying Keuper aquifer. To quantify these processes, we performed a series of simulations with an advective-diffusive transport model with constant parameters. Varying initial and boundary conditions as well as model parameters allowed the following specific conclusions to be made:

- Initial isotope ratios before the onset of flow in the local Keuper aquifer were shifted to lower values with respect to the initial marine pore water. They correspond to values measured in the upper and middle part of the Dogger units.
- Some time after activation of flow, values in the Keuper aquifer decreased rapidly to meteoric values. A slow concentration decrease cannot reproduce the observed data.
- Conditions at the Malm boundary had only a small effect on the observed profiles. The data in the upper part do not allow discrimination between different possible upper boundary conditions.
- The profiles evolved mainly under the influence of molecular diffusion. No signature of advective flow could be detected.
- Depending on boundary conditions, a diffusion distance $\xi = (t\ D_p)^{0.5}$ of about 40 to 56 m was estimated. This corresponds to evolution times of about 0.5 to 1 Ma based on a laboratory diffusion coefficient D_p at 40 °C (Van Loon & Soler, 2004) of about 1×10^{-10} m^2 s^{-1}.
- Additional uncertainty about relevant temperatures and processes (e.g. slight variability of porosities and diffusion coefficients) increases the estimated span of evolution to about 0.2–1.5 Ma.

Consistency between data and a model, as observed for the stable water isotopes, indicates that the model may be adequate, but it does of course not prove that it is the only suitable model concept. But, the larger the ensemble of observations that are consistent with a given model, the more confident one can be that the most important features were included in it. In this sense, the modelling of the chloride and $\delta^{37}Cl$ data that is presented in the next sections is very important.

6.2 Chloride and $\delta^{37}Cl$

In Section 6.2.1, we present some generic calculations of Cl and $\delta^{37}Cl$ profiles. They illustrate the relations between the total Cl concentration and the relative excess of the heavy isotopes, $\delta^{37}Cl$, during transport. We then use the modelling results for the stable water isotopes as a starting point and check the conclusions reached with those data against the Cl and $\delta^{37}Cl$ data. Additional calculations are included, where suggested by the data, or to investigate the sensitivity to specific parameters for Cl and $\delta^{37}Cl$. Section 6.2.2 presents the results for the base case, one of the scenarios considered as possible according to the results of the stable water

isotopes. Sections 6.2.3 (ratio of diffusion coefficients) and 6.2.4 (Cl-accessible porosity) deal with additional uncertainties introduced by specific parameters required to model transport of Cl and δ^{37}Cl. Sections 6.2.5 (Malm boundary), 6.2.6 (initial conditions), and 6.2.7 (Keuper boundary) present variations of boundary and initial conditions similar to those tested for the stable water isotopes, and Section 6.2.8 demonstrates the effect of advective flow. The modelling results for the Cl and δ^{37}Cl data are summarised in Section 6.2.10.

6.2.1 Generic calculations

In this section, some simulations for diffusive transport are presented for a domain with the same extent as the low-permeability zones in Benken. Boundary and initial conditions were, however, more or less arbitrarily chosen to demonstrate the relations between Cl and δ^{37}Cl. Simulations are shown for a very large (and for the Benken site unrealistic) time span just to illustrate the temporal behaviour. Note that times were calculated based on a pore diffusion coefficient D_p of 5×10^{-11} m^2 s^{-1}, which is one half of the value for stable water isotopes. Such a ratio of D_p between Cl and water isotopes was found in laboratory experiments (see Section 6.2.2). A ratio of diffusion coefficients between ^{35}Cl and ^{37}Cl of 1.002 was assumed (see Section 6.2.3).

Figure 30 shows simulations for constant, low boundary concentrations for Cl (500 mg L^{-1}) on both sides of the domain, which initially contained Cl at a concentration of 6 000 mg L^{-1}. Figure 31 presents results for a zero-gradient boundary condition for Cl at the lower interface. Since only diffusive transport was taken into account, this boundary condition prevents all solute exchange across the lower interface. In Figure 32, the lower interface is kept at the (initial) value of 6 000 mg L^{-1} at all times. For all three examples, identical conditions for δ^{37}Cl were assumed: $\delta^{37}Cl(z,t = 0) = 0$ ‰, $\delta^{37}Cl(z = 0,t) = 0$ ‰, $\delta^{37}Cl(z = L,t) = 0$ ‰.

In Figure 30, diffusion occurs symmetrically to both sides. The maximum Cl concentrations drop then faster than in Figure 31, where diffusive transport occurs only towards one side. In fact, Figure 31 represents a situation identical to the upper or lower half of Figure 30, but with a size of the domain two times as large and a correspondingly slower loss of solutes. A large gradient for Cl and thus a large diffusive flux leads initially to peaks in δ^{37}Cl. During that phase, the Cl and δ^{37}Cl profiles look rather different, with maximum Cl concentrations, but minimum (or at least low) δ^{37}Cl values in the centre (Figure 30, two-sided diffusion) or at the bottom (Figure 31, one-sided diffusion) of the domain. With increasing time of diffusion, the δ^{37}Cl peaks in Figure 30 become broader and, in a later stage, may even merge or smear to a single peak, similar in shape to the Cl peak. For the two-sided diffusion of Figure 30, with a relevant distance of about 150 m, this happens at times larger than about 2 – 4 Ma. Maximum δ^{37}Cl values of about 2.5 ‰ are reached then within about 10 Ma. In case of one-sided diffusion in Figure 31, with a relevant distance of about 300 m, it lasts about 10 Ma, until the δ^{37}Cl peak has smeared over the domain, and maximum δ^{37}Cl values of about 2.5 ‰ are only reached at much longer times.

For one-sided diffusion with unequal, constant concentrations on both sides (Figure 32), Cl and δ^{37}Cl look similar to Figure 31 for the first 2 – 4 Ma, before the different lower boundary condition has come into play. Later, after about 10 Ma, the Cl profile is already rather close to the linear steady state. Consequently, the enrichment with ^{37}Cl increases no more, and maximum δ^{37}Cl values are only about 0.7 ‰.

For all cases considered, the steady-state profiles of δ^{37}Cl are identical, namely flat, but the time to reach them varies considerably. It is longest for the largest amount of Cl that can diffuse out

(i.e. largest mass difference between initial and steady state), and for the largest diffusion distance (Figure 31).

From the calculations presented in Figures 30 – 32, we learned the following about diffusive fractionation of $\delta^{37}Cl$:

- Distinct peaks of $\delta^{37}Cl$ are typical for relatively steep Cl gradients (that is, large Cl flux) and a relatively young perturbation.
- For larger diffusion times (more than about 2 – 10 Ma in our cases) such peaks typically disappear or smear out.
- The larger the total amount of Cl that can diffuse out of a domain, the larger are the maximum $\delta^{37}Cl$ values reached in the domain.
- Concentrations close to the steady state seem to be reached faster by Cl profiles than by $\delta^{37}Cl$ profiles (amplification of differences by $\delta^{37}Cl$ values)
- The $\delta^{37}Cl$ values are relatively sensitive to boundary conditions for Cl; the inverse is, of course, not true.

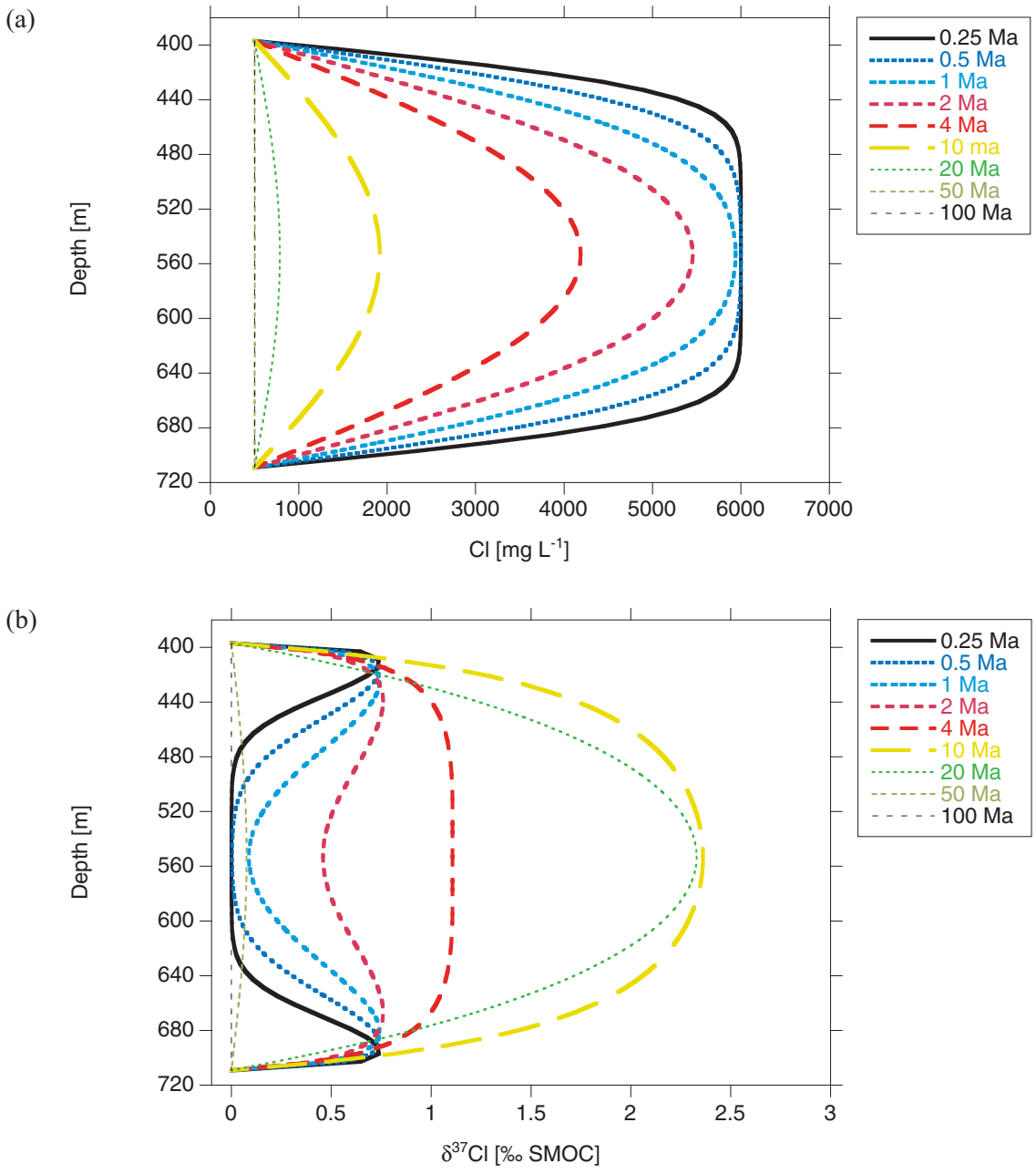

Figure 30: Profiles of chloride (a) and $\delta^{37}Cl$ (b) calculated for constant concentrations on both sides of the domain.

Concentrations of C_{Cl} = 500 mg L^{-1} and $C_{\delta 37Cl}$ = 0 ‰ at both boundaries.

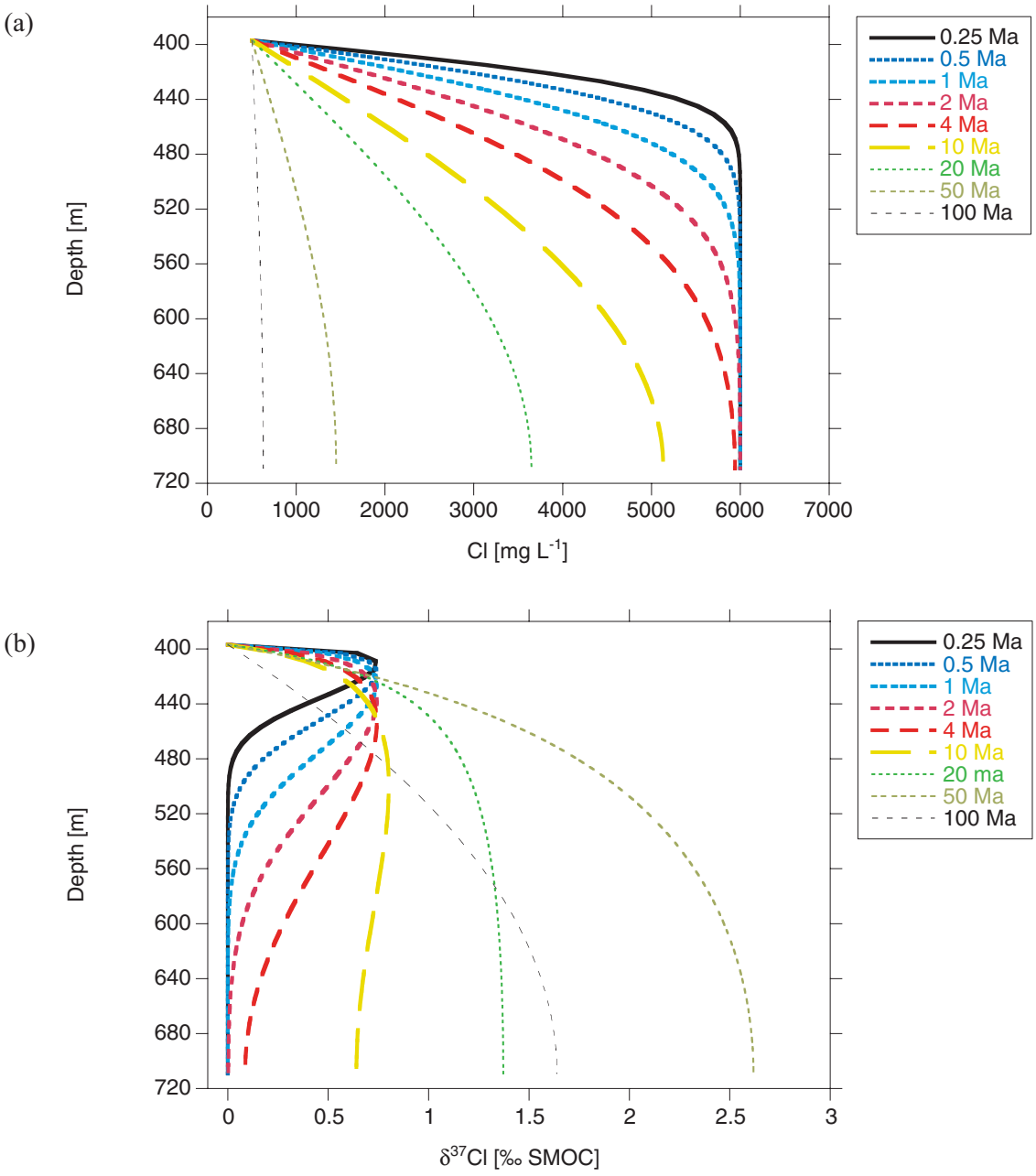

Figure 31: Profiles of chloride (a) and $\delta^{37}Cl$ (b) calculated for constant Cl concentration at top and zero gradient at bottom.

Concentration of $C_{Cl}(z = L,t)$ = 500 mg L^{-1}. Boundary and initial conditions for $\delta^{37}Cl$ as in Figure 30.

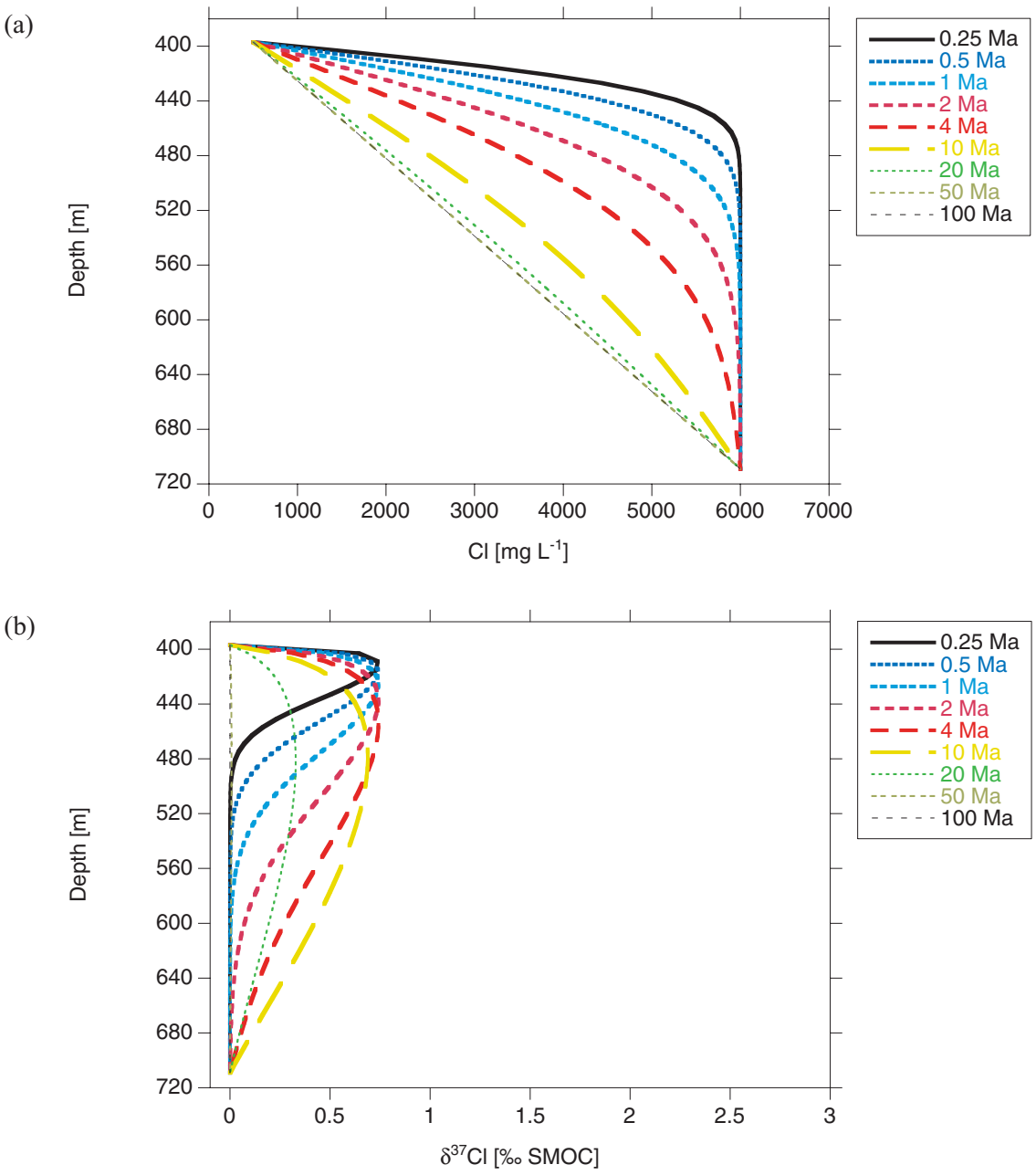

Figure 32: Profiles of chloride (a) and $\delta^{37}Cl$ (b) calculated for constant, but different Cl concentrations at the two interfaces.

Concentrations of $C_{Cl}(z = L,t)$ = 500 mg L^{-1} and $C_{Cl}(z = 0,t)$ = 6 000 mg L^{-1}. Boundary and initial conditions for $\delta^{37}Cl$ as in Figure 30.

6.2.2 Base case

The base case simulations for Cl and $\delta^{37}Cl$ are shown in Figure 34. The value of $\xi = (t\, D_p)^{0.5}$ from the base case simulations of the stable water isotopes in the pore water was about 40 m (Section 6.1.1). Based on the geologic scenario, it is considered as reasonable to assume identical evolution times t for the Cl profiles and for the stable water isotopes, that is to assume that Cl concentrations and stable water isotope values in the Keuper aquifer dropped at the same time. If Cl and water isotopes had the same pore diffusion coefficients D_p, this would then lead to identical values of ξ for Cl and stable water isotopes. Laboratory diffusion measurements for samples from Mont Terri and Benken (Nagra 2002, Van Loon & Soler 2004) indicated that the pore diffusion coefficient D_p of Cl perpendicular to the layering is typically somewhat lower than the D_p of water isotopes (see Figure 33), with a factor in the range of about 0.2 to 0.8 and an average of about 0.5. For transport parallel to the layering, the difference is smaller and the factors are generally closer to unity (average of about 0.9). One should note, however, that the laboratory diffusion coefficients are measured with (radioactive) tracers in constant background concentrations, and thus represent (true) tracer diffusion coefficients. In the field, a total Cl gradient exists, and Cl cannot diffuse independently from other solutes. To maintain electroneutrality, a counter diffusion of other anions or, more likely, a co-diffusion of cations has to occur, which influences the net diffusive transport of Cl (see e.g. Cussler 1984; Flury & Gimmi 2002). There are some hints that cations diffuse faster (a factor of about 1.2 - 2.2 for Na^+) through Opalinus Clay than anions (Van Loon & Soler 2004). Thus, the co-diffusion of Na^+ could possibly increase the net diffusion of Cl as compared to the tracer diffusion of Cl. To cover the uncertainty about the relevant (net) pore diffusion coefficient of Cl in the field, we will present simulations for two values of ξ or, correspondingly, two values of evolution times when calculated with $D_p = 5 \times 10^{-11}$ m^2 s^{-1}, i.e. half the value of the water isotopes. The first, $\xi = 28.1$ m, leads to $t = 0.5$ Ma, the second, $\xi = 39.7$ m, to $t = 1$ Ma. The latter corresponds also to an evolution time $t = 0.5$ Ma, if the same $D_p = 1 \times 10^{-10}$ m^2 s^{-1} as for the water isotopes is used. The corresponding simulations are shown as thick lines in Figure 34.

Comparing data and simulations, we see (Figure 34(a), thick lines), that the range of "predictions" for Cl based on the analysis of the stable water isotopes matches the observed data approximately. There are, however, some deviations at the boundary between Malm and upper Dogger, and in the Lias, that are clearly larger than the indicated errors of the observations. Especially the data in the Lias cannot be simulated by a single diffusive event, unless the errors are larger than indicated. Similar conclusions are to be drawn from the modelling of the $\delta^{37}Cl$ data (Figure 34(b), thick lines). The overall trend of the simulations follows the data more or less, but there are some significant deviations, mainly in the upper and partly also in the lower sections.

Based on the generic calculations presented in 6.2.1, the relatively large values of $\delta^{37}Cl$ close to the upper and lower boundary and the relative minimum in the centre of the domain indicate probably (still ongoing) diffusive exchange, even though the exact shapes cannot be modelled. In the following, we will test slightly different scenarios that may lead to increased $\delta^{37}Cl$ values in the upper and lower parts of the profiles.

(a)

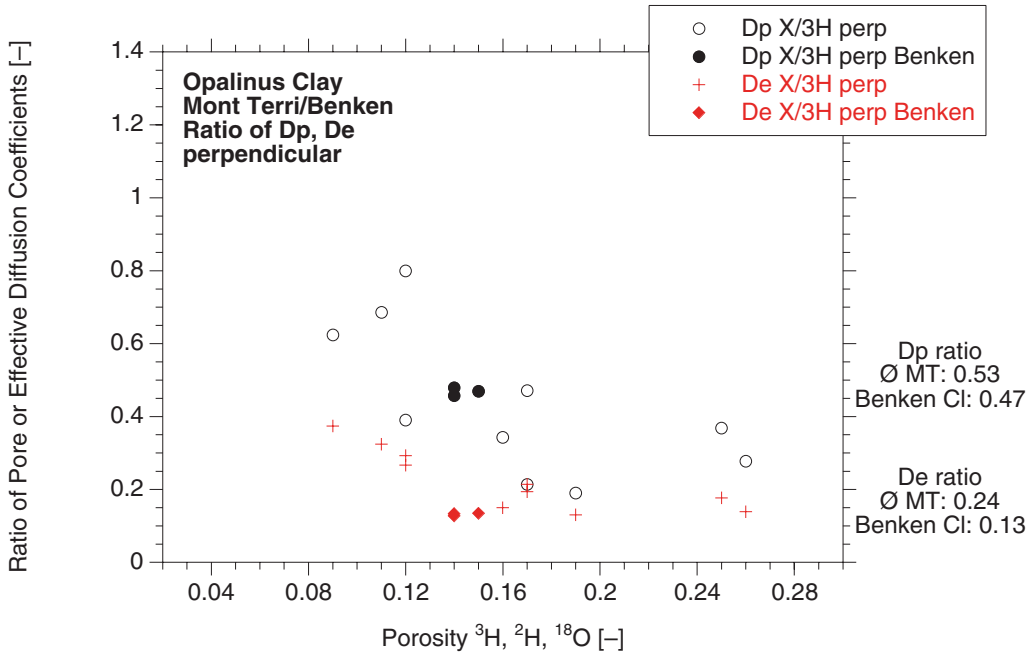

(b)

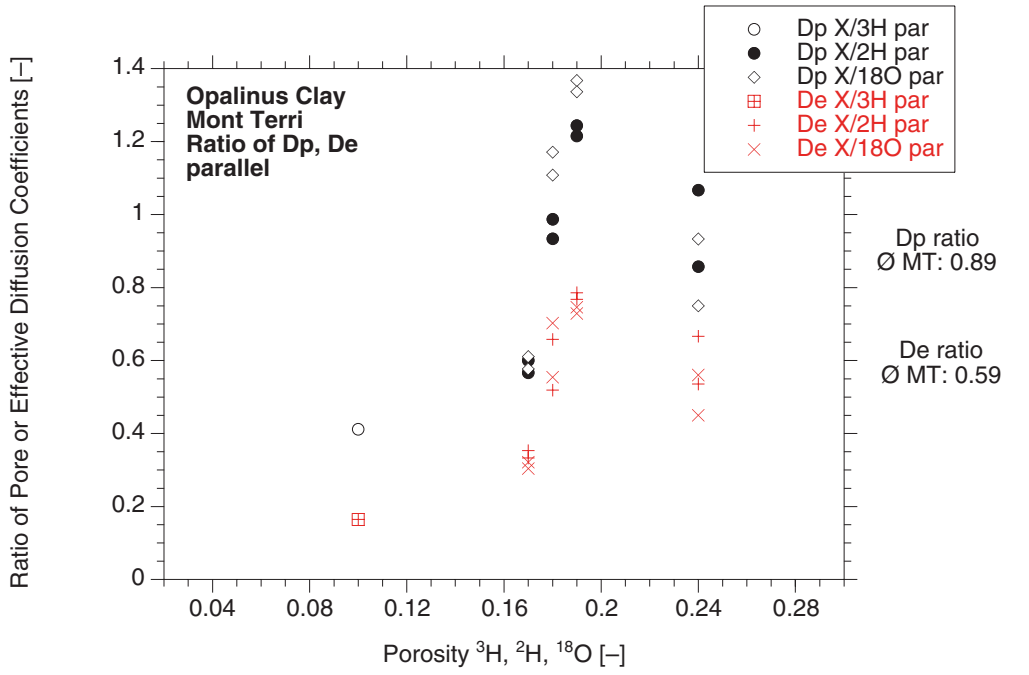

Figure 33: Ratio of pore diffusion coefficients D_p, and effective diffusion coefficients $D_e = \varepsilon D_p$, between anions and water tracers for samples from Mont Terri and Benken.

Data from Nagra (2002) and Van Loon & Soler (2004). Anions are denoted as X in the legend. Diffusion coefficients perpendicular (a) and parallel (b) to bedding. On the right side, average ratios are indicated.

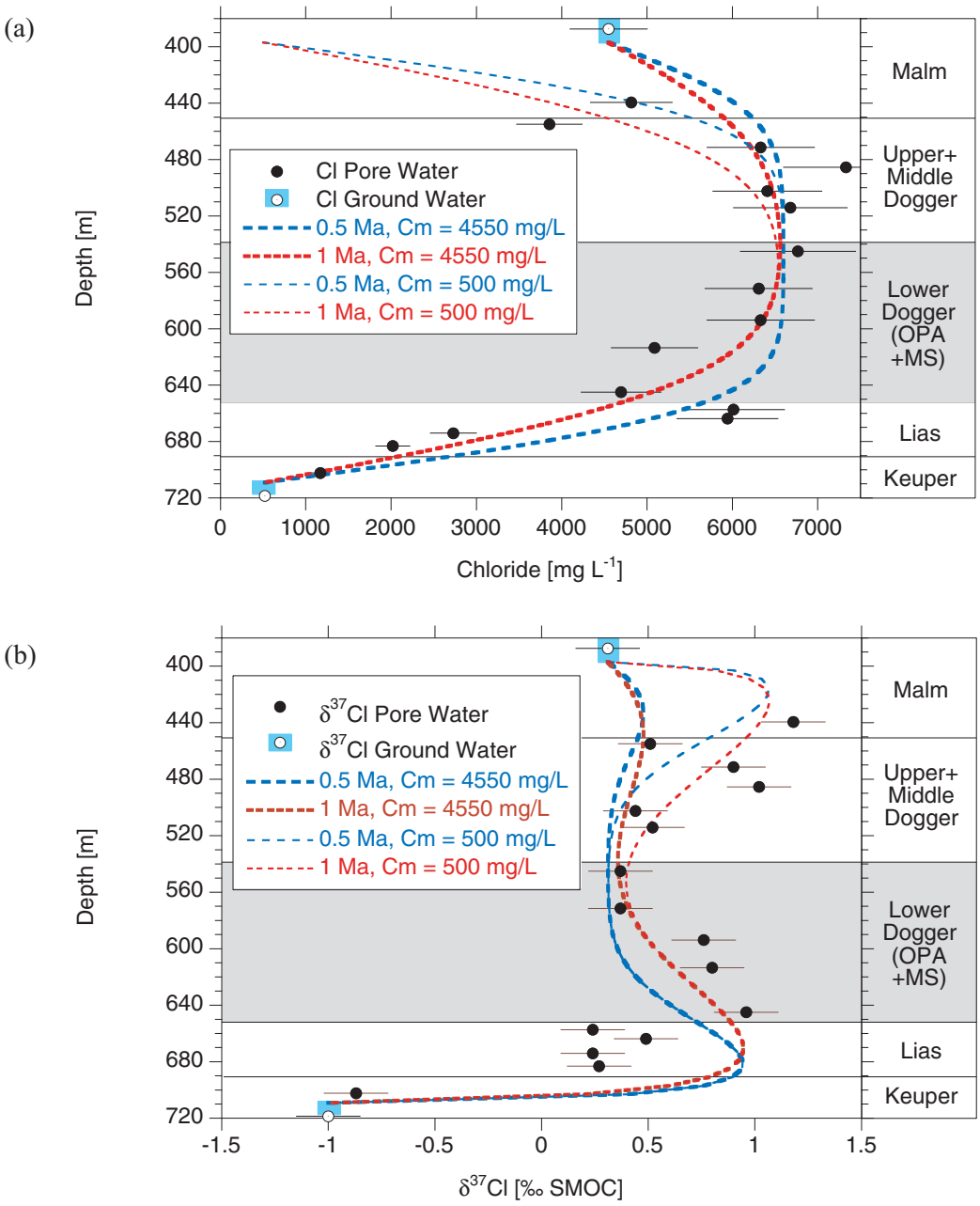

Figure 34: Calculated profiles of chloride (a) and $\delta^{37}Cl$ (b) for the base case and for a constant, lower Cl concentration at the Malm boundary.

Thick lines are for the base case with constant Cl and $\delta^{37}Cl$ concentrations at top and bottom equivalent to values measured in the ground water (cf. Table 9), purely diffusive transport, and a ratio of diffusion coefficients of ^{35}Cl to ^{37}Cl of 1.002. Thin lines are for identical conditions, except a constant, lower Malm boundary concentration of 500 mg L^{-1}. The evolution times are estimated for a Cl pore diffusion coefficient at 40 °C of 5×10^{-11} m^2 s^{-1}, which is half the value used for stable water isotopes. The curves labelled with 1 Ma are the same as would be calculated using an evolution time of 0.5 Ma, and a Cl pore diffusion coefficient at 40 °C of 1×10^{-10} m^2 s^{-1}, i.e. identical to that for stable water isotopes.

6.2.3 Variation of ratio of diffusion coefficients of Cl isotopes

The simulations for $\delta^{37}Cl$ depend on the ratio of the diffusion coefficients of ^{35}Cl and ^{37}Cl, which is sometimes also denoted as enrichment or fractionation factor. For the base case, we used a value of 1.002 as recommended by Eggenkamp et al. (1994). Since there is some uncertainty about the relevant ratio (Desaulnier et al. 1986; Eggenkamp et al. 1994; Hendry et al. 2000), we varied this parameter also slightly. Figure 35 shows simulations for a ratio of 1.001, 1.003, and 1.0093 as compared to the base case. The value of 1.0093 was calculated based on the mass differences of ^{35}Cl and ^{37}Cl, each hydrated with four water molecules. Such a high fractionation ratio has never been observed in experiments (Desaulnier et al. 1986; Eggenkamp et al. 1994), so it is considered as unrealistic, and calculations are just shown for comparison purposes. The higher this ratio, the more pronounced are the peaks of the relative ^{37}Cl excess (Figure 35), but even for the ratio of 1.003, which is considered possible in contrast to the value of 1.0093, clear discrepancies between simulations and measurements remain.

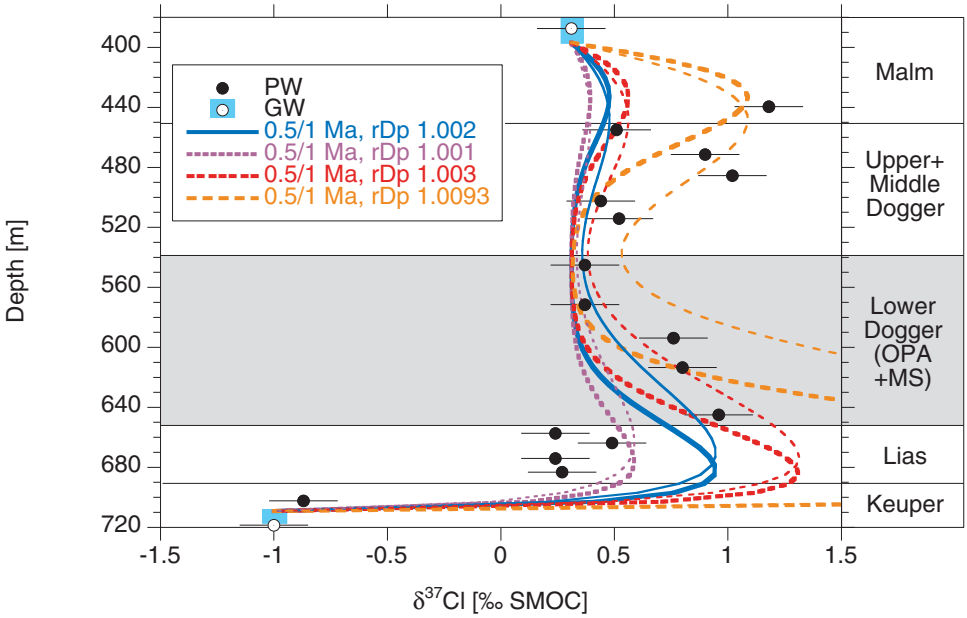

Figure 35: Influence of ratio of diffusion coefficients D_p of ^{35}Cl to ^{37}Cl.

For the base case, a ratio of 1.002 was assumed (solid lines). The ratio calculated based on mass differences, 1.0093, is not considered relevant for real profiles, and is just shown for comparison purposes. Thick lines are for an evolution time of 0.5 Ma based on a D_p of 5×10^{-11} m^2 s^{-1}, thin lines for 1 Ma based on a D_p of 5×10^{-11} m^2 s^{-1}, or for 0.5 Ma based on a D_p of 1×10^{-10} m^2 s^{-1}.

6.2.4 Variation of Cl-accessible porosity

Relevant concentrations of Cl in the pore water have to be calculated based on the fraction of Cl-accessible pore water. As stated, a value of 0.5 was used for this fraction for the whole domain, based on laboratory diffusion measurements with anions, squeezing samples, and comparison with Mont Terri data (cf. 4.2.1). In some diffusion experiments, especially for samples with relatively high clay content, a smaller Cl-accessible fraction was observed (Van Loon & Soler 2004). To test the influence of this fraction on the simulations, we rescaled the Cl data using a Cl-accessible pore fraction of 0.3 instead of 0.5. Maximum Cl concentrations

increase then to about 11 000 mg L^{-1} in the centre of the domain (Figure 36). One should note that such high concentrations are not compatible with the squeezing data shown in Figure 11; the simulations are only a sensitivity test and cannot represent reality. For the Cl simulations (Figure 36(a)), the correspondence with the observed data is in general similar to that of the base case, and in the upper part even better. As seen in the generic calculations, larger Cl gradients tend to increase the $\delta^{37}Cl$ peaks. This happens also in this case at the Malm boundary (Figure 36(b)). The effect is, however, not large enough to explain the relatively large $\delta^{37}Cl$ values in the upper part of the profile.

Anion exclusion effects are typically only observed in compacted, clay rich materials, which have small pore sizes. Such effects may well be smaller in regions of the low permeability zone with lower clay contents, or with increased porosities. Thus, assuming a constant anion accessible fraction of 0.5 may locally be inaccurate and be partly responsible for the relatively large scatter of the Cl data. For instance, the data in the Lias at depths around 660 m are in a zone, where the geophysical logs indicate a higher porosity (see Figure 14). If the anion accessible fraction in this region were 0.75 instead of 0.5, the two Cl data points would fit much more smoothly into the other data, with values around 4 000 mg L^{-1}. Interestingly, the profiles of $\delta^{18}O$ and $\delta^{2}H$ are at the same time somewhat flatter in this region, which could be explained also by a larger porosity (see Section 6.1.1). As mentioned in Section 6.1.1, spatially variable porosities or diffusion coefficients will of course also influence the simulations, but for the expected variability this influence is relatively small and very likely less important than the above mentioned scaling of the Cl data by the anion-accessible pore fraction.

6.2.5 Variation of Malm boundary conditions

Smaller Cl concentrations than measured today in the Malm aquifer will also lead to larger Cl gradients, and thus larger $\delta^{37}Cl$ peaks. Simulations for a concentration of 500 mg L^{-1} at the Malm interface are shown in Figure 34 (thin lines) together with the base case (thick lines). Such relatively low concentrations at the interface lead to a better description of the Cl data in the lower Malm and upper Dogger, but of course to a discrepancy with the measured Cl value in the Malm aquifer. At the same time, a distinct $\delta^{37}Cl$ peak evolves within the Malm and upper Dogger, which fits better (but not perfectly) to the observed data.

Figure 37 displays calculations for various time-dependent boundary conditions at the Malm interface. For the mixing cell ′MC a′, Cl concentrations in the Malm aquifer start at low values and increase towards those measured today, whereas for the case ′MC b′ they start at higher Cl concentrations and higher $\delta^{37}Cl$ values. The simulations for Cl were in both cases affected only in the upper part, where the data show a relatively large variability anyway. The $\delta^{37}Cl$ values were also affected in the upper part only. There, more pronounced $\delta^{37}Cl$ peaks were calculated, especially if initially larger $\delta^{37}Cl$ values in the Malm aquifer were used.

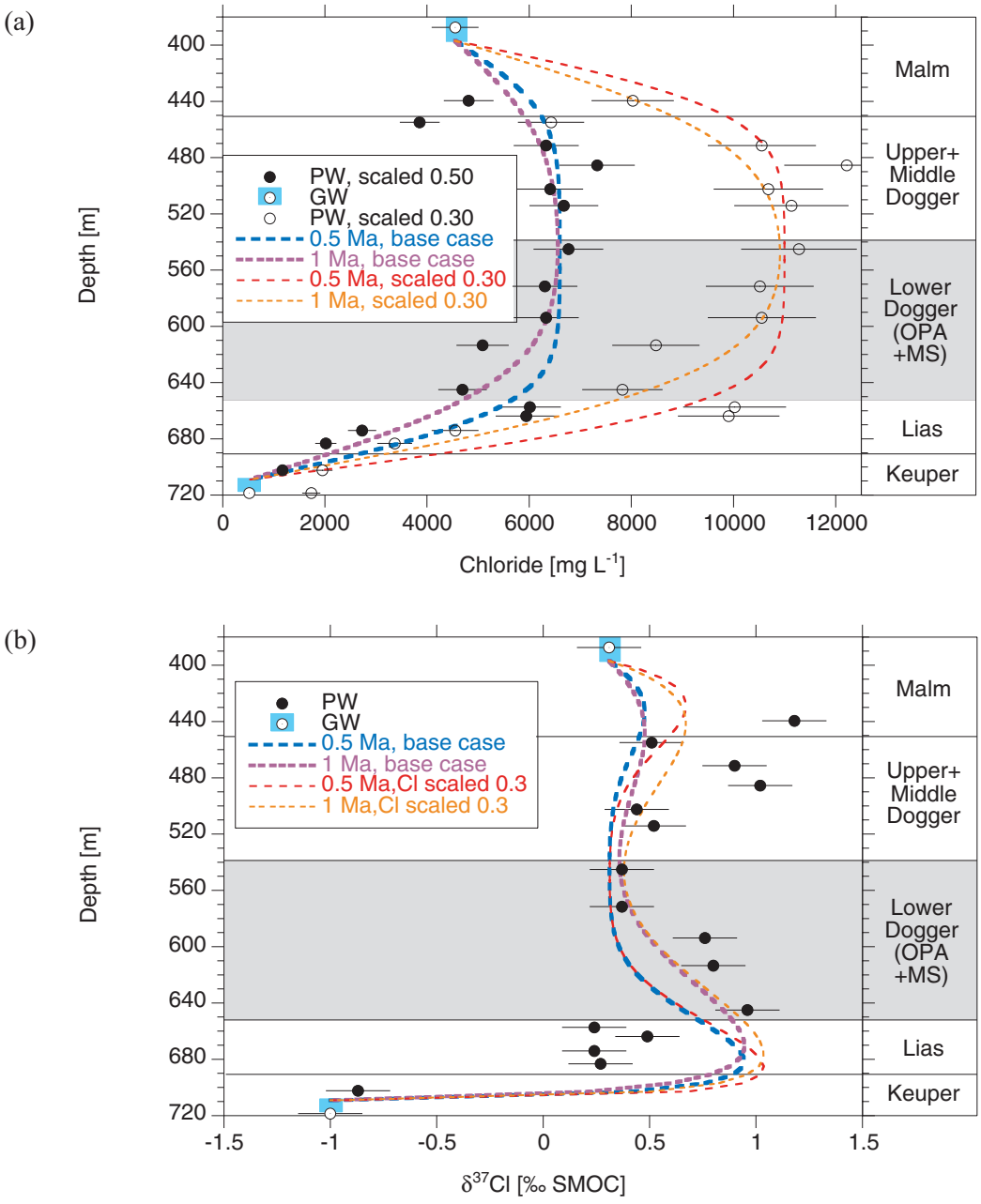

Figure 36: Influence of Cl-accessible porosity on profiles of chloride (a) and $\delta^{37}Cl$ (b).

The thick lines and the solid symbols represent the base case, which relies on a Cl-accessible pore fraction of 0.5. The thin lines and open symbols in (a) are for identical conditions, except that the Cl concentrations were rescaled with a value for Cl-accessible pore fraction of 0.3 instead of 0.5. The evolution times were estimated based on a D_p of 5×10^{-11} m^2 s^{-1}.

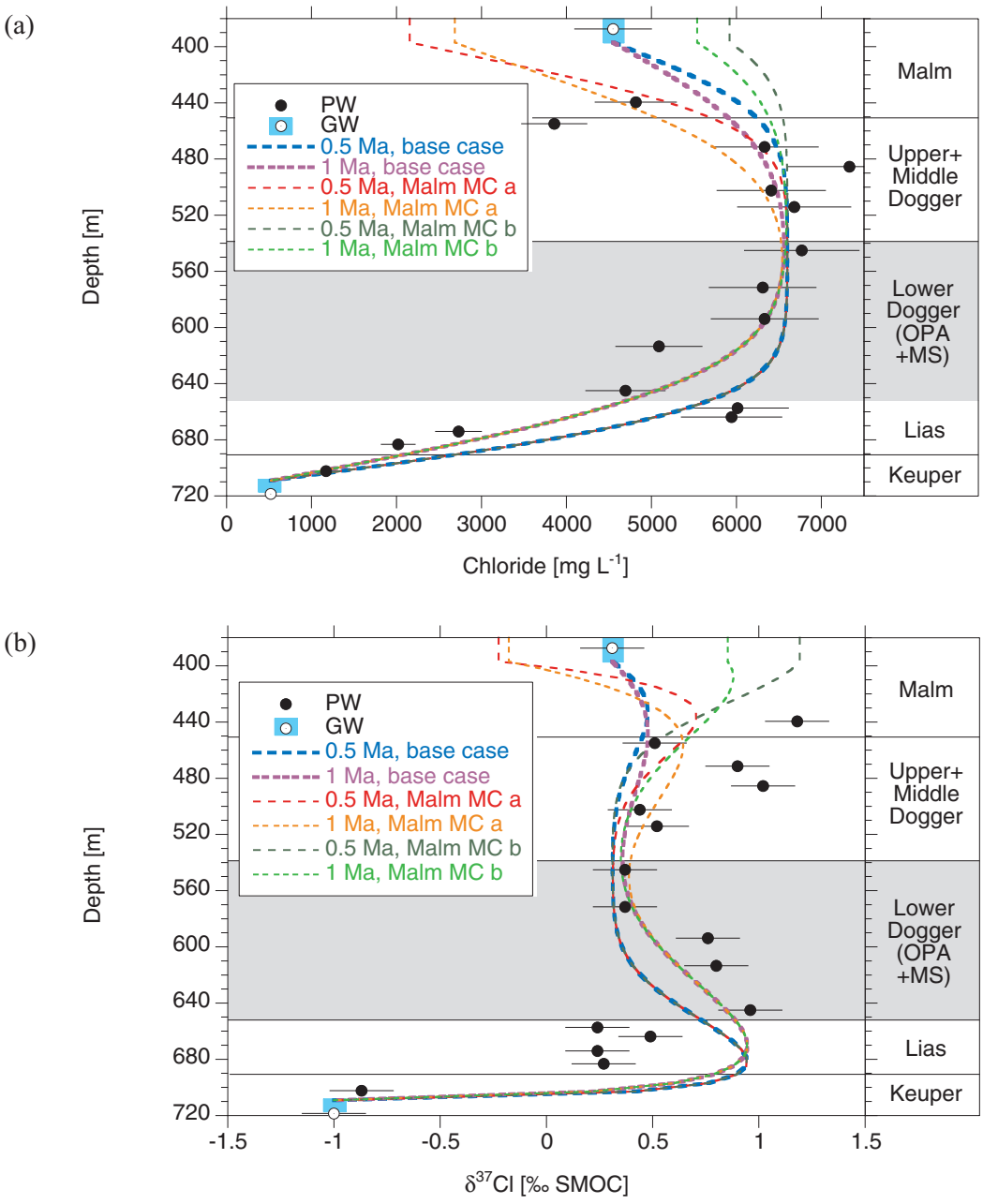

Figure 37: Influence of Malm boundary condition on profiles of chloride (a) and δ^{37}Cl (b).

Thick lines show the base case as in Figure 34; thin lines are for identical conditions, except a mixing cell boundary at the Malm interface. For 'MC a', Cl concentration increases from 500 mg L^{-1} to 4 550 mg L^{-1} ($\rho = 2 \times 10^{-7}$ a^{-1}, $\zeta = 100$ m, δ^{37}Cl at Malm = 0.31). For 'MC b', Cl and δ^{37}Cl concentrations decrease (from 6 600 mg L^{-1} to 4 550 mg L^{-1}, and from 2.0 ‰ to 0.31 ‰, respectively; $\rho = 2 \times 10^{-6}$ a^{-1}; $\zeta = 100$ m).

6.2.6 Variation of Cl initial condition

Effects of larger initial concentrations of Cl are shown in Figure 38. Starting from Cl concentrations of 9 000 mg L^{-1}, an approximate fit of a part of the Cl data – with the exception of the data in the upper Lias – was obtained for a relatively large time of 4 Ma. But for such long diffusion

times, the simulated $\delta^{37}Cl$ profiles look rather different than the observed ones: the two peaks present near the boundaries at smaller times have merged to a single peak, with a maximum value near the interface between the Dogger and Lias. Thus, with the help of the $\delta^{37}Cl$ data it is possible to rule out the hypothesis of significantly larger initial Cl concentrations than observed today, and correspondingly larger diffusion times.

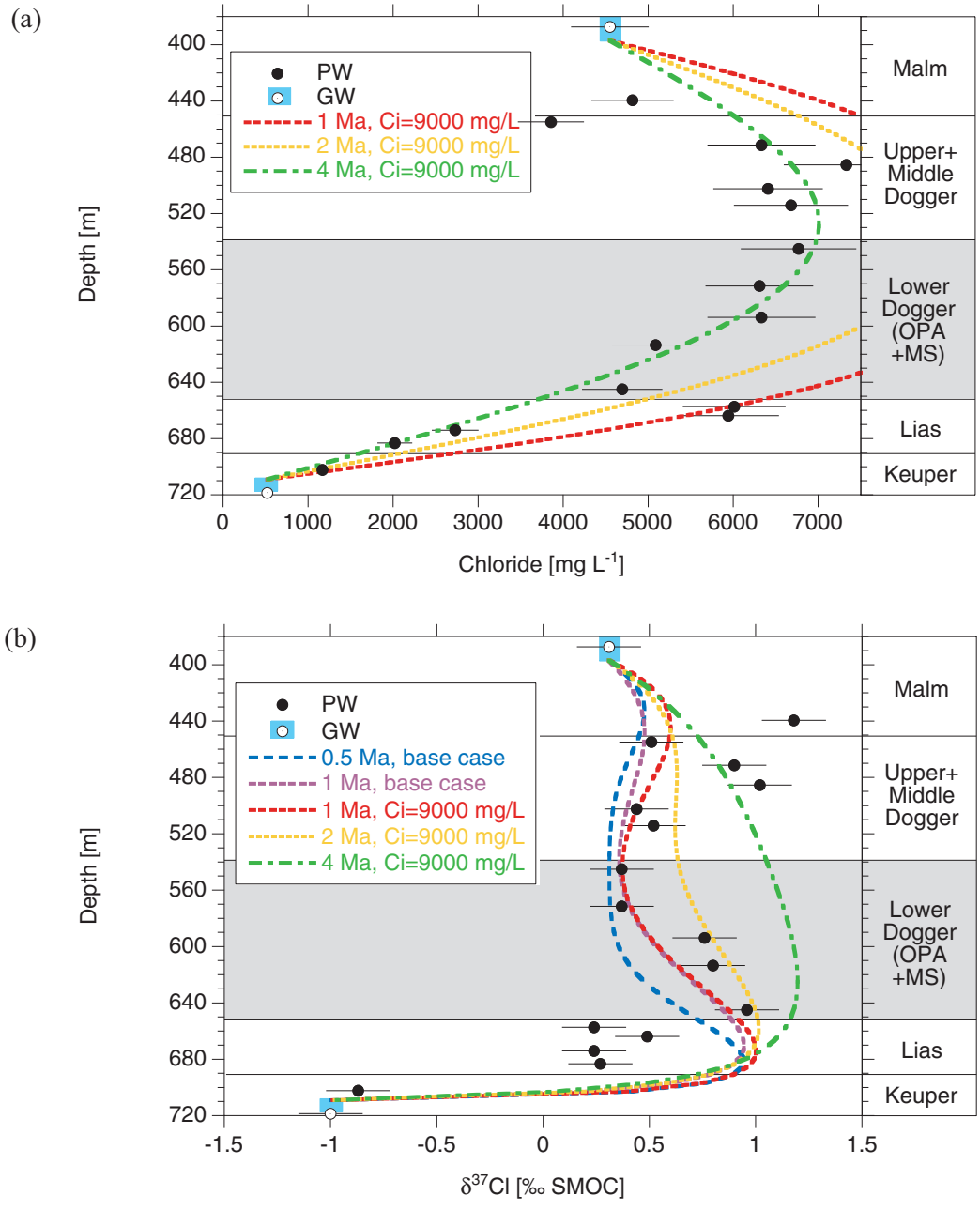

Figure 38: Influence of an increased initial Cl concentration of 9 000 mg L^{-1} on simulated profiles of chloride (a) and $\delta^{37}Cl$ (b).

In (b), the simulations for the base case are also shown as reference.

6.2.7 Variation of Keuper boundary condition

For the stable water isotopes, a gradual decrease of the concentrations at the Keuper aquifer (mixing cell with flushing rate of 2×10^{-5} a^{-1}) rather than the instantaneous drop of the base case also led to acceptable fits, with slightly increased evolution times (cf. Figure 21). Therefore, we present in Figure 39 simulations for Cl and $\delta^{37}Cl$ for the same mixing cell parameters. For Cl, the correspondence to the data at somewhat larger times (1 - 2 Ma) is similar or slightly worse than for the base case, whereas for $\delta^{37}Cl$ the shape of the peak in the lower part more closely resembles the data, even if the maximum values are underestimated. The conclusions that can be drawn based on Figure 39 are the same as those for the stable water isotopes: a slightly more gradual decrease of the Cl concentration in the Keuper aquifer instead of an instantaneous one may be considered, but the correspondence with the data is not or only slightly improved.

6.2.8 Influence of advection

The Cl-accessible pore fraction of Opalinus Clay is only about 0.5 of the porosity that is accessible for water tracers (Nagra 2002, Chapters 5.4.5 and 5.4.6). At the same time, only about half of the pore water in Opalinus Clay is considered as mobile under normal gradients (Nagra 2002, Chapter 5.4.6). Because both the Cl-accessible fraction and the mobile pore water are most likely located in the centre of the larger pores, this means that Cl can access just the mobile pore water. Water tracers, in contrast, access also the immobile pore water, which means that they are in fact retarded as compared to Cl. This retardation, which is probably at equilibrium for the small distances involved, is responsible for the slower breakthrough of water tracers as compared to anions. For Opalinus Clay, it can thus be estimated that Cl moves about two times as fast as a water tracer under the identical hydraulic gradient. Consequently, one can expect that Cl is more sensitive to advective flow (larger Peclet numbers) than the stable water isotopes, especially for the lower D_p value. Also, for direct comparisons of a given scenario, the advective velocity for Cl has to be doubled as compared to stable water isotopes.

In Figure 40, we show some generic calculations for small upward or downward, constant advective velocities ($|v| = 1 \times 10^{-12}$ m s^{-1}). As for the stable water isotopes, such small velocities have only a small effect on Cl concentrations. For $\delta^{37}Cl$, the effects are more pronounced. An upward advective velocity pushes the calculated lower peak upward, and thus improves the correspondence with the measurements somewhat, especially in case of an evolution time of 1 Ma. A downward velocity has the opposite effect.

Figure 41 compares simulations equivalent to the approximate fit obtained for the stable water isotopes at an upward velocity of $v = 2 \times 10^{-12}$ m s^{-1} (cf. Figure 26). For Cl, the velocity is doubled to $v = 4 \times 10^{-12}$ m s^{-1} according to the lower Cl-accessible porosity. Even though it seems that a slight upward velocity leads to a slightly better description of the $\delta^{37}Cl$ data, the rather large scatter of the data and the still rather large discrepancies between measurements and simulations do not allow any definite conclusion. As was shown in the preceding paragraphs, many other processes or parameters may also lead to some improvements of the simulations, and it is not possible to uniquely link the observed differences between data and base case simulations to one process or parameter value.

One has to keep in mind also that we included only diffusive fractionation processes in our model. During advective flow through clay membranes, other fractionation processes may also occur (Phillips & Bentley 1987). The corresponding processes are not yet well understood, and the question remains open, whether those other fractionation processes are observed also under field conditions. In any case, one should be careful when interpreting the simulations presented in Figures 40 and 41.

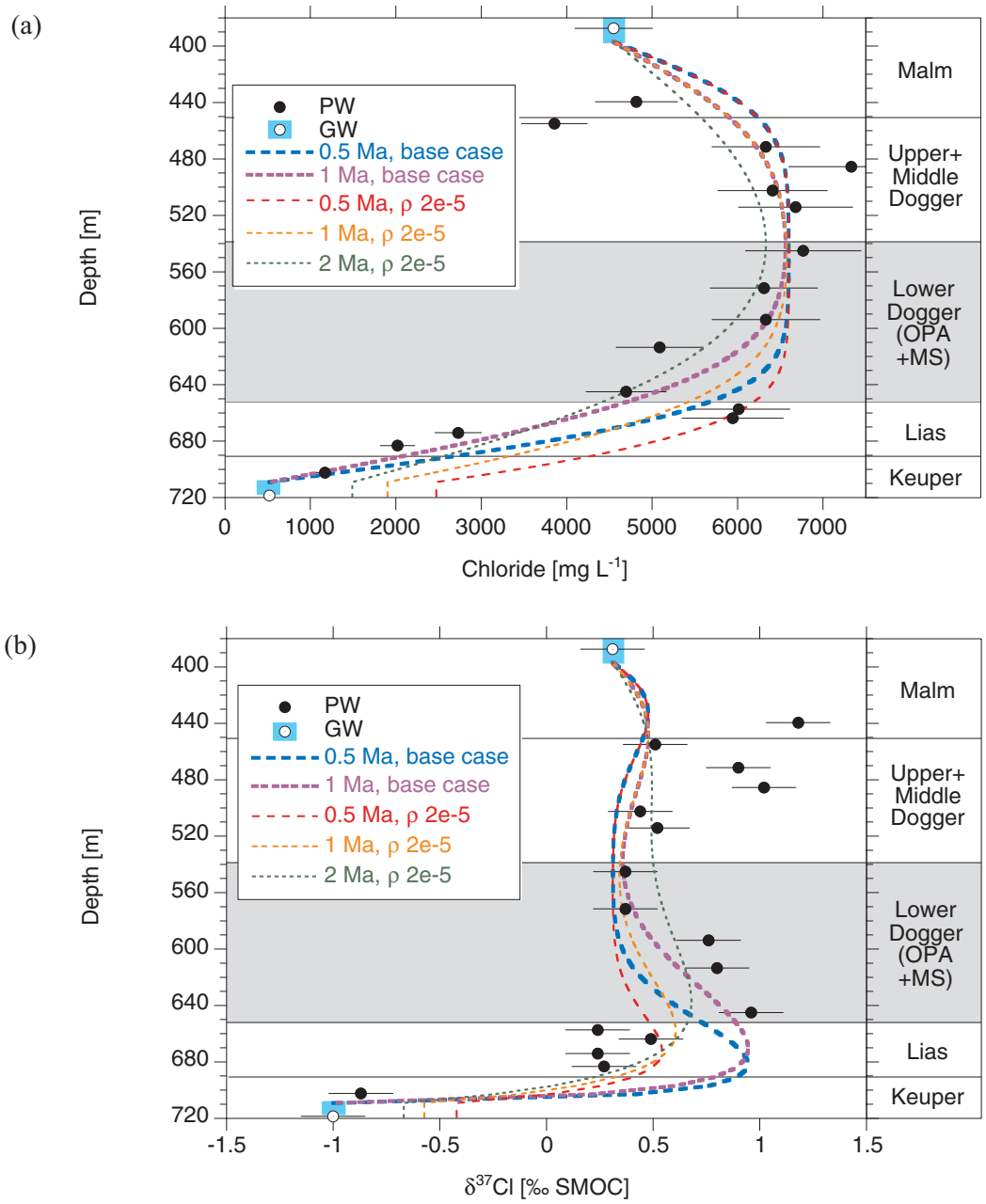

Figure 39: Influence of a gradual decrease of the Cl concentration in the Keuper aquifer.

Thin lines: mixing cell with $\rho = 2 \times 10^{-5}$ a^{-1}, $\zeta = 10$ m, initial concentrations 6 600 mg L^{-1} and –1 ‰, inflow concentrations 4 550 mg L^{-1} and –1 ‰. The thick lines represent the base case.

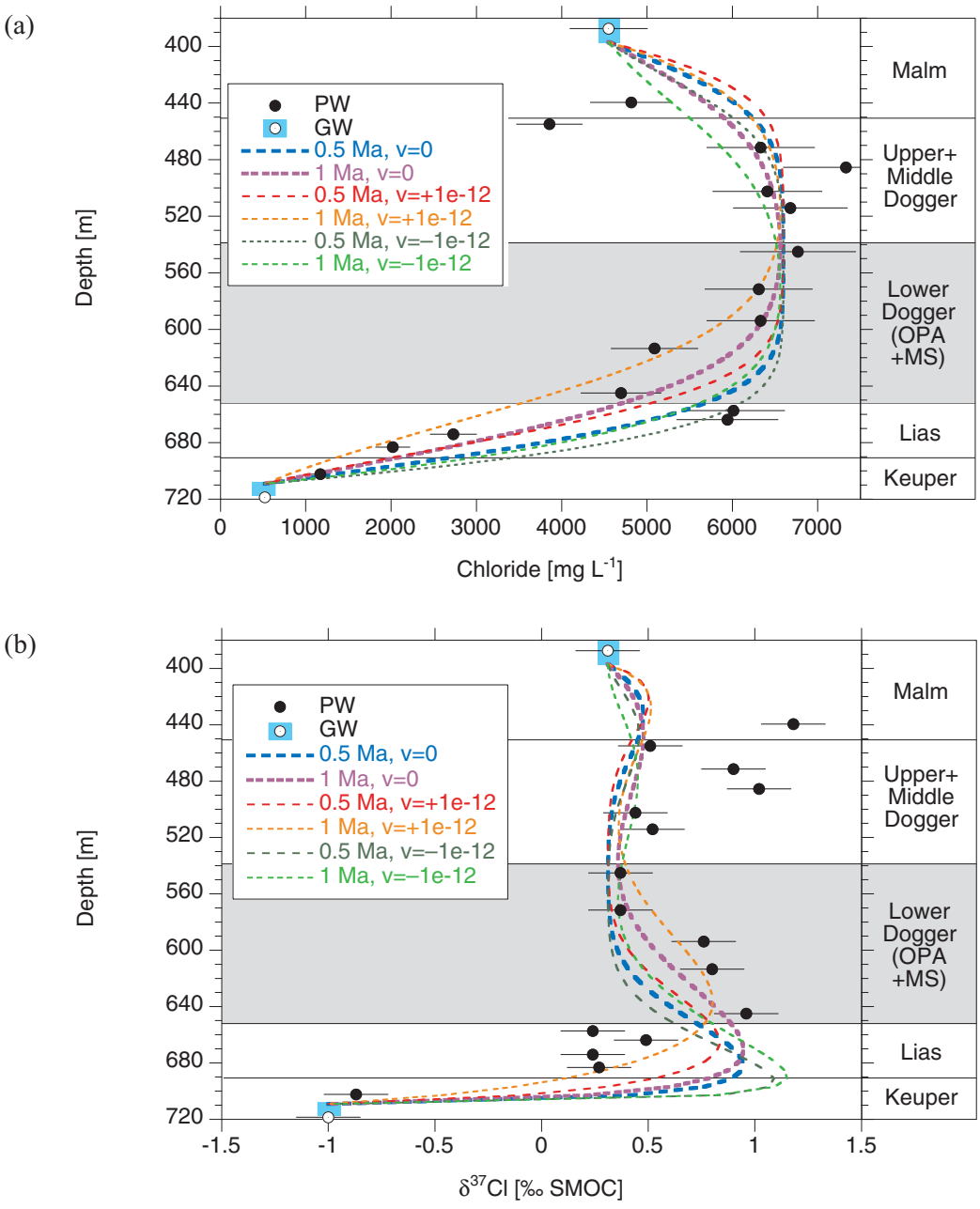

Figure 40: Influence of a small upward or downward advective velocity on calculated profiles of chloride (a) and $\delta^{37}Cl$ (b).

Thin lines: upward ($v > 0$) or downward ($v < 0$) velocity; thick lines: base case for pure diffusion. Note that the evolution times were evaluated for a D_p of 5×10^{-11} m^2 s^{-1}. For $v \neq 0$, the curves labelled with 1 Ma correspond also to simulations for an evolution time of 0.5 Ma and $|v| = 2 \times 10^{-12}$ m^2 s^{-1}, if $D_p = 1 \times 10^{-10}$ m^2 s^{-1} is assumed (because then $\xi = (D_p\, t)^{0.5}$ and D_p/v are identical for the two cases).

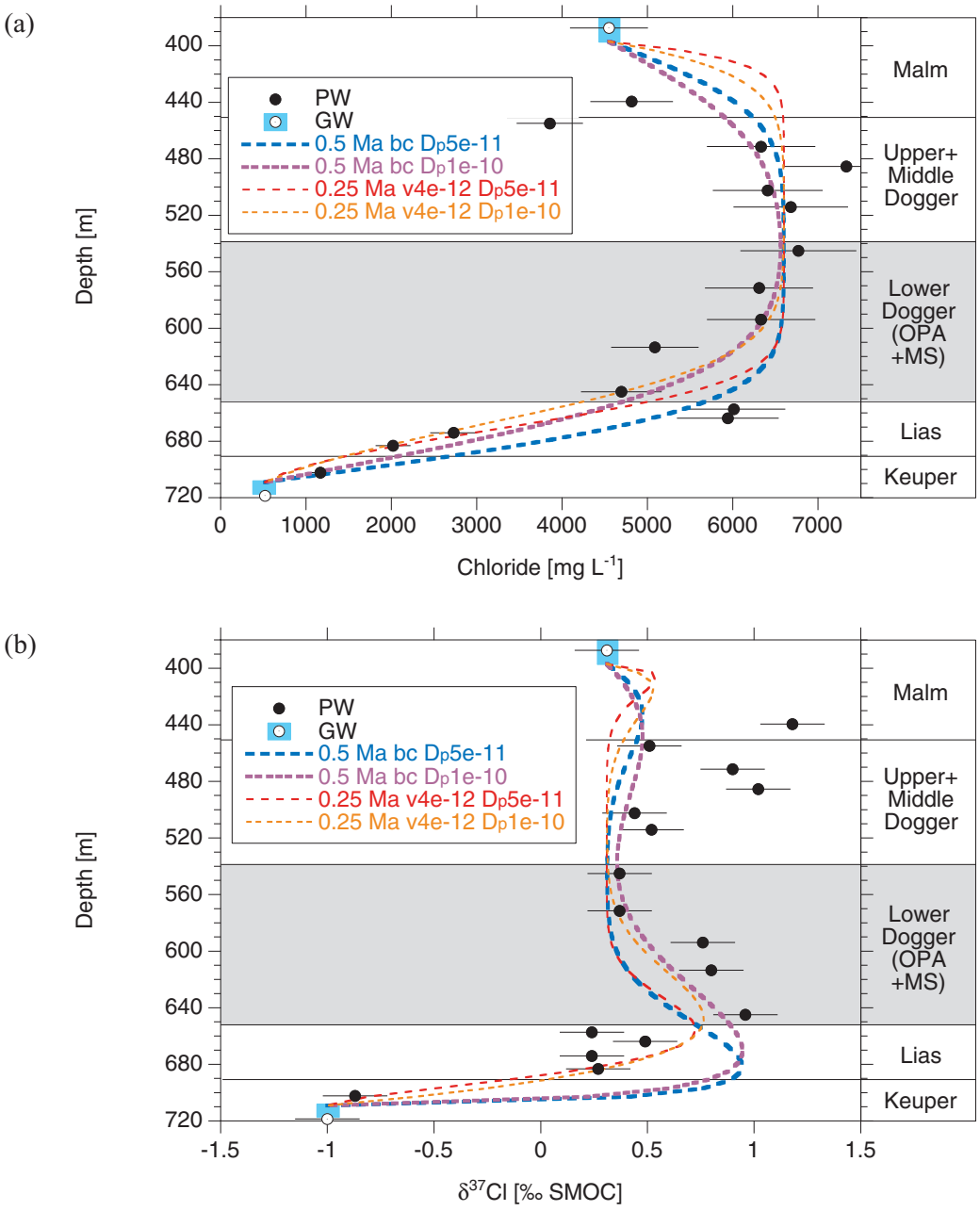

Figure 41: Influence of a slightly increased upward advective velocity, and shorter evolution time, on calculated profiles of chloride (a) and $\delta^{37}Cl$ (b).

Thin lines: advective velocity v>0; thick lines: base case for pure diffusion. For both cases, simulations for $D_p = 5 \times 10^{-11}$ m^2 s^{-1} and $D_p = 1 \times 10^{-10}$ m^2 s^{-1} are shown.

6.2.9 Future evolution of Cl profiles

The geochemical composition of the pore water in the potential host rock is largely determined by equilibrium reactions with the rock minerals (clay minerals, carbonates), which have a large buffering capacity. Thus, concentrations of cations or neutral species controlled by water-rock reactions will remain fairly constant over the next 1 Ma. In contrast, salinity, which is largely determined by Cl and the dominant charge-balancing cation (in this case Na), will continue to change according to the concentrations in the surrounding aquifers. Figure 42 presents the expected changes of Cl concentrations over the next 1 Ma, if diffusion dominates the transport and aquifer concentrations remain similar as today. The assumptions are reasonable based on geologic observations, even though future glaciations might increase the influence of advection slightly during relatively short time periods. An approximate fit of the measured data is labelled as today. Calculations for 0.5 or 1 Ma from today (based on a diffusion coefficient at 40 °C of $D_p = 5 \times 10^{-11}$ m^2 s^{-1}) show that the expected changes are relatively small. For the next 1 Ma, calculated changes within the potential host rock are between about 5 % (top of Opalinus Clay) and 20 % (bottom of Opalinus Clay).

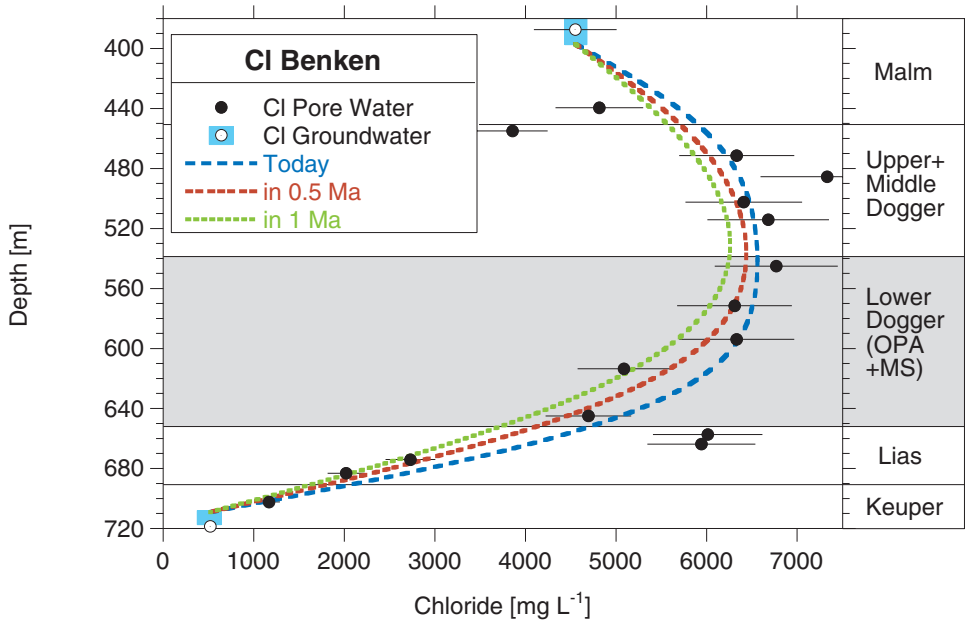

Figure 42: Evolution of the Cl profiles at Benken under the assumptions of diffusive transport and constant boundary conditions at the aquifers with values as today.

The indicated times are based on a diffusion coefficient $D_p = 5 \times 10^{-11}$ m^2 s^{-1}. Changes within the potential host rock remain relatively small (≤ about 20%) within this time span.

6.2.10 Summary of results for Chloride and ^{37}Cl

From the simulations of the observed Cl and $\delta^{37}Cl$ profiles presented above, the following conclusions can be drawn:

- Both Cl and $\delta^{37}Cl$ data show several features that cannot be explained by simple two-sided diffusion processes within the given errors.
- The processes that led to these more complicated shapes are not known. It cannot be ruled out, however, that a part of the variability of the data should just be regarded as scatter, originating from (unknown) local values of Cl-accessible pore fraction, for instance. Thus, the field data might be smoother, or the errors larger than indicated.
- For $\delta^{37}Cl$ especially, the initial profiles may have been non-uniform, because signatures of older processes, e.g. those occurring during burial, might have persisted. Such signatures may last for long times, as was demonstrated in the generic calculations.
- The observed peaks of $\delta^{37}Cl$ close to the upper and lower boundaries could indicate ongoing diffusive processes, but could partly also be inherited from older processes.
- Simulations that approximately describe the overall features of the Cl and the $\delta^{37}Cl$ data could be obtained for identical or – depending on the assumed value of D_p for Cl – slightly longer times than for stable water isotopes (range of about 0.5 - 2 Ma). The agreement is, however, not completely satisfying, and, especially for $\delta^{37}Cl$, of a more qualitative nature.
- The observed Cl and $\delta^{37}Cl$ data do not contradict the interpretations made in the analysis of the profiles of stable water isotopes. But, they also cannot be used to clearly corroborate those findings. The simulation of the Cl and $\delta^{37}Cl$ data requires additional parameters and boundary and initial conditions, which are unknown and – especially for $\delta^{37}Cl$ – not easily inferred from geologic history or from process understanding.

7 Summary and Conclusions

Values of $\delta^{18}O$ and $\delta^{2}H$ as well as chloride concentrations and values of $\delta^{37}Cl$ were determined in the pore fluid of low-permeability formations at Benken in north-eastern Switzerland. The formations are of Jurassic and uppermost Triassic age, and they were sampled at depths between about 400 and 700 m. A new technique based on diffusive exchange of stable water isotopes (Rübel & Sonntag, 2000; Nagra, 2001) had to be used to obtain the pore-water isotopic composition from the rock samples, because the conventional vacuum-distillation method was proven to be inaccurate for argillaceous rocks. The data obtained with this new technique describe depth profiles that provide a unique opportunity to evaluate the transport behaviour of the Jurassic sedimentary rocks on large spatial and temporal scales.

The observed profiles seem to be influenced mainly by mass exchange with the underlying Keuper aquifer. To quantify the mass transfer processes, we performed a series of advective-diffusive transport simulations. In accordance with the hydrogeological history, we varied the initial and boundary conditions, as well as model parameters. The most important conclusions from the simulations of the *stable water isotopes* in the pore water are the following:

- The profiles evolved mainly via molecular diffusion. No signature of advective flow could be detected.
- Depending on boundary conditions, a diffusion distance $\xi = (t\ D_p)^{0.5}$ of about 40 to 56 m was estimated. This corresponds to evolution times of 0.5 to 1 Ma (1 Ma = 10^6 years) based on a laboratory diffusion coefficient D_p at 40°C (Van Loon & Soler, 2004) of $1 \cdot 10^{-10}$ $m^2\ s^{-1}$.
- Additional uncertainty about relevant temperatures and processes (e.g. slight variability of porosities and diffusion coefficients) increases the estimated span of evolution to about 0.2 – 1.5 Ma.

The simulations also revealed that, prior to the onset of flow in the local Keuper aquifer, the isotope ratios in the low-permeability zones were shifted to lower values with respect to the initial marine pore water. Furthermore, some time after activation of flow, values of stable water isotopes in the Keuper aquifer decreased rapidly to meteoric values typical for the recharge area for the time considered.

The interpretation of the *chloride and $\delta^{37}Cl$* data proved to be more difficult, with the measured concentrations displaying a larger scatter in the vertical direction. Part of the vertical variability in the Cl data may originate from the unknown scaling factor for the Cl-accessible fraction of the rock pores. This factor is required to estimate relevant pore-water concentrations. The explanation applies particularly to the lithologies above and below the Opalinus Clay, which have a lower total content of clay. Comparing the interpretation of the Cl and $\delta^{37}Cl$ data with that of the $\delta^{18}O$ and $\delta^{2}H$ data, the following statements can be made:

- The observed Cl and $\delta^{37}Cl$ data do not contradict the interpretations of the stable water isotope data.
- Molecular diffusion seems to be the most important transport mechanism for Cl as well, but some features above and below the Opalinus Clay cannot be explained fully by a simple two-sided diffusion over the time span considered. In particular, some features of the $\delta^{37}Cl$ data may be due to older processes.
- The derivation of the Cl and $\delta^{37}Cl$ pore-water data and their simulation requires additional parameters, such as the solute-specific accessible porosity. These are not precisely known and therefore the uncertainty of the reconstructed pore-water composition is increased.

Also, the boundary- and initial conditions for Cl and $\delta^{37}Cl$ are less easily inferred from the geologic history and the present understanding of major processes. Consequently, the results are subject to larger uncertainties or discrepancies.

The evolution times of about 0.5 to 1 Ma for the observed profiles, which were estimated using laboratory diffusion coefficients, are plausible when compared to geological and geochemical evidence (activation of Keuper flow systems in this area at about 2 Ma b.p., residence times of Keuper water much longer than 25 ka, but less than 2.6 Ma). At the same time, no advective signatures could be detected in the isotope and Cl profiles, in accord with the low hydraulic conductivities determined in the laboratory and via borehole tests, and with the present-day hydraulic gradients.

The combination of the findings for the stable water isotopes, chloride and chloride isotopes in the pore water of the low-permeability zones allows an additional, more general conclusion to be drawn:

- Several parameters of the investigated Jurassic sedimentary rocks, such as diffusion coefficients and hydraulic conductivities, which were measured on small spatial and temporal scales (centimeters or meters, months), seem to be applicable at larger scales (tens of meters, millions of years), at least to within an order of magnitude.

Acknowledgements

The authors would like to thank Andreas Gautschi (Nagra) for the very encouraging and professional support during this project. We have greatly benefited from intensive scientific discussions with him as well as with Martin Mazurek (University of Bern) and other colleagues from Bern and from the Paul Scherrer Institut. We also wish to thank Ghislain de Marsily (University Paris VI) for his very constructive and valuable review of the first draft of this report, and Joe Pearson (Ground-Water Geochemistry) for his equally thoughtful scientific and editorial comments on the final draft version of the report.

References

Aeschbach-Hertig, W., Peeters, F., Beyerle, U., & Kipfer, R. (2000): Paleotemperature reconstruction from noble gases in ground water taking into account equilibration with entrapped air, Nature 405, 1040-1044.

Balderer, W. (1990): Hydrogeologische Charakterisierung der Grundwasservorkommen innerhalb der Molasse in der Nordostschweiz aufgrund von hydrochemischen und Isotopenuntersuchungen. Steir. Beitr. Z. Hydrogeologie, 41, 35-104.

Balderer, W., Pearson, F.J., & Soreau, S. (1991): Sulphur and Oxygen Isotopes in Sulphate and Sulphide. In: Pearson, F.J., Balderer, W., Loosli, H.H., Lehmann, B.E, Matter, A., Peters, Tj., Schmassmann, H. & Gautschi, A. (eds.), Applied Isotope Hydrogeology - A Case Study in Northern Switzerland. Studies in Environmental Science 43, Elsevier Amsterdam, 297-322.

Birkhäuser, Ph., Roth, Ph., Meier B., & Naef H. (2001): 3D-Seismik: Räumliche Erkundung der mesozoischen Sedimentschichten im Zürcher Weinland, Nagra Technical Report NTB 00-03, Nagra, Wettingen, Switzerland.

Bertleff, B. (1986): Das Strömungssystem der Grundwässer im Malm-Karst des West-Teils des süddeutschen Molassebeckens. Abh. des Geol. Landesamtes Baden-Württenberg, 12.

Bertleff, B., & Watzel, R. (2002): Tiefe Aquifersysteme im südwestdeutschen Molassebecken. Eine umfassende hydrogeologische Analyse als Grundlage eines zukünftigen Qunatitäts- und Qualitätsmanagements. Abh. Landesamt f. Geologie, Rohstoffe und Bergbau Baden-Württemberg, 15, 75-90.

Biehler, D., Schmassmann, H., Schneemann, K., & Sillanpää, J. (1993): Hydrochemische Synthese Nordschweiz: Dogger-, Lias-, Keuper- und Muschelkalk-Aquifere, Nagra Technical Report NTB 92-87, Nagra, Wettingen, Switzerland.

Carslaw, H.S., & Jaeger, J.C. (1959): Conduction of heat in solids, 2nd ed. Oxford University Press, Oxford, Great Britain.

Clark, I.D., & Fritz, P. (1997): Environmental Isotopes in Hydrogeology, Lewis Publishers, Boca Raton, USA.

Coudrain-Ribstein, A., Gouze, Ph., & de Marsily, Gh. (1988): Temperature-carbon dioxide partial pressure trends in confined aquifers. Chem. Geol. 145, 73-89.

Cussler, E.L. (1984): Diffusion–Mass Transfer in Fluid Systems. Cambridge University Press, Cambridge.

Desaulniers, D.E., Kaufmann, R.S., Cherry, J.A., & Bentley, H.W. (1986): ^{37}Cl-^{35}Cl variations in a diffusion-controlled groundwater system. Geochim. Cosmochim. Acta 50, 1757-1764.

de Marsily, G., Gonçalves, J., Violette, S., & Castro, M.C. (2002): Migration mechanisms of radionuclides from a clay repository toward adjacent aquifers and the surface. Comptes Rendus Physique 3, 945-959.

Eastoe, C.J., Long, A., Land, L.S., & Kyle. J.R. (2001): Stable chlorine isotopes in halite and brine from the Gulf Coast Basin: brine genesis and evolution. Chem. Geol., 176, 343-360.

Eggenkamp, H.G.M., Middelbourg, J.J., & Kreulen, R. (1994): Preferential diffusion of ^{35}Cl relative to ^{37}Cl in sediments of Kau Bay, Halmahera, Indonesia. Chem. Geol. 116, 317-325.

Eggenkamp, H.G.M., Kreulen, R., & Koster van Groos, A.F. (1995): Chlorine stable isotope fractionation in evaporites. Geochim. Cosmochim. Acta, 24, 5169-5175.

Flury, M., & Gimmi, Th (2002): Solute diffusion. In: Methods of Soil Analysis, Part 4 – Physical Methods. In: Dane, J.H. & Topp, G.C. (eds.), Soil Science Society of America Inc., Madison, Wisconsin, USA, p. 1323-1351,.

Gimmi, Th. (2003): Porosity, pore structure, and energy state of pore water of Opalinus Clay. Unpubl. Nagra Internal Report, Nagra, Wettingen, Switzerland.

Gimmi, Th., & Flühler, H. (1998): Mixing-cell boundary conditions and apparent mass balance errors for advective-dispersive solute transport. J. Contam.Hydrol. 33, 101-131.

Graf, W., & Trimborn, P. (1997): Isotopengehalte der Niederschläge an Stationen aus dem Süddeutschen Raum. Beiträge zur Hydrogeologie, 48, 7-16.

Gregory, R.T. (1991): Oxygen isotope history of seawater revisited: Timescales for boundary event changes in the oxygen isotope composition of seawater. In: Taylor, H.P., O'Neil, J.R. & Kaplan, I.R. (eds.), Stable Isotope Geochemistry: A Tribute to Samuel Epstein. The Geochemical Society, Special Publ. No. 3, 65-76.

Gonçalves, J., Violette, S., & Wendling, J. (2004): Analytical and numerical solutions for alternative overpressuring processes: Application to the Callovo-Oxfordian sedimentary sequence in the Paris basin, France. J. Geoph. Res.–Solid Earth 109 (B2), art. no. B02110.

Hendry, M.J., Wassenaar, L.I., & Kotzer, T. (2000): Chloride and chlorine isotopes (^{36}Cl and $\delta^{37}Cl$) as tracers of solute migration in a thick, clay-rich aquitard system. Water Resour. Res. 36, 285-296.

Hofmann, F. (1996): Zur plio-pleistozänen Landschaftsgeschichte im Gebiet Hochrhein-Wutach-Randen-Donau: Geomorphologische Überlegungen und sedimentpetrographische Befunde. Eclogae geol. Helv., 89, 1023-1041.

Horseman, S.T., Higgo, J.J.W., Alexander, J., & Harrington, F.J. (1996): Water, gas and solute movement through argillaceous media. OECD Nuclear Energy Agency, Paris.

Hummel, W, Berner, U., Curti, E., Pearson, F.J., & Thoenen, T. (2002): Nagra / PSI Chemical Thermodynamic Data Base 01/01, Universal Publishers/uPublish.com, Parkland, Florida, 565 p.

Jury, W.A., & Roth, K. (1990): Transfer functions and solute movement through soil. Theory and Applications. Birkhäuser, Basel. Switzerland.

Kaufmann, R., Long, A., Bentley, H., & Davis, S. (1984): Natural chlorine isotope variations. Nature, 309, 338-340.

Kipfer, R., Aeschbach-Hertig, W, Peeters, F., & Stute, M. (2002): Noble Gases in Lakes and Ground Waters. In: Porcelli, D., Ballentine, C.J. & Wieler, R., (eds.) Noble Gases in Geochemistry and Cosmochemistry. Am. Min. Soc., Washington DC, Reviews in Mineralogy and Geochemistry, Vol. 47, 615-690.

Kosakowski, G., & Gimmi, Th. (2001): Effects of compaction on fluid velocities in the Opalinus Clay. Unpubl. PSI Int. Rep., Paul Scherrer Institut, Villigen, Switzerland.

Klemenz, W., Blaser, P., & Küpfer, T. (2000): Hydrogeologie des Gebietes Lägern Zürcher Weinland. Unpubl. Nagra Internal Report, Nagra, Wettingen, Switzerland.

Kullin, M., & Schmassmann, H. (1991): Isotopic Composition of Modern Recharge. In: Pearson, F.J., Balderer, W., Loosli, H.H., Lehmann, B.E, Matter, A., Peters, Tj., Schmassmann, H. & Gautschi, A. (eds.), Applied Isotope Hydrogeology - A Case Study in Northern Switzerland. Studies in Environmental Science 43, Elsevier Amsterdam, 65-89.

Lehmann, B.E., Loosli, H.H., & Tolstikhin, I. (2001): Sondierbohrung Benken: Radioelements (U, Th, K) and noble gases (^{4}He, $^{3}He/^{4}He$, ^{40}Ar, $^{40}Ar/^{36}Ar$) in rocks. Unpubl. Nagra Internal Report, Nagra, Wettingen, Switzerland.

Lemcke, K. (1987): Zur Frage der alten Verkarstung des Malms im Untergrund des deutschen Molassebeckens und an dessen Nordwestrand. Bull. Ver. schweiz. Petroleum-Geol. und -Ing., *53*, 33-46.

Lemcke, K. (1976): Übertiefte Grundwässer im südeutschen Alpenvorland. Bull. Ver. schweiz. Petroleum-Geol. u. Ing., 42, 9-18.

Leu, W., Greber, E., & Schegg, R. (2001): Basin modeling NE-Switzerland, burial, erosion and temperature history of wells Benken, Weiach and Herdern-1. Unpubl. Nagra Internal Report, Nagra, Wettingen, Switzerland.

Loosli, H. H., & Lehmann, B.E. (1991): Argon-39 and Argon-37. In: Pearson, F.J., Balderer, W., Loosli, H.H., Lehmann, B.E, Matter, A., Peters, Tj., Schmassmann, H. & Gautschi, A. (eds.), Applied Isotope Hydrogeology - A Case Study in Northern Switzerland. Studies in Environmental Science 43, Elsevier Amsterdam, 266-275.

Matter, A., Peters Tj., & Ramseyer, K. (1991): Strontium Isotopes in Groundwaters and Minerals. In: Pearson, F.J., Balderer, W., Loosli, H.H., Lehmann, B.E, Matter, A., Peters, Tj., Schmassmann, H. & Gautschi, A. (eds.), Applied Isotope Hydrogeology - A Case Study in Northern Switzerland. Studies in Environmental Science 43, Elsevier Amsterdam, 323-335.

Mazurek, M. (2001): Sprödstrukturen und potentielle Migrationspfade im Opalinuston und seinen Rahmengesteinen. Unpubl. Nagra Internal Report, Nagra, Wettingen, Switzerland.

Nagra, (1988): Sedimentstudie - Zwischenbericht 1988. Nagra Technischer Bericht NTB 88-25, Nagra, Wettingen, Switzerland.

Nagra (2001): Sondierbohrung Benken, Untersuchungsbericht. Nagra Technical Report NTB 00-01, Nagra, Wettingen, Switzerland.

Nagra (2002): Projekt Opalinuston: Synthese der geowissenschaftlichen Untersuchungsergebnisse. Nagra Technical Report NTB 02-03, Nagra, Wettingen, Switzerland.

Patriarche, D., Michelot, J.-L., Ledoux, E., & Savoye, S. (2004a): Diffusion as the main process for mass transport in very low water content argillites: 1. Chloride as a natural tracer for mass transport – Diffusion coefficient and concentration measurements in interstitial water. Water Resour. Res. 40, W01516, doi: 10.1029/2003WR 002600.

Patriarche, D., Ledoux, E., Michelot, J.-L., Simon-Coinçon, R., & Savoye, S. (2004b): Diffusion as the main process for mass transport in very low water content argillites: 2. Fluid flow and mass transport modelling. Water Resour. Res. 40, W01517, doi:10.1029/2003WR002700.

Pearson, F.J. (2002): Benken reference water chemistry. Unpubl. Nagra Internal Report, Nagra, Wettingen, Switzerland.

Pearson, F.J., Arcos, D., Bath, A., Boisson, J.-Y., Fernández, A.M., Gaebler, H.E., Gaucher, E., Gautschi, A., Griffault, L., Hernan, P., & Waber, H.N. (2003): Mont Terri Project - Geochemistry of Water in the Opalinus Clay Formation at the Mont Terri Rock Laboratory. Reports of the Federal Office for Water and Geology (FOWG), Geology Series No 5, Bern, Switzerland.

Phillips, F.M., & Bentley, H.W., (1987): Isotopic fractionation during ion filtration: I. Theory. Geochim. Cosmochim. Acta 51: 683-695.

Plummer, L.N., Prestemon, E.C., & Parkhurst, D.L. (1994): An interactive code (NETPATH) for modeling net geochemical reactions along a flow path, version 2.0. U.S. Geological Survey Water Resources Investigations Report 94-4169.

Rübel, A., & Sonntag, Ch. (2000): Sondierbohrung Benken: Profiles of pore water content, stable isotopes and dissolved noble gas content in the pore water of samples of argillaceous rocks. Unpubl. Nagra Internal Report, Nagra, Wettingen, Switzerland.

Rübel, A., Sonntag C., Lippmann J., Gautschi A., & Pearson F.J. (2002): Solute transport in formations of very low permeability: Profiles of stable isotope and dissolved gas contents of the pore water in the Opalinus Clay, Mont Terri, Switzerland. - Geochim. Cosmochim. Acta 66, 1311-1321.

Sacchi, E., & Michelot, J.-L. (2000): Porewater Extraction from Argillaceous Rocks for Geochemical Characterisation, Methods and Interpretation. OECD Nuclear Energy Agency, Paris.

Schmassmann, H. (1990): Hydrochemische Synthese Nordschweiz: Tertiär- und Malm-Aquifere. Nagra Technical Report NTB 88-07, Nagra, Wettingen, Switzerland.

Schmassmann, H., Kullin, M., & Schneemann, K (1992): Hydrochemische Synthese Nordschweiz: Buntsandstein-, Perm- und Kristallin-Aquifere. Nagra Technical Report NTB 91-30, Nagra, Wettingen, Switzerland.

Steffen, P., Waber, H.N., & Frieg, B. (2000): Sondierbohrung Benken: Tracerservice, Hydrochemie, Probenahme, Analysenresultate und Isotopenmessungen. Unpubl. Nagra Internal Report, Wettingen, Switzerland.

Stober, I., & Villinger, E. (1997): Hydraulisches Potential und Durchlässigkeit des höheren Oberjuras und des Oberen Muschelkalks unter dem baden-württembergischen Molassebecken. Jh. geol. Landesamt Baden-Würtemberg 37, 77-96.

Traber, D., Waber, H.N., Eichinger, L., & Heidinger, M. (2002): Hydrochemie und Isotopenhydrologie von Tiefengrundwässern in der Region Lägern - Zürcher Weinland – Hegnau. Unpubl. Nagra Internal Report, Nagra, Wettingen, Switzerland.

Trümpy, R. (1980): Geology of Switzerland. Part A: An Outline of the Geology of Switzerland. Wepf & Co., Basel, 104 p.

Thury, M., Gautschi, A., Mazurek, M., Müller, W.H., Naef, H., Pearson, F.J., Vomvoris, S., & Wilson, W. (1994): Geology and hydrogeology of the crystalline basement of northern Switzerland. Nagra Technical Report NTB 93-01, Nagra, Wettingen, Switzerland.

Udluft, P. (1981): Die Süss-Salzwassergrenze Süddeutschlands als Ausdruck der Grundwasserdynamik.. Z. dt. geol. Ges., 132, 623-636.

Van Genuchten, M. Th., & Alves, W.J. (1982): Analytical Solutions of the One-Dimensional Convective-Dispersive Solute Transport Equation. Technical Bulletin 1661, U.S. Departement of Agriculture.

Van Loon, L.R., & Soler, J.M. (2004): Diffusion of HTO, $^{36}Cl^-$, $^{125}I^-$ and $^{22}Na^+$ in Opalinus Clay: Effect of Confining Pressure, Sample Orientation, Sample Depth and Temperature. PSI Report No. 04-03, Paul Scherrer Insitut, Villigen, Switzerland.

Villinger, E. (1988): Bemerkungen zur Verkarstung des Malms unter dem westlichen süddeutschen Molassebecken. Bull. Ver. schweiz. Petroleum-Geol. und -Ing., 54, 41-59.

Villinger, E. (2003): Zur Paläogeographie von Alpenrhein und oberer Donau. Z. dt. geol. Ges. 154, Stuttgart, Deutschland, 193-253.

Waber, H.N., Frape, S.K., & Gautschi, A. (2001): Cl-Isotopes as Indicator for a Complex Paleohydrogeology in Jurassic Argillaceous Rocks, Switzerland. In: Cidu, R. (ed.) Water-Rock Interaction: Proceedings of the 10th International Symposium on Water-Rock Interaction, A.A. Balkema, Rotterdam, 1403-1406.

Waber, H.N., Pearson, F.J., Aeschbach-Hertig, W., Eichinger, L., Lehmann, B.E., & Loosli, H.H. (2002): Sondierbohrung Benken: Hydrochemical and hydroisotopic characterisation of groundwaters. Unpubl. Nagra Internal Report, Nagra, Wettingen, Switzerland.

Waber, H.N., Pearson, F.J., Hobbs, M.Y., & Oyama, T. (2003): Sondierbohrung Benken: Characterisation of pore water from argillaceous rocks. Unpubl. Nagra Internal Report, Nagra, Wettingen, Switzerland.